M.Sc. Thesis

Load verification of the Arklow Bank Offshore Wind Farm

Marcos Álvarez Gómez

September 2007

Preface

This report is the result of the work carried out by Marcos Álvarez Gómez, in the fulfillment of the requirements for obtaining the degree Master of Science in Sustainable Energy Technology, from Technische Universiteit Eindhoven (The Netherlands). The thesis work has been carried out in cooperation between the Wind Energy department of Technische Universiteit Delft (The Netherlands), the Stiftungslehrstuhl Windenergie from Universität Stuttgart (Germany) and GE Wind Energy at Salzbergen (Germany). The supervision of the thesis has been undertaken by Dr.-Ing. Gerard van Bussel and Dipl.-Ing. Michiel Zaaijer at TU Delft, Dr.-Ing. Po Wen Cheng at GE Wind Energy, and Prof. Dr.-Ing. Martin Kühn and Dipl.-Ing. Patrik Passon at SWE.

This report provides a description of the methodology used for the load verification on turbine 1 of the Arklow Bank Offshore Wind Farm, and a discussion of the obtained results. The report begins with an introductory chapter, in which the objectives of the thesis and the approach followed to achieve them are defined. The next chapter provides an overall description of the wind farm and the turbines, as well as the characterization of the site used during the design phase. Chapter 3 delves into the measurement system, both on the meteorological mast and on turbine 1. Chapter 4 deals with environmental data processing (wind, waves, currents and soil), aiming at the verification of the environmental conditions used in design. Chapter 5 discusses the measured natural frequencies for the support structure and blades, comparing them with the natural frequencies predicted in the design and those obtained from simulations. In chapter 6 the model of the turbine in the simulation package FLEX5 is described, and its tuning process explained. Chapter 7 deals with the short term fatigue analysis of few load cases chosen from measurements. For this purpose both orginal and tuned model are used, and the results in terms of fatigue damage equivalent loads are compared with the values of the equivalent loads obtained from measured time histories. In chapter 8, the response of the turbine to severe sea states found in the measurements is analyzed again in terms of fatigue damage equivalent loads, both with the turbine idling and in operation. Finally, chapter 9 presents the main outcomes and conclusions of the project.

Acknowledgements

I would like to start thanking my parents and brother, for their permanent and inconditional support, always. Special thanks also to my grandfather, for his encouragement and concern.

Thanks to all my five supervisors, for their scientific guidance and support along the whole duration of the project. Thanks to Dr.-Ing. Po Wen Cheng, for making this thesis possible, and for his helping hand since the thesis was conceived. Thanks to Prof. Dr.-Ing. Martin J. Kühn for giving me the chance to come to Stuttgart, and for his interest in this project. Thanks to Patrik Passon, for his patience and his unconditioned dedication. Thanks also to Michiel B. Zaaijer, for following the progress of the project in the distance, and for his wise comments and advices. Finally, thanks to Dr.-Ing. Gerard van Bussel, for his direct influence on my choice of studying Wind Energy.

I would also like to thank Nicolai Cosack, for his valuable assistance with FLEX5. Thanks also to Gunther Auer, Rene Aschermann and Dr.-Ing. Henk-Jan Kooijman for their help at and from GE Wind Energy.

Thanks to Giuseppe Mignoli, Valerio Lorenzoni, Ana Benítez and Faraz Memon, for their accomodation assistance during several stages of the project. Thanks to Björn Schmidt, for all the support in the last stressful days. Thanks to all the friends I found during these three years, and those who I had already before. This project would have been different without you, as the author would have not been the same. In this context, especial thanks to Óscar, Miguel, Elena, Gil, Valerio, Giuseppe and Vanesa.

Lastly, thanks to Fundación Arao and Fundación Pedro Barrié de la Maza, for giving me the opportunity of completing this M.Sc. through financial support.

Contents

List of Figures

List of Tables

List of symbols

a	Amplitude
A	Scale factor of the Weibull distribution
BE	Suscript to indicate the edgewise deflection of the blade
BF	Suscript to indicate the flapwise deflection of the blade
C_T	Thrust coefficient
Ca	Added mass coefficient (FLEX5 model)
Cd	Drag coefficient (FLEX5 model)
Coh	Coherence
$CurDir$	Deviation of the current direction with respect to the fore-aft direction (FLEX5 model)
$Curexp$	Exponent of the *power law* applied to the variation of current speed with water depth (FLEX5 model)
d	Water depth
D	Rotor diameter
Dy	Monopile or tower outer diameter (FLEX5 model)
E'	Energy content of the wind distribution
$Emod$	Young modulus (FLEX5 model)
f	Frequency
f_x	(x+1)-th natural frequency
F	Cumulative probability
F	Force
$Freq$	First natural frequency of the support structure (FLEX5 model)
$Gmod$	Shear modulus (FLEX5 model)
H	Hydrodynamic excitation
H	Section height (FLEX5 model)
H	Wave height
H_s	Significant wave height
H_{s50}	Extreme significant wave height, with a return period of 50 years
I	Turbulence intensity
I_{ref}	Reference turbulence intensity
Iud	Input-output flag (FLEX5 model)
k	Shape factor of the Weibull distribution
k	Stiffness
k	Wavenumber
Kky_t	Nacelle tilt stiffness (FLEX5 model)
Ktx_t	Torsional stiffness of the tower (FLEX5 model)
l_0	Apparent fixity length

L	Wave length
L_c	Coherence scale parameter
m	Inverse slope of the S-N curve
M	Moment
$Mlump$	Lumped mass on either the monopile or the tower section (FLEX5 model)
MS	Suscript to indicate the deflection of the main shaft in both tilt and yaw directions
MST	Suscript to indicate the deflection of the main shaft in tilt direction
MSY	Suscript to indicate the deflection of the main shaft in yaw direction
n	Number of cycles
n_0	Number of zero up-crossings
N	Number of data
$Nsnit$	Number of sections in which either the monopile or the tower are divided (FLEX5 model)
p	Probability
r	Magnitude of the projection of the separation vector between two points on a plane normal to the average wind direction (for the calculation of coherence)
rho	Density of the material of the monopile (FLEX5 model)
Rho_w	Water density (FLEX5 model)
S	Spectral density
SS	Suscript to indicate the deflection of the support structure in both fore-aft and side-to-side directions
SST	Suscript to indicate the deflection of the support structure in fore-aft direction
SSR	Suscript to indicate the deflection of the support structure in side-to-side direction
t	Time
t	Wall thickness (FLEX5 model)
t_{series}	Time series length
T_z	Zero up-crossing period
T_{z50}	Zero up-crossing period associated with H_{s50}
U	Wind speed
$\bar{U}$	10-min mean wind speed
U_{mean}	Mean wind speed
U_{ref}	Extreme 10 min mean wind speed at hub height, with a return period of 50 years
$Ucur$	Current speed at sea surface (FLEX5 model)
W	Wind excitation
$WaveDir$	Deviation of the waves direction with respect to the fore-aft direction (FLEX5 model)
X_{bl}	X blade axis, in the flange plane, according to the right hand rule with reference to Y_{bl} and Z_{bl}
X_{msh}	X main shaft axis, positive in direction of the main shaft axis, positive in direction of the wind

X_n	X nacelle axis, parallel to the main shaft axis, positive in direction of the wind
X_t	X support structure axis, projection of the X_{msh} on the tower bottom flange plane, positive in direction of the wind
Y_{bl}	Y blade axis, in the flange plane, parallel to the rotor plane at a pitch angle of 3^o
Y_{msh}	Y main shaft axis, in the rotor plane according to the right hand rule with reference to X_{msh} and Z_{msh}
Y_n	Y nacelle axis, horizontal and orthogonal to the X_n axis
Y_t	Y support structure axis, according to the right hand rule with reference to X_t and Z_t
z	Height
Z_{bl}	Z blade axis, coaxial with the blade pitch axis
Z_{msh}	Z main shaft axis, Z_{bl} axis projection of the reference blade into the rotor plane
Z_n	Z nacelle axis, according to the right hand rule with reference to X_n and Y_n
Z_t	Z support structure axis, in direction of the tower axis, positive towards the tower top
α	Wind shear exponent
δ	Displacement
φ	Internal friction angle
γ'	Soil unit weight
η	Wave elevation
Λ	Logarithmic decrement of the structural damping
Λ_1	Longitudinal turbulence scale
θ	Phase of a harmonic wave
θ	Torsion
σ	Standard deviation
ω	Wave angular velocity
ξ	Damping ratio

Chapter 1

Introduction

1.1 General

The present report deals with the analysis of the loads on the wind turbines at the Arklow Bank Offshore Wind Farm. As a demonstration plant, a big measuring campaign has been carried out for a better understanding of the behaviour of the turbines under offshore conditions. During this measuring campaign, especial attention has been paid to load measurements, as they represent a key issue for the verification of the quality of the design of the turbines. A too conservative estimation of the loads would lead to an inefficient design with higher material cost in the construction of the turbines. On the other hand, an underestimation of the loads will lead to undersized components of the turbine, with risk of structural failure. Obviously, the first option offers a structurally more conservative design, as it guarantees a safer performance of the turbines, though at higher costs. However, the objective of every designer is to obtain a design with the required performance at the lowest costs; therefore an optimal solution should be achieved.

In order to be as close as possible to the ideal optimal solution, a better understanding of the loads on offshore wind turbines is needed. Nowadays, several safety factors are included in the design phase to ensure that the design remains on the safe side (the conservative one). However, a better prediction of the loads that a wind turbine will experience during its lifetime will allow a more efficient design, with lesser use of materials.

1.2 Objectives and general approach

1.2.1 Objectives

According to the project outline [1], there are three main objectives of the thesis:

1. Estimation of the difference in fatigue damage and natural frequencies predicted in the design phase of the Arklow Bank Offshore Wind Farm, and those determined from measurements.

2. Identification of sources of error in fatigue damage and natural frequencies prediction during the design phase of the Arklow Bank Offshore Wind Farm, especially related to the offshore environment.

3. Identification of important design parameters for an improvement on the design of future offshore wind farms, found through simulations and comparisons with measurements at the Arklow Bank Offshore Wind Farm.

Initially, an analysis of extreme loads was also included as an objective of the thesis. However, due to the lack of extreme events during the measuring campaign, the extreme events analysis have been substituted by a study of the most severe measured sea states, in terms of fatigue damage.

In addition, fatigue analysis is limited to the short term fatigue damage. The measuring campaign on turbine 1 has not been long enough to ensure reliable long term predictions. Therefore, no long term comparisons between the fatigue damage predicted during the design phase, and the fatigue damage calculated from measured loads, are carried out.

1.2.2 General approach

In order to achieve the objectives, the strategy to be followed consists of five steps:

1. **Verification of the environmental conditions at the Arklow Bank site**. Data provided by the measuring campaign are analyzed, and compared with design weather conditions.

2. **Analysis of natural frequencies of turbine 1**. Natural frequencies of the turbine are obtained through spectral analysis of the different subsystems, and compared with natural frequencies predicted by simulations and by design.

3. **FLEX5 GE3.6s model tuning**. The FLEX5 model of the 3.6s turbine used in the design phase is tuned in order to better reproduce the behaviour of the turbine. Results from the environmental analysis and the assessment of natural frequencies are used for tuning purposes.

4. **Short term fatigue analysis**. Few load cases (preferably as close as possible to design load cases) from the measurements are identified for further analysis, including simulations with both design and tuned models.

5. **Analysis of severe sea states**. Few load cases with the harshest measured weather conditions are identified. The analysis includes comparisons in terms of fatigue damage of measured and simulated loads, with both design and tuned models.

Chapter 2

The Arklow Bank Offshore Wind Farm

2.1 Wind farm overview

During 2004, the Arklow Bank Offshore Wind Farm, the world's first offshore wind farm using turbines in excess of 3 MW, was installed about 10 km off the coast of Arklow, on the East of Ireland. The project was co-developed by GE Energy and Airtricity, and built and run by GE Energy as a demonstration wind farm for their 3.6 MW machines. Zeusford, a company owned 50% by Airtricity and ACCIONA, holds an option to purchase the wind farm after certification, testing and demonstration is complete.

The Arklow Bank Offshore Wind Farm uses seven GE 3.6 MW units, the largest turbines commercially installed at sea until the Beatrice wind farm (on the Scottish coast) was installed in the summer of 2006. The water depths at the seven turbines range between 3.7 m and 6.2 m, with respect to the MSL. The 25 MW facility was developed as Phase I of a much larger offshore project (520 MW), which has been postponed for the moment. It represented Ireland's first offshore wind project, and generates enough electricity to serve the energy needs of about 16,000 average Irish households, avoiding the annual release of approximately 68,000 tons of CO_2 into the atmosphere. The main characteristics of the wind farm and the GE 3.6s wind turbine are presented in table 2.1.

The wind farm is connected to ESB Networks (the Irish Distribution System Operator) via the Arklow National Grid Substation. The connection to the shore is done by means of a submarine cable. From shore, connection occurs through an underground cable.

2.2 GE 3.6s wind turbine

The Arklow Bank Offshore Wind Farm comprises seven GE 3.6s offshore wind turbines. The turbines are erected on driven monopiles, connected to the wind

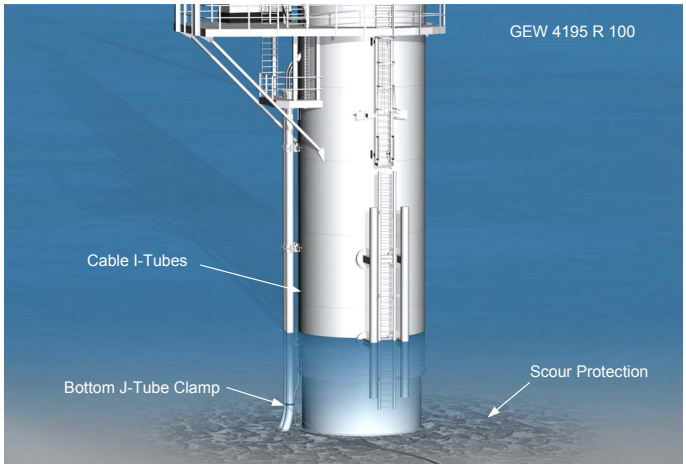

Figure 2.1 Transition piece and monopile of the GE 3.6s wind turbine [3].

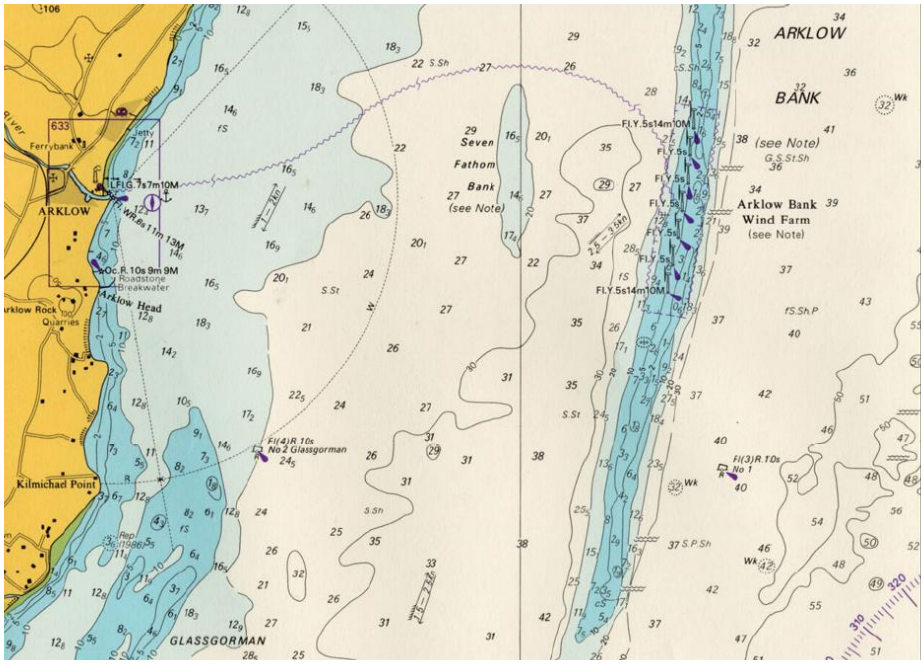

Figure 2.2 Location of the Arklow Bank Offshore Wind Farm [4].

Table 2.1 Main data of the wind turbine [2].

Model	3.6s offshore
Wind turbine class	IEC TC IIA / TC IB
Generator power [kW]	3,600
Rotor concept	3-blade, rigid hub, up-wind, active yaw
Rotor speed range [rpm]	8.5 – 15.3
Control concept	Variable-speed, variable-pitch
Cut-in wind speed [m/s]	3.5
Rated wind speed [m/s]	14.0
Cut-out wind speed [m/s]	25.0 (30 s average)
Rotor diameter [m]	104
Hub height w.r.t. MSL [m]	73.5
Nacelle and rotor weight [t]	290

turbine tower by the so-called transition piece, which aims at compensating imperfections on the monopile head (due to the hammering installation process) and correcting slight deviations of the monopile from the vertical direction. The transition piece has several pre-mounted ancillary structures (see figure 2.1):

- Boat landing arrangement, ladders and platform, which together allow boat access to the turbine for maintenance activities
- J-tubes, which provide cable access to the tower from the seabed
- Cathodic protection against corrosion
- Turbine tower flange, which constitutes the connection between the tower and the transition piece

The transition piece is fixed to the monopile by means of a grouted joint, which uses a high-strength concrete-like material. This joint provides a large flexibility, allowing adjustment of both vertical and horizontal inaccuracies.

All seven turbines have been expected to suffer severe scour, therefore scour protection has been provided at all locations. The scour protection consisted of a 1 m deep filter layer in a 12 m wide ring of rock armour around the monopile, in an excavated pit so that the top of the filter layer was flush with the top of the sand bed.

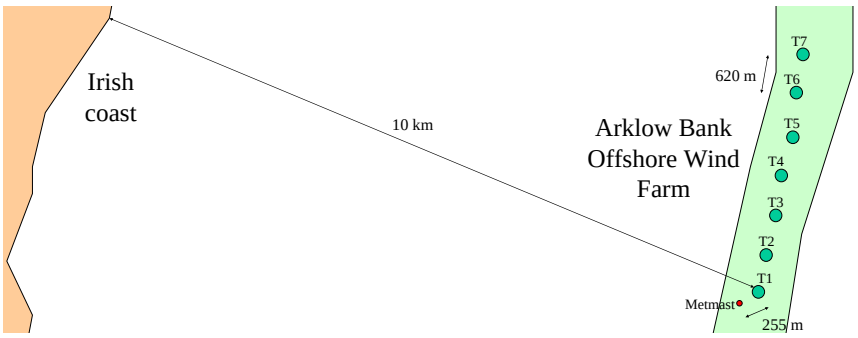

Figure 2.3 Schematic wind farm layout and location.

2.3 Site and environment

The Arklow Bank Offshore Wind Farm is located 10 km off the coast of Arklow, on the East of Ireland (see figures 2.2 and 2.3). The Arklow Bank is a sand bank of about 20 km long and 2.5 km wide in the Irish Sea, parallelly oriented to the coastline. The water depth within the bank ranges between –25 m (with reference to Mean Sea Level, MSL) to –1.5 m MSL; however, the water depth at turbine locations varies between –3.7 m and –6.2 m. The mid-section of the bank, where the turbines have been installed, has an asymmetric profile, with a steeper slope on the eastern side than on the western one.

Table 2.2 Main design environmental parameters of the Arklow Bank site [2].

Parameter	**Value**
U_{mean} at hub height[a] [m/s]	8.6
Weibull shape factor k	2.08
Wind shear exponent α	0.12
U_{ref}[b] [m/s]	46.1
H_{s50}[c] [m]	6.9
T_{z50}[d] [s]	8.9

[a] Annual mean wind speed at hub height (73.5 m above MSL)
[b] Extreme 10 min mean wind speed at hub height, with a return period of 50 years
[c] Extreme 1 h significant wave height, with a return period of 50 years
[d] 1 h zero up-crossing period associated with H_{s50}

Table 2.2 shows a brief summary of the most important environmental data used in the design of the wind farm, according to Seidel and Böker [2]. The

annual wind speed on the Arklow Bank site at the turbines' hub height (that is, 73.5 m above MSL) is 8.6 m/s. The wave height in the area of the bank is rather low, as the relatively shallow waters do not allow big waves. The flow direction over the bank ranges from E – W (East – West) to ENE – WSW (East-northeast – West-southwest), with a maximum measured current of 2.0 m/s. Site investigations carried out by FUGRO in 2001 along the whole bank, together with CPT (cone penetrometer tests) data from Seacore and Svirtzer on each turbine location, have been used in order to derive the design soil conditions. At the turbine locations, the soil is formed by several layers ranging from medium dense to very dense sand. No sea ice or earthquake is expected.

Chapter 3

Measurement system

In order to study the behaviour of the turbines, and the support structures, under offshore conditions, a broad measuring campaign has been carried out by WINDTEST Kaiser-Wilhelm-Koog GmbH. Starting on 01/07/2004 until 31/03/2005 (although with several periods in between without measurements), the measuring campaign focused on structural loads on turbine 1 (the most southern one) of the wind farm. However, the available data for the present report only cover the period 09/09/2004 to 18/03/2005. Results from data processing for the period 09/09/2004 to 12/12/2004 are found in the WINDTEST report [4]. Load measurements were performed in accordance to the IEC 61400-13 standards.

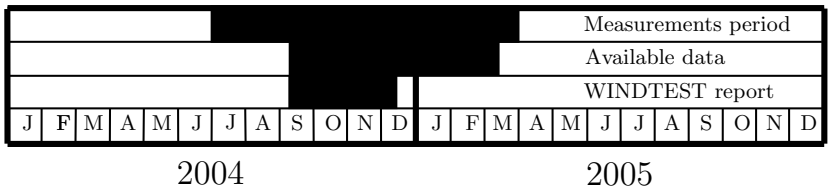

Figure 3.1 Cronogram of the different periods related to measurements analysis.

3.1 Metmast

A meteorological mast of 73 m height (w.r.t. MSL) has been installed at the Arklow Bank Offshore Wind Farm. The metmast is located 255 m (i.e. approx. 2.45·D) away from the nearest turbine (turbine 1), in the 246° direction.

The metmast consists of a lattice tower placed on top of a monopile, where the meteorological sensors are located at different heights. These sensors include:

- 3 Thies and 3 Risø anemometers, placed at three different heights (30 m, 52 m and 73.5 m w.r.t. MSL)

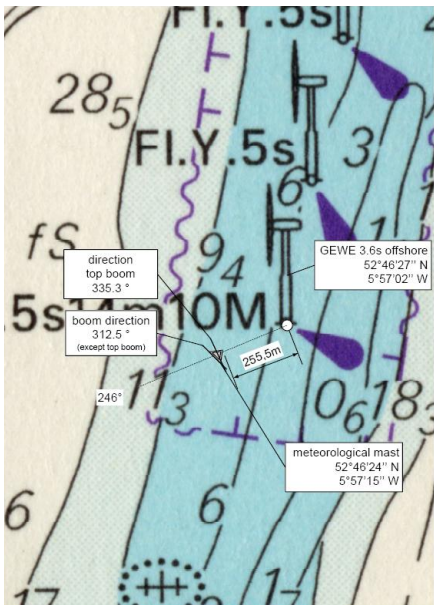

Figure 3.2 Location of turbine 1 and metmast [4].

- one Gill ultra sonic anemometer (at 73.5 m height)
- 3 potentiometric wind vanes, placed at three different heights (27 m, 48 m and 70 m)
- one precipitation sensor, at 18 m height
- two temperature sensors, at 18 m and 70 m height

3.2 Relevant sensors and signals

Besides the sensors on the metmast, additional sensors have been installed in turbine 1, mainly regarding load measurements, but also weather conditions. Moreover, operational data are obtained from the control system. Altogether, they come to 56 different measurements channels, the most important of which are shown in tables 3.1, 3.2 and 3.3.

From table 3.1 it can be seen that the rotor position is measured with an inductive sensor located on the rotor flange. The absolute position of the rotor is determined by combining this signal with the digital pulses from the rotating angle sensor located at the gearbox. In addition, the sensor measuring the yaw position was not working properly during the measurements period. For all the calculations shown in this report, an assumption of no yaw misalignment was made.

The wave height (see table 3.2) has been measured with a sensor located on the turbine platform. The actual measurement gives the distance between the sensor and the water surface, and therefore, this signal needs to be processed

Table 3.1 Operational measurements categories [4].

Signal	Signal type	Sensor	Sensor location
Brake pressure	Analog	Pressure transformer	Braking system
Electric power	Analog	Power transducer	—
Generator speed	Analog	Control system	—
Pitch angle	Analog	Control system	Pitching system
Rotor position	Analog	Inductive sensor	Rotor flange
Yaw position [a]	Analog	Rotation angle sensor	Yaw gear wheel
Failure	Digital	Control system	—
Status: Availability	Digital	Control system	—
Status: Grid connect.	Digital	Control system	—
Status: Manual stop	Digital	Control system	—

[a] The yaw position signal was errored for the period of this report

Table 3.2 Environmental measurements categories [4].

Signal	Signal type	Sensor	Sensor location
Barometric pressure	Analog	Barometer	Turbine [a]
Temperature	Analog	Resistance thermometer	Metmast [b]
Wave height	Analog	Radar	Turbine platform
Wind direction	Analog	Wind vane	Metmast [c]
Wind direction	Analog	Wind vane	Nacelle [d]
Wind speed	Analog	Risø anemometer	Metmast [e]
Wind speed	Analog	Thies anemometer	Metmast [e]
Wind speed	Analog	Sonic anemometer	Metmast [f]
Wind speed	Analog	Cup anemometer	Nacelle [d]
Precipitation	Digital	Rain sensor	Metmast

[a] At 18 m, with reference to MSL
[b] At 18 m and 70 m height, w.r.t. MSL
[c] At 27 m, 47 m and 70 m height, w.r.t. MSL
[d] On both the port and the starboard side
[e] At 30 m, 52 m and 73 m height, w.r.t. MSL
[f] At 73 m height, w.r.t. MSL

Table 3.3 Load measurements categories [4].

Signal	Signal type	Sensor	Sensor location
Acceleration [a]	Analog	Acceleration sensor	Main frame
Blade bending	Analog	Strain gauges Fixed resistors	Blade root
Main shaft bending	Analog	Strain gauges	Main shaft (inner)
Main shaft torsional	Analog	Strain gauges	Main shaft (outer)
Monopile bending	Analog	Strain gauges	Monopile (inner)
Tower bending	Analog	Strain gauges	Tower (inner)
Tower torsional	Analog	Strain gauges	Tower (inner)

[a] In the wind direction and in direction perpendicular to the wind

in order to obtain the wave parameters, namely, the significant wave height H_s and the zero up-crossing period T_z. No wave direction sensor has been used, hence impeding the study of the influence of wind and waves misalignment on the behaviour of the turbines.

On the other hand, the accuracy of the wind vanes and anemometers located on top of the nacelle is rather limited, due to high turbulence created by the rotation of the rotor, and the nacelle itself. This limited reliability also applies to the rain sensor, which is often used by seagulls as a resting point.

All bending moments (table 3.3) have been measured in two approximately perpendicular directions. In the case of the monopile, the strain gauges have been placed in four different directions.

3.3 Calibration of load measuring systems

3.3.1 Rotorblade bending

The strain gauges applied for measuring the bending moments of the blades have been placed inside the blade root, and wired as full-bridges. Some damaged strain gauges for edgewise bending moments in two blades (blades 16 and 20[1]) have been replaced by fixed resistors.

The position of the edgewise bending gauges have been deviated 10^o from the 0^o direction, as the edgewise seam of the rotorblade is not appropriate for load measurements (see figure 3.3b).

[1] The blades from all seven turbines of the wind farm are numbered for an easier identification. The blades from turbine 1 are blades 16 (blade X), 18 (blade Y) and 20 (blade Z).

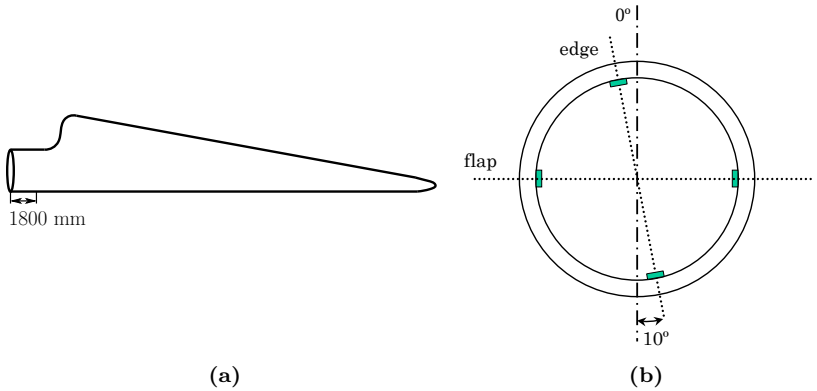

Figure 3.3 Strain gauges position on the blade: (a) longitudinal direction (b) cross section.

The variable pitch angle, together with the influence of crosstalk[2] and temperature effects, make the calculation of new signals necessary in order to obtain the actual edgewise and flapwise bending moments.

The edgewise and flapwise calibration was done at low wind speeds, by idling the rotor with pitch angles of 0º (for edgewise bending moments) and 90º (for flapwise). Gravitational moments were calculated from the weight protocols of the blades (enclosure 4 of [4]).

3.3.2 Main shaft bending and torsion

For the measurement of bending moments on the main shaft, two perpendicular full-bridges were installed in the inner part of the shaft. In addition, another full-bridge was installed in the outer part of the main shaft, in order to measure torsional moments (see figure 3.4).

The calibration of the sensors was made by means of precision shunt resistors.

3.3.3 Tower bending and torsion

In order to measure the bending moments on the bottom of the tower, two full-bridges have been installed inside the tower in the 80º/260º and 170º/350º directions (see figure 3.5a), at 0.9 m over the bottom flange of the tower.

One full-bridge for the measurement of the torsional moments on the tower have been installed at a distance of 6.9 m below the tower top flange.

In both cases, the calibration of the sensors was made by means of precision shunt resistors.

[2] The crosstalk effect is caused by an influence of the signal of edgewise bending moment on the signal of the flapwise bending moment, and viceversa, due to the 10º deviation of the edgewise sensors from the 0º direction.

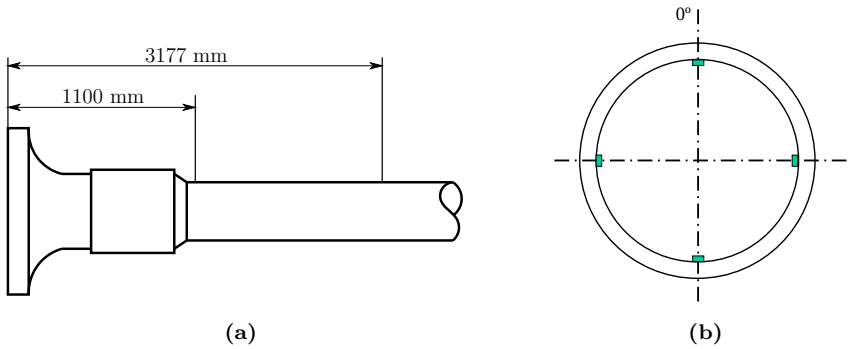

Figure 3.4 Strain gauges position on the main shaft: (a) longitudinal direction (b) cross section.

3.3.4 Monopile bending

Eight half-bridges were installed in the inner side of the monopile for bending moments measuring purposes, at a distance of 11.46 m from the monopile top. These half-bridges were applied approximately each 45º, connecting opposite half-bridges to full-bridges (see figure 3.5b).

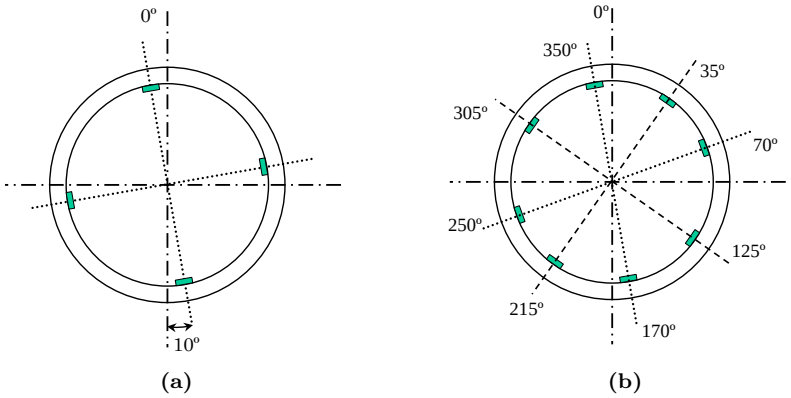

Figure 3.5 Strain gauges for bending moments measurement: (a) tower (b) monopile.

A sketch of the locations of the sensors on the support structure is shown in figure 3.6. It should be pointed out that the directions shown in this figure have no correspondency with cardinal directions.

3.4 Data acquisition

The schematic configuration of the data acquisition system from WINDTEST Kaiser-Koog is shown in figure 3.7. The data acquisition system is based on a data logger with 32 analog inputs, 32 status inputs and 4 frequency inputs. For the measurements in the hub an extra module with 12 analog channels was

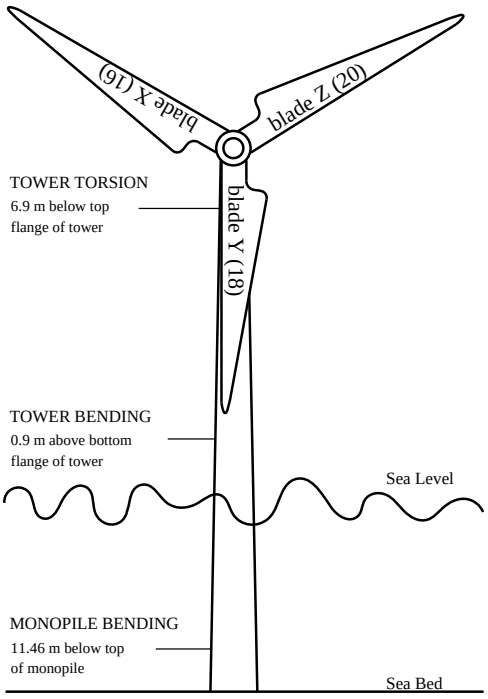

Figure 3.6 Location of strain gauges for bending moments measurement on the support structure [4].

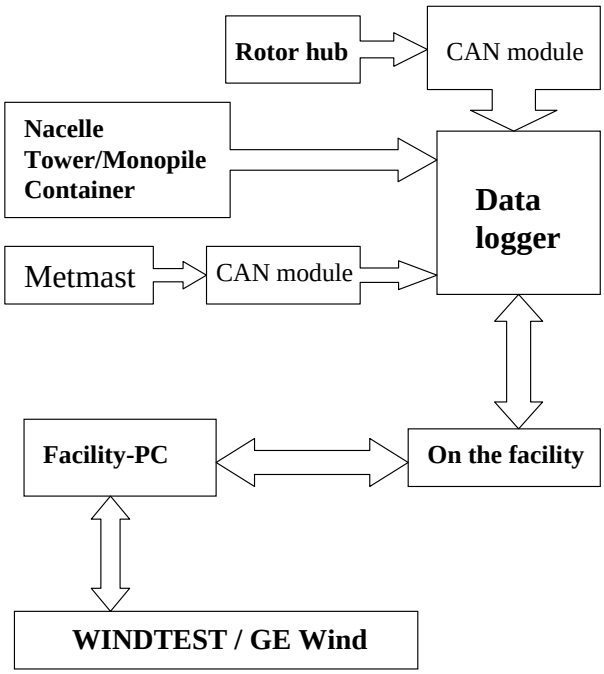

Figure 3.7 Schematic layout of the measurement system.

installed. A two wire line (CAN) transmits the data from this module to the main unit in the tower bottom.

Two other modules (CAN), each one having 12 analog channels, were installed at the metmast. A glass fiber cable transmits data from the metmast to turbine 1. The hard disk of the main unit stores directly connected signals together with all CAN-signals.

All measurements are controlled by a personal computer located at the bottom of the tower. This computer stores all rawdata and statistic files transmitted, which can be checked by remote control. Measured data are stored in 10-min-period files of 4.39 MB of size, in FAMOS format. The complete rawdata are frequently streamed and restored at WINDTEST for further processing. The sampling rate of the transferred signals is variable up to 80 kHz. Measured data are frequently checked on plausibility.

3.5 Restrictions

For the evaluation in this report the following data sets have been discarded [4]:

- Data sets outside the period 09/09/2004 to 18/03/2005, because they are not reliable enough (not complying with IEC standards).
- Wind data sets inside the 36^o – 96^o sector, because the metmast would be in the wake of the turbine
- Data sets with a length smaller than 10 min.

Some data sets have been discarded for specific analyses, but not for others. For example, data sets where the wave sensor was not working have been used anyway for natural frequencies analysis, but not for the analysis of weather conditions.

It is important to highlight that although the WINDTEST report [4] limited its results to the 200^o – 290^o sector, in the present report only those data referring to the operation of the metmast in the wake of the turbine have been discarded.

Chapter 4

Verification of environmental conditions at the Arklow Bank site

As explained in chapter 3, the measurement campaign lasted 6 months, although the available data for this study cover the period from 09/09/2004 to 18/03/2005, with interruptions. In the present chapter the results of the analysis of both wind and wave data for this period are shown, together with the soil conditions.

4.1 Wind

As seen in table 3.2, there are three different anemometers at hub height. Unless stated otherwise, only the *Risø anemometer* results are shown in this report due to comparison purposes, as it is the one used in the WINDTEST report [4].

The analysis has been based on 10 minutes averages of four different wind parameters: *wind speed*, *wind direction*, *wind shear* and *turbulence intensity*. Unless stated otherwise (e.g. for the wind direction analysis), the 36º – 96º sector is excluded from the analysis, in order to avoid wake effects of turbine 1 on the anemometers placed on the metmast.

4.1.1 Wind speed distribution

In order to model the behaviour of the wind speed at a specific site during the year, two different probability distributions are commonly used in wind analysis: the *Rayleigh* and the *Weibull* distributions. Both of them are used to represent the variations of either the 10 min average or the hourly mean wind speed over a year. The Weibull distribution is based on two parameters (the scale factor A, and the shape factor k), whilst the Rayleigh distribution uses only one (the annual mean wind speed U_{mean}). This makes the Weibull distribution more versatile, whilst the Rayleigh is easier to use.

Table 4.1 Mean wind speed and parameters of the probability distributions for the wind speed.

Distribution	**k**	**A [m/s]**	**U_{mean} [m/s]**
Weibull energy	2.22	10.65	9.43
Weibull standard deviation	2.26	10.65	9.43
Rayleigh	2.00	10.65	9.43
Weibull design	2.08	9.7	8.60

The Weibull probability density function and the cumulative distribution function are given by:

$$p\left(U\right) = \left(\frac{k}{A}\right)\left(\frac{U}{A}\right)^{k-1} exp\left[-\left(\frac{U}{A}\right)^{k}\right] \tag{4.1}$$

$$F\left(U\right) = 1 - exp\left[-\left(\frac{U}{A}\right)^{k}\right] \tag{4.2}$$

The Rayleigh distribution is a specific case of the Weibull, when k is 2 and the scale factor satisfies the following condition:

$$A = \frac{2}{\sqrt{\pi}} U_{mean} \tag{4.3}$$

Figure 4.1 shows the measured wind speed frequency distribution at hub height, together with four different probability distributions (one Rayleigh and two Weibull distributions built out of on-site measurements, and one Weibull distribution used for design) which approximate it. The two Weibull distributions built with measured data have been calculated with two different methods (explained in Appendix B): the *standard deviation method* is applied for one of them, while the other one has been calculated with the *energy density method*. As can be seen from figure 4.1 both Weibull distributions look very similar, and they approximate better to the actual wind speed frequency distribution than the Rayleigh one. Obviously, these two Weibull distributions also match better to the measured wind speed frequency distribution than the design wind speed distribution. The design *annual* mean wind speed at hub height used for design is 8.60 m/s, whilst the mean wind speed *for the measurements period* is 9.43 m/s. The design distribution gives higher probabilities at lower wind speeds than the distributions built out of measurements, and lower probabilities at higher wind speeds. Nevertheless, the design distribution is anyway close enough to the measured wind speed frequency distribution, and therefore it can be concluded that wind speed conditions from design and measurements are comparable. Table 4.1 shows the scale and shape factors of the distributions plotted in figure 4.1.

4.1.2 Wind direction

For the wind direction analysis, all sectors (including the 36º – 96º) are analyzed. Therefore, the relative importance of the exclusion of that particular sector from the general wind analysis can be assessed.

As can be seen from figure 4.2, most probable wind directions at hub height are in the region 180º – 240º (where 0º corresponds to North), with a maximum for the 210º direction. It can also be seen that the prevailing wind direction does not change with increasing heights. Actually, the wind rose is very similar at both 27 m and 70 m, showing slight deviations at 47 m, where both the 180º and 210º directions share the same percentage of occurrence. In addition, the 36º – 96º sector represents approximately the 4.2% of the total occurrences at hub height, and therefore no big influence is expected from its exclusion from the analysis.

The design wind rose, also plotted in figure 4.2, shows a good agreement with the measurements in the region 30º – 210º. However the design wind rose reflects a much higher probability of northern winds, as well as lower probabilities for winds in the 240º, 300º and 330º directions. In conclusion, the design wind rose matches the measured ones for the prevailing wind direction (210º direction), though some significant differences arise in the 240º – 0º region.

The prevailing wind direction at hub height is parallel to the coast line, which is also the direction of alignment of the wind farm. This means that the wind turbines are often operating in wake, which is not relevant for the present study, as the studied turbine is the first of the alignment, receiving the free wind stream. On the other hand, no wind and waves misalignment has been considered for design. No verification of this assumption can be carried out, as no wave direction has been measured. However, this assumption would imply that long fetch sea states (that is, developed sea states) would be commonly occurring at the Arklow Bank site.

4.1.3 Wind shear

Wind shear stands for the increase of the mean wind speed with height. For the estimation of the wind shear, two mathematical models are normally applied: the *logarithmic law*, and the *power law*.

In the present report only the *power law* has been applied. Its basic form is:

$$\frac{U(z)}{U(z_r)} = \left(\frac{z}{z_r}\right)^{\alpha} \tag{4.4}$$

where $U(z)$ is the wind speed at height z, $U(z_r)$ is the reference wind speed at height z_r and α is the power law exponent.

The wind shear is estimated by using the measurements from the anemometers at three different heights (see table 3.2). Only those cases in which the wind speed is increasing with height are taken into account. The α is calculated by a linear fit, after taking logarithms on the power law:

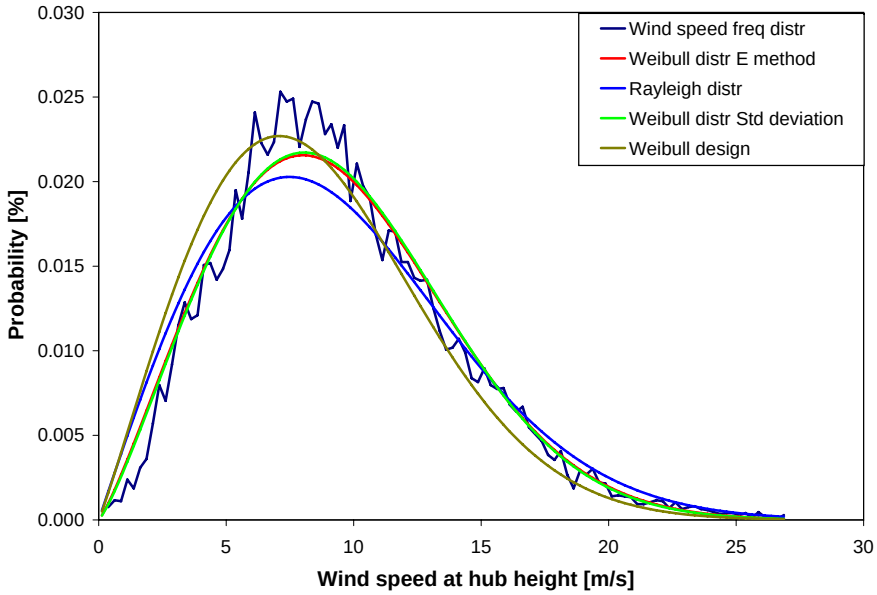

Figure 4.1 Probability distributions for the wind speed at hub height, from design and from measurements (Risø anemometer).

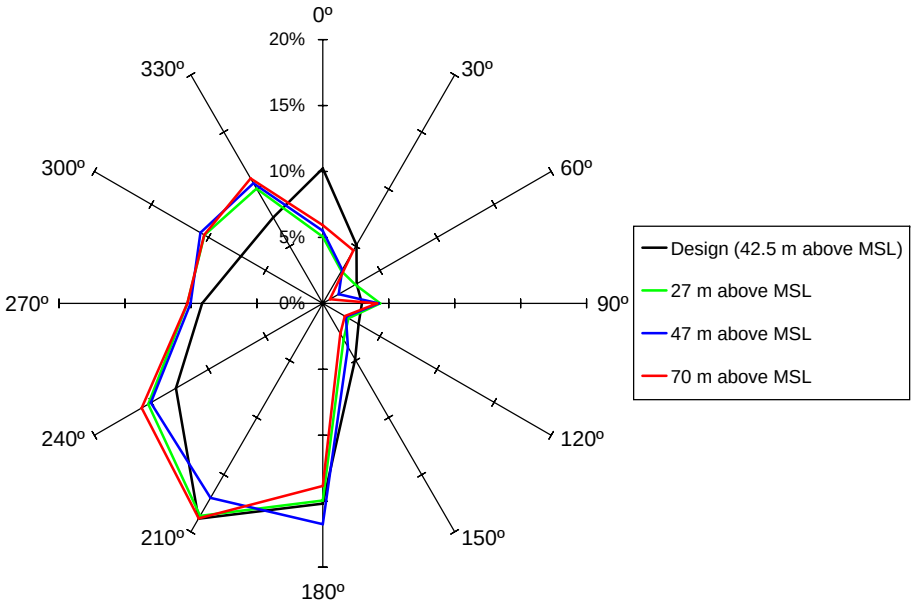

Figure 4.2 Measured wind rose for the Arklow Bank site

$$log\left(\frac{U\left(z\right)}{U\left(z_r\right)}\right) = \alpha \cdot log\left(\left(\frac{z}{z_r}\right)\right) \tag{4.5}$$

The design shear exponent has been taken as 0.12. This value was obtained as the average of the 12 directional α calculated by Garrad Hassan [5], based on the results from a WAsP wind flow model. The design value matches the values of the α obtained from measurements for the 0° direction and in the range 150° – 210°. However, there is a strong mismatching between measurements and design for the 90° and 120° directions. Furthermore, no explanation for the high average values of the wind shear exponent in the 90° and 120° directions has been found, as no obstacles are expected in those directions.

4.1.4 Turbulence intensity

Turbulence refers to fast wind speed variations, typically on a 10 minutes timescale, generated by friction with the earth's surface or by thermal effects. Turbulence intensity is the most basic measure of turbulence, defined as

$$I = \frac{\sigma}{\bar{U}} \tag{4.6}$$

where σ is the standard deviation of the wind speed fluctuations around the 10-min mean wind speed $\bar{U}$.

For design, the so-called *wake turbulence intensity 6D (including background)* is calculated with the Sten Frandsen model. This model allows the estimation of the effective turbulence intensity inside the wind farm layout. For the particular case of Aklow Bank, a worst case of eight neighbour wind turbines has been considered. This corresponds to the wind farm layout for Phase II of the project, which would imply an extension of the current wind farm by 26 further turbines. The *wake turbulence intensity 6D (including background)* is considered as design turbulence intensity, accounting for the ambient characteristic turbulence intensity, the background turbulence from the whole wind farm and a continuous $6 \cdot D$ wake operation. However, the machinery and the blades have been checked with the IEC 61400-1 ed.2 TC 1 B turbulence intensity.

In figure 4.4 large differences arise between the design turbulence intensity (*Wake I 6D (incl. background)*) and the measurements (*I measurements*), especially in the partial load range (below 14 m/s). Differences become much smaller for wind speeds above 18 m/s. In addition, a good match between design turbulence intensity and the turbulence intensity calculated according to IEC 61400-1 ed.2 TC 1 B (*IEC B* in the figure) is observed for the partial load range. Finally, there are not significant differences between the turbulence intensity measured before the installation of the wind farm (*I before design* in figure 4.4) and during the measurement campaign (*I measurements*) for the whole operation range.

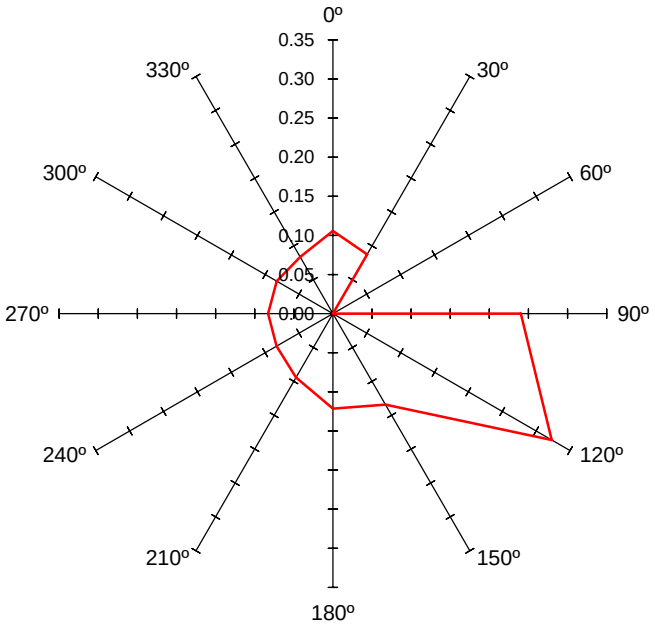

Figure 4.3 Mean shear exponent in different directions at the Arklow Bank site.

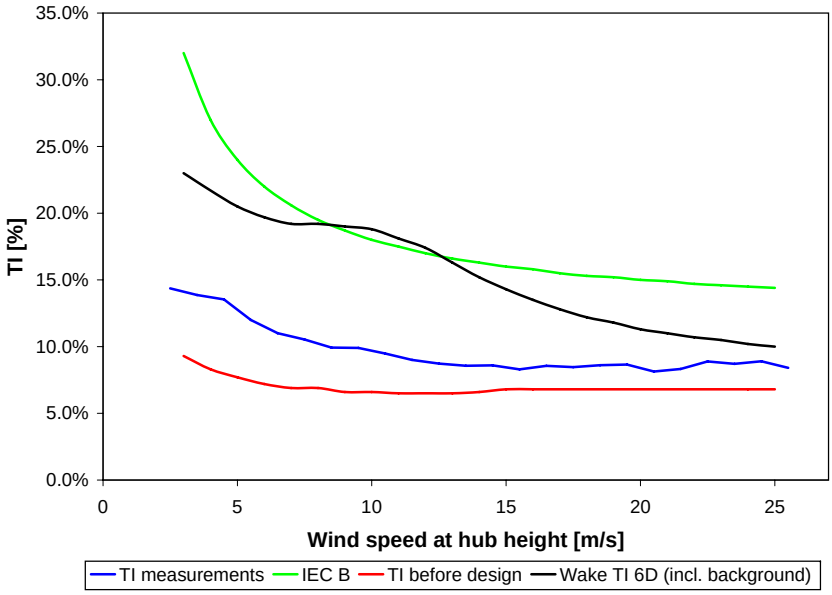

Figure 4.4 Turbulence intensities at the Arklow Bank site.

4.2 Water level variations

As specified in table 3.2, the waves sensor consists of a radar located on the turbine platform, pointing downwards. The radar sends a beam that gets reflected on the water surface, registering the time that it takes to get back. The distance between the radar and the water surface is then calculated based on this time. The radar has a measuring frequency of 9 Hz, and an accuracy of $\pm$6 mm. However, the frequency with which the data acquisition system collects the measurements from the wave sensor is 50 Hz, and therefore those data have been filtered back to 4 Hz in order to get reliable information.

As mentioned before, the sensor is located at the turbine platform, which according to the support structure certification document [6] is at 13.20 m above MSL. However, the mean measured distance from the sensor to the water surface is 15.87 m. The assumption of this value as correct would imply the whole structure to be shifted 2.67 m up. This would mean that the transition piece would be most part of the time completely out of the water, which is quite improbable. Therefore, the support structure certification document is taken as correct, and a +2.67 m offset in the waves sensor measurements is assumed.

Four different water-level-related parameters have been calculated: *still water level*, *water depth*, *significant wave height* and *zero up-crossing period*. No wave direction measurements have been performed. In addition, for the current study the sea state period has been set to 1 h, and therefore, all the water level parameters refer to a 1-h period.

The wave sensor has been available only around 43% of the time during the measurement campaign, which means only 2 months and 21 days of complete measurements.

4.2.1 Water depth and still water level

During the measuring campaign, the *water depth* has been measured twice (once in the beginning of the period, the other one near the end). Therefore, the measured water depth has been assumed to be constant during the whole measurements period, with a value of 5.25 m (with reference to the MSL). Nevertheless, the design *water depth* used for the fatigue analysis was 9.30 m, much higher than what actually is measured. This design water depth is calculated on the basis of the maximum nominal water depth for all the seven turbines of the wind farm (6.2 m, for turbine 3), with additional 2 m accounting for the possibility of sand waves, and 1.1 m for general uncertainties. No significant variation of the seabed level is detected in the measurements (probably due to the action of the scour protection, explained in section 2.2). However, no long term extrapolations can be carried out, due to both the insufficient amount of data (only two bathymetry surveys have been carried out during the measuring campaign) and the insufficient length of the measurements period.

The *still water level* varies in time, mainly due to the effect of the tide, but also due to storm surges. It has been calculated by determining the mean distance from the radar to the water surface for every 1-h period. This value was corrected in order to refer it to the MSL (mean sea level) instead of to the

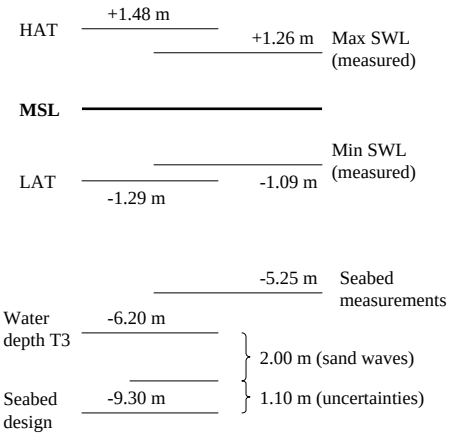

Figure 4.5 Water depths and water levels at the Arklow Bank site.

turbine platform, and in order to account for the aforementioned +2.67 m offset of the sensor. The MSL was taken as the mean distance from the radar to the water surface for the whole measuring campaign period.

The maximum still water level (*Max SWL* in figure 4.5) for the measurements period is +1.26 m, while the design *highest astronomical tide* (HAT) was +1.48 m. On the other hand, the minimum measured still water level (*Min SWL* in figure 4.5) is -1.09 m, while the design *lowest astronomical tide* (LAT) was -1.29 m. Hence measurements show a good agreement with design values. Finally, from both the measurements and the design values it can be concluded that the tide variations at the Arklow Bank site are quite mild.

4.2.2 Significant wave height

The *significant wave height* is defined as the mean of the 1/3 highest waves in the time series (w.r.t. the still water level of the 1-h sea state), which can also be estimated as

$$H_s \approx 4 \cdot \sigma \tag{4.7}$$

where σ represents the standard deviation of the time series.

The maximum significant wave height registered during the measurement campaign lays around 2.5 m, for wind speeds around 27 m/s. However, the maximum design significant wave height used for fatigue analysis is 6.81 m, for wind speeds higher than 25 m/s. Therefore, large discrepancies in the significant wave height between design and measured values are observed. Moreover, the maximum design H_s is higher than the measured water depth at turbine 1. This is in contradiction with expression 4.8, which gives an estimation of the maximum *regular* wave for a particular water depth:

$$H_{reg,max} = 0.78 \cdot d \tag{4.8}$$

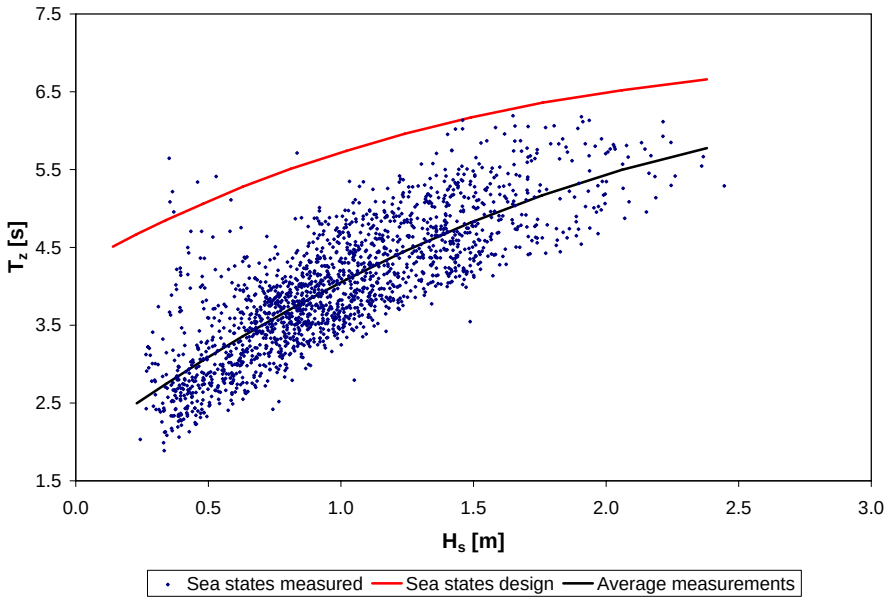

Figure 4.6 Design versus measured H_s and T_z at the Arklow Bank site.

where d represents the water depth.

Taking into account that the value obtained from expression 4.8 is related to a single wave, whilst the H_s is a mean over a 1 h period, it seems quite improbable that design significant wave heights actually occur.

4.2.3 Zero up-crossing period

The zero up-crossing period is defined as the mean time between two zero up-crossings. An up-crossing occurs whenever the water surface is crossing the still water level upwards. The zero up-crossing period can be calculated as follows

$$T_z = \frac{t_{series}}{n_0} \tag{4.9}$$

where t_{series} represents the length of the time series, and n_0 is the number of zero up-crossings.

The zero up-crossing period and the significant wave height are not directly correlated, although they are not completely independent parameters. In figure 4.6 a correlation between both parameters is derived from measured sea states. This correlation is obviously not reliable enough to be applied in accurate calculations, but it is useful for getting an idea of how the sea states look like at the site. It can also be observed that although the points representing sea states do not stick to one straight line, they lay inside a certain region. When looking at the sea states used for design, it turns out that they represent the upper limit for this region where the measured sea states are enclosed.

4.3 Currents

No current sensor has been installed at the Arklow Bank Offshore Wind Farm. Therefore, the available data come only from the measurements carried out during the wind farm development project. The maximum current speed recorded was 2.0 m/s, with flow directions ranging from E – W to ENE – WSW [7]. Nevertheless, the extreme current considered for design has been 2.3 m/s (see table 4.2).

Table 4.2 Current data used in design [2].

Current	**Speed**
Tidal current	1.5 m/s
Storm surge current	0.4 m/s
Other residual currents	0.2 m/s
Uncertainties	0.2 m/s
Total	2.3 m/s

4.4 Soil conditions

Two site investigations have been carried out at the Arklow Bank site. The results from the first one, made by FUGRO in 2000, have been used during the design phase, and are shown in table 4.3. According to FUGRO, the soil at the Arklow Bank consists basically of very dense sand, gravel and gravelly sand up to 26 m deep. Clay was found only in one borehole, between 17.9 and 18.7 m.

The latest investigation, carried out by Seacore in 2003, concluded that up to 30 m deep the bank was constituted by dense to very dense sand and gravelly sand. For higher depths, very dense sand interbedded with very stiff to hard clay was found.

4.5 Conclusions

The main conclusions that can be extracted from the analysis of the environmental conditions are summarized next:

1) Wind speed probability distributions built from measurements are similar to the design Weibull distribution. However, the mean wind speed for the whole mesurements period is 9.43 m/s, slightly higher than the annual mean wind speed considered in design (8.60 m/s). However, this difference could be due to the insufficient length of the measuring campaign. Some seasonal variations of the wind speed (i.e. spring and summer variations) are not accounted for in the value obtained from measurements.

Table 4.3 Soil conditions for design [2].

Soil profile	Soil	γ' [a] [kN/m^3]	φ [b] [deg]
0 – 5 m	Medium Dense Sand	9.0	33
5 – 12 m	Dense Sand	9.0	37
12 – 17 m	Dense Sand	9.0	39
17 – 24 m	Very Dense Sand	9.5	39
> 24 m	Very Dense Sand	10.0	41

[a] Effective soil unit weight
[b] Internal friction angle

2) From the wind direction analysis, it can be concluded that the 180º – 240º sector is predominant in both the measurements (50% of occurrences) and design (probability of 45%), with a prevailing wind direction at 210º. Furthermore, the 36º – 96º sector, excluded from the analysis to avoid wake effects on the metmast, only represents the 5% of occurrences, approximately.

3) A constant 0.12 wind shear exponent has been assumed for design. However, large directional differences on the α value are found in the measurements, especially for 90º and 120º directions. For the resting directions, the measured shear exponent ranges between 0.08 and 0.13.

4) The measured turbulence intensity shows good agreement with the mean turbulence intensity resulting from studies carried out before the design phase. However, for design purposes a much higher turbulence intensity is used. The initial project of the wind farm considered the installation of 33 turbines in two phases, with a layout in which the worst case would be represented by a turbine surrounded by other 8 neighbouring converters. Hence, the turbulence intensity used in the design accounted not only for the ambient turbulence, but also for the background turbulence of the entire wind farm and for a continuous $6 \cdot D$ wake operation. However, Phase II of the project has finally not been built, and therefore the design turbulence intensity seems to be too high for the current layout.

5) The water depth measured at turbine 1 of Arklow Bank (5.25 m) shows large discrepancy with design assumptions (9.30 m). No significant variations on the seabed level (including scour and sand waves) has been detected during the measuring campaign. Nevertheless, no long term extrapolations can be carried out mainly due to insufficient amount of data.

6) Large differences are also observed in the maximum significant wave height values obtained from measurements (2.5 m) and design (6.81 m). In this case, design values seem to be overestimated, as the maximum design H_s is larger than the measured water depth, which is in contradiction with expression 4.8. However, as stated in the previous point, no long term

extrapolations can be carried out, as the calculation of the maximum wave through equation 4.8 is based on the value of the water depth.

7) Finally, design sea states (accounting for H_s and T_z) represent the upper limit of the measured sea states in the range 0 – 2.5 m of significant wave height.

Chapter 5

Analysis of natural frequencies

The analysis of natural frequencies is focused on the support structure and blades. The analysis is based on the short term (10 min) structural response of the specific subsystem to well known wind and waves excitations. The aim of this analysis is the comparison of the values for the bending natural frequencies determined from measurements, with those values obtained from design and from simulations. No torsional natural frequencies have been studied.

The actual bending natural frequencies of the main shaft are determined from measurements, although due to the lack of design and simulation data for its bending moments and natural frequencies, this subsystem is finally discarded from the analysis.

Due to confidentiality issues, all values of the natural frequencies in this chapter are normalized with respect to design natural frequencies. For the support structure, the design first natural frequency (used for fatigue calculations) in both fore-aft and side-to-side directions is taken as the reference. For the blades, the reference is the design first natural frequency in flapwise direction.

5.1 Analysis of natural frequencies in design

The design natural frequencies of the blades are shown in table 5.1.

Table 5.1 Design blade natural frequencies, normalized w.r.t. the f_0 in flapwise direction.

	Flapwise	**Edgewise**
$\mathbf{f}_0$	1.00	1.66
$\mathbf{f}_1$	2.82	5.24

Table 5.2 Results of the modal analysis for the support structure from design, both in fore-aft and side-to-side directions, normalized w.r.t. the f_0 used for fatigue.

	soft, 110% mass	**extreme**	**fatigue**	**stiff**	**stiff, 90% mass**
Water level	12 m	12 m	9.5 m	3 m	3 m
Pile penetration	29 m	29 m	29 m	32 m	32 m
Masses	110%	100%	100%	100%	90%
Corrosion abrasion	full	full	half	no	no
Fouling	yes	yes	no	no	no
Thickness GJ [a]	45 mm	45 mm	45 mm	95 mm	95 mm
Soil conditions	lower bounds	lower bounds	lower bounds	upper bounds	upper bounds
$\mathbf{f}_0$	0.92	0.95	1.00	1.17	1.23
$\mathbf{f}_1$	4.87	4.98	5.71	7.58	7.90

[a] GJ stands for grouted joint

For the support structure, more severe cases than those expected in reality have been analyzed in the design phase, in order to achieve a robust design. Several parameters, as the water depth, soil conditions or masses, have been modified in order to predict their effect on the values of the natural frequencies. On table 5.2 the upper and lower limits calculated in the design phase for the natural frequencies of the support structure are shown.

5.2 Analysis of measurements

This section deals with the determination of the natural frequencies of the support structure and the blades from measurements. Two different cases are analyzed:

- *Turbine idling after shut down.* The first natural frequencies of the support structure and blades, together with the damping ratio of the support structure, are obtained from the analysis of a free vibration event, after a shut down of the turbine.
- *Turbine in operation.* The first and second natural frequencies of the support structure and the blades are determined from the spectral analysis of the loads on the turbine during normal operation.

In both cases, the design natural frequencies are used as a reference in order to relate the peaks found in the spectrum with the different subsystems. The

denotation of the loads on the blades, main shaft and support structure used in this chapter is described in Appendix A, based on information from [8].

5.2.1 Turbine idling after shut down

The 1st natural frequencies of the different subsystems can be easily identified from a free vibration event. However, the 2nd natural frequencies are better recognized from the load spectra of the turbine in operation. This paragraph deals with the analysis of the turbine shut down occurred on 31/10/2004 at 18:06. Although only the immediately following 110 s after the shut down are analyzed, this period should be long enough to clearly distinguish the natural frequencies of the different subsystems.

For the determination of the natural frequencies of the support structure, only the PSD of the bending moments on the tower bottom are used for the determination of the natural frequencies. The first natural frequencies of the support structure and blades (normalized w.r.t. the design natural frequencies) are shown in table 5.3.

Table 5.3 Measured natural frequencies after shut down, normalized w.r.t. the design natural frequencies.

	Blades		**Support structure**	
	Flapwise	**Edgewise**	**Fore-aft**	**Side-to-side**
$\mathbf{f}_0$	1.04	1.79	1.22	1.22

During this free vibration event, some interesting phenomena are observed on the time histories of the blade bending moments, both in flapwise and edgewise directions. This behaviour is explained in the next section.

5.2.1.1 Blades

Flapwise direction

The blade root bending moments in flapwise direction are shown in figure 5.1. In order to explain this figure, the variation of the generator speed after the shut down is shown in figure 5.2.

When the turbine is shut down due to insufficient wind speed, the blades are pitched to 85°. In the current case, this pitch angle is achieved at 490 s. In this situation, the blades are no longer oriented to the wind, and the rotor starts idling. However, due to its inertia the rotor takes some time in reducing its rotational speed. During this deceleration of the rotor and the subsequent idling conditions, the blade root bending moments in flapwise direction are mainly due to the dead weight of the blade. The gravitational forces on the blades, which are sinusoidal at constant rotor speed, are stretched due to the decreasing rotational speed.

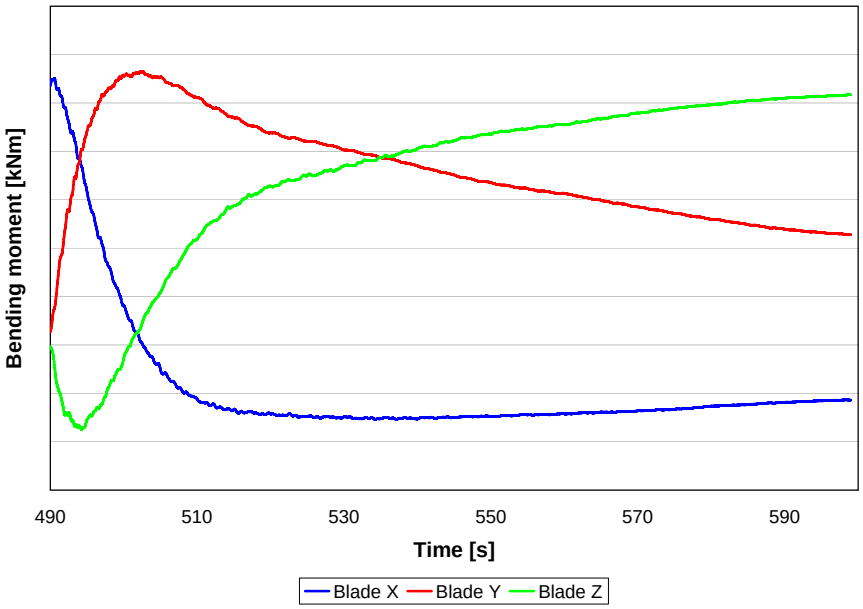

Figure 5.1 Blade root bending moments in flapwise direction, after shut down.

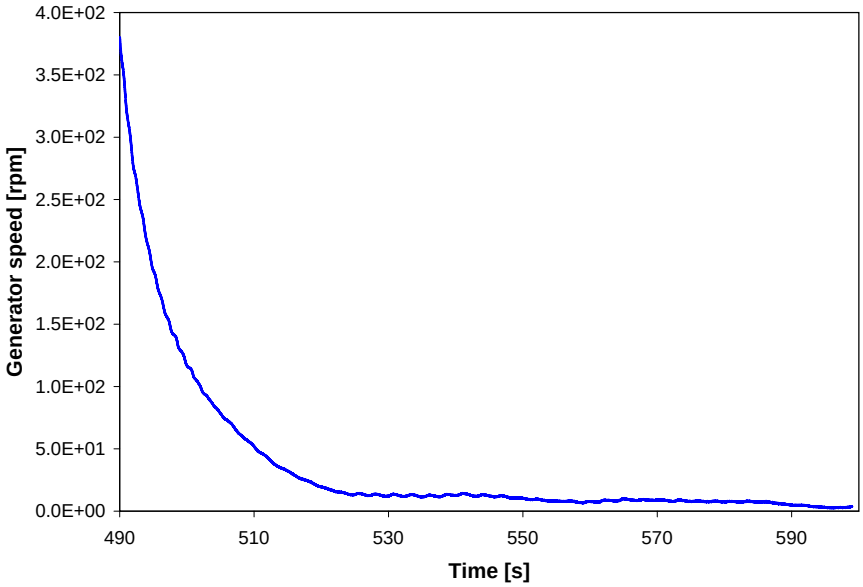

Figure 5.2 Generator speed after shut down.

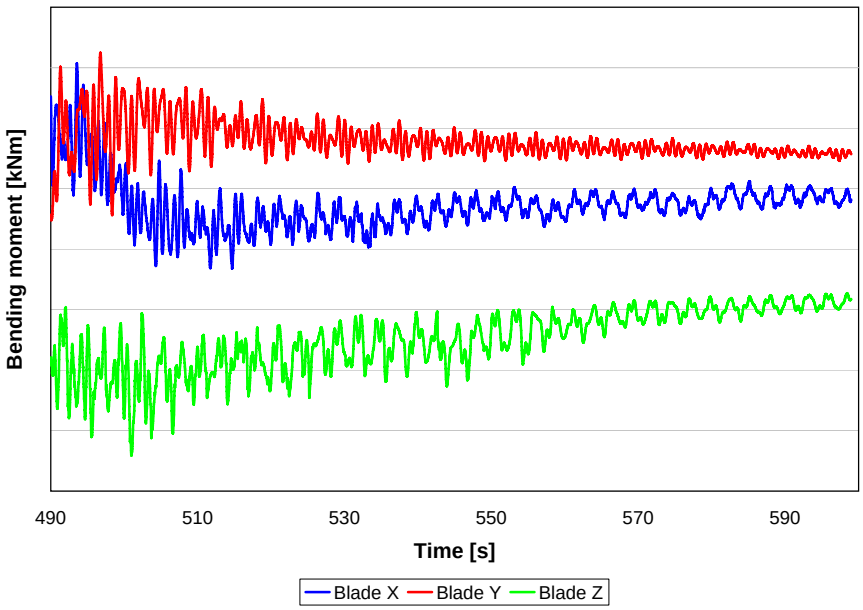

Figure 5.3 Blade root bending moments in edgewise direction, after shut down.

The generator speed gets approximately constant 40 s after the shut down, and this is also reflected on the bending moments in figure 5.1. At that time, the generator speed lowers down to approximately 12 rpm, which means a rotor speed of 0.1 rpm (the gearbox ratio is 117.65). Thereafter, the blade root bending moments are varying very smoothly.

Edgewise direction

The effect of the dead weight of the blades can also be observed on the edgewise bending moments, being mainly due to the tilt angle of the turbine. As the tilt angle is 5°, the contribution of the gravitational forces on the blades to the edgewise bending moments is much less important than in the flapwise case. This is reflected on the bending moments time series, where the sinusoidal shape at the beginning of the series is much less marked than in the flapwise case.

5.2.2 Turbine in operation

In order to identify the 2nd natural frequencies of the support structure and the blades, as well as for verification of the values obtained from the free vibration event, another case with the turbine in operation is studied. In particular, the period from 00:07 to 00:17, on 17/10/2004 is analyzed (10.12 m/s wind speed, 1.01 m significant wave height).

The first and second natural frequencies of the support structure and blades (again, normalized w.r.t. the design natural frequencies) obtained through this analysis are shown in table 5.4.

Table 5.4 Measured natural frequencies during operation, normalized w.r.t. the design natural frequencies.

	Blades		**Support structure**	
	Flapwise	**Edgewise**	**Fore-aft**	**Side-to-side**
$\mathbf{f}_0$	0.94	1.77	1.22	1.22
$\mathbf{f}_1$	2.72	5.43	7.32	7.32

The first natural frequencies of the support structure, both in fore-aft and side-to-side directions, have been constant in time since commissioning of the turbine (on 13/05/2004) to the end of the analyzed period (on 18/03/2005). To illustrate this, figure 5.4 shows the power spectral density for the *towbetilt* for three different 10-min periods. These three time histories correspond to the beginning, the middle and the end of the measuring campaign. The peaks corresponding to the first natural frequency of the support structure in fore-aft direction is observed for all three cases at the same frequency. Several conclusions can be derived from this fact:

1. The variation of the natural frequencies of the support structure, due to the different still water levels for the different periods analyzed, is negligible. This agrees with the expectations for the site, due to the mild weather conditions (maximum measured variations of 2.35 m on the SWL).

2. From the commissioning of the turbine until the end of the measurements period (10 months), scouring has had no influence in the natural frequency of the support structure. During the measurements period, the variation in the scour hole is estimated as 0.25 m, and therefore any further analysis on scour is skipped.

3. The variation of the soil conditions in the period analyzed is also negligible. Further investigations should be carried out in order to make accurate predictions on the long term.

5.2.3 Campbell diagram

In table 5.5, a summary of the natural frequencies obtained from the measurements analysis is shown.

Some strange values stand out from table 5.5. Both the natural frequencies of the blades in flap and edgewise directions decrease with increasing rotational speed. This is completely unreasonable, because due to the centrifugal stiffening effect, the natural frequencies of the blades should *increase* with increasing rotor speeds. As the natural frequencies of the blades obtained out of the shut down case match much better the design values, these have been used when building the Campbell diagram. This diagram, built for turbine 1, is illustrated in figure 5.5.

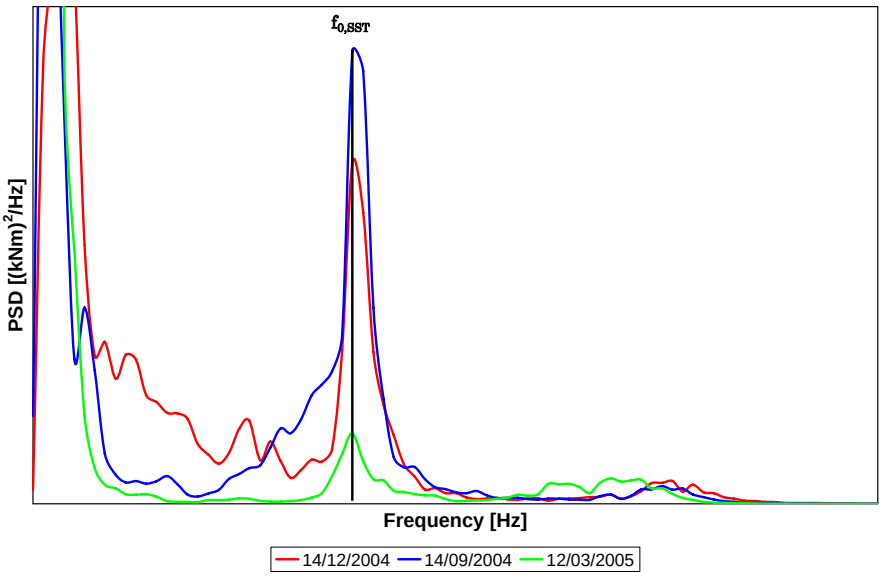

Figure 5.4 Variation of the natural frequency of the tower in fore-aft direction (*towbetilt*), during the measuring campaign.

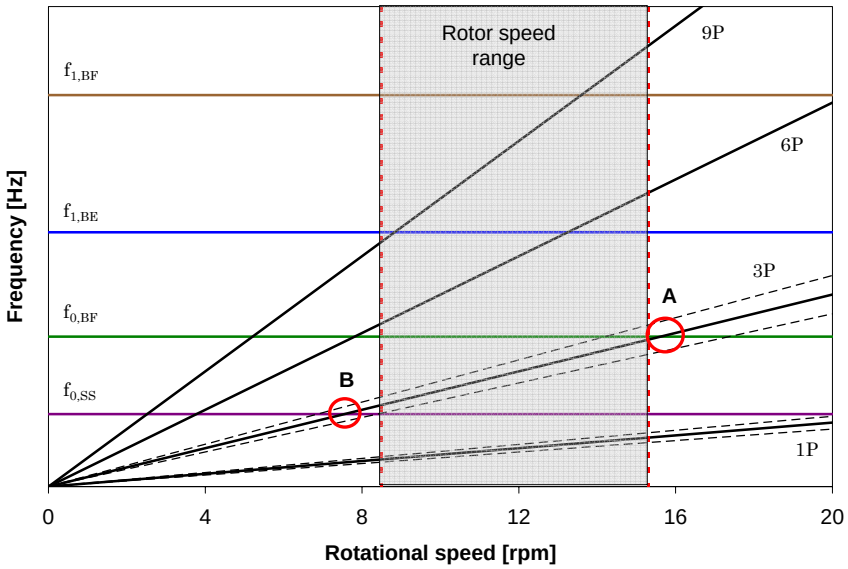

Figure 5.5 Campbell diagram for turbine 1.

Table 5.5 Summary of the natural frequencies obtained from measurements, normalized w.r.t. the design natural frequencies.

		Blades		**Support structure**	
		Flapwise	**Edgewise**	**Fore-aft**	**Side-to-side**
Measurements	f_0	1.04	1.79	1.22	1.22
(shut down)	f_1	—	—	—	—
Measurements	f_0	0.94	1.77	1.22	1.22
(in operation)	f_1	2.72	5.43	7.32	7.32

The rotor speed from the GE 3.6s turbine varies between 8.5 and 15.3 rpm. Therefore, this is the forbidden area for the excitational frequencies to coincide with any of the natural frequencies of the different subsystems. For both the 1P and the 3P excitations, a $\pm 10\%$ safety range is established. This means that not only the 1P and 3P lines themselves, but also the limits of these regions around 1P and 3P should not cross the natural frequency lines inside the forbidden area. However, as can be seen from the figure, the 3P excitation crosses the natural frequency of the blades in flapwise direction (point A) in the neighbourhood of the upper limit of the rotor speed region. Although it is strongly recommended not having such an excitation of a natural frequency so close to the rotor speed region, this specific case is not critical. The influence of the 3P excitation on the blades is not expected to be large, as its importance results from being a multiple of 1P, which is the main excitational frequency for the blades. In fact, measurements show that this influence is negligible (see figure 5.6). Five cases with rotational speed close to 14 rpm have been studied, and none of them shows an important excitation of the first eigenmode of the blades in flapwise direction by 3P. Therefore, the turbine can normally work within the normal range without being affected by the excitation of the first eigenmode of the blades in flapwise direction by 3P.

On the other hand, the excitation of the first eigenmode of the support structure by 3P (point B) occurs quite close to the lower limit of the rotor speed region. This could result in high loads on the support structure, reducing its expected lifetime. 3P is the most important excitation coming from the rotation of the machine on the support structure. However, as the soil conditions are expected to get softer in the long term [9], the first natural frequency of the support structure is also expected to become softer, making the cross between 3P and the natural frequency of the tower move away from the forbidden region.

5.2.4 Damping of the first fore-aft mode of the support structure

In order to estimate the damping of the first fore-aft mode of the support structure, the logarithmic decrement method has been applied, using the free decay

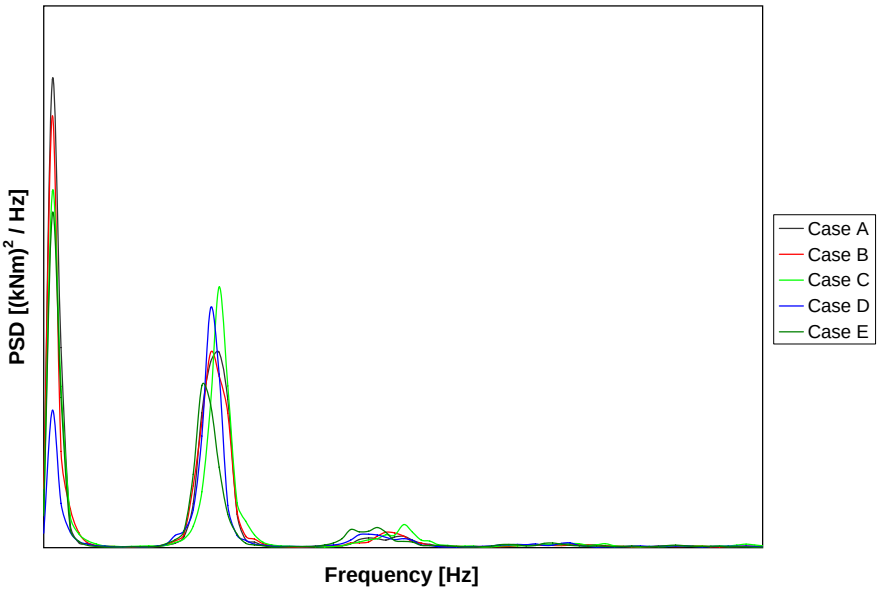

Figure 5.6 Power spectral density of the blade root bending moments in flapwise direction, turbine in operation, 14 rpm rotor speed.

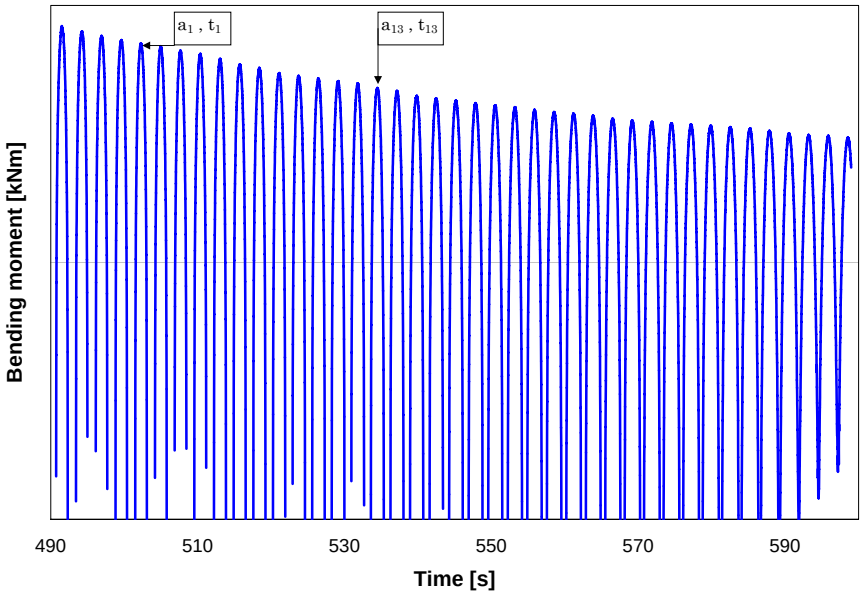

Figure 5.7 Tower bottom bending moment in fore-aft direction, after shut down.

history of the bending moment on the tower bottom after a turbine shut down. The value of the damping as a logarithmic decrement is given by:

$$\Lambda = \frac{1}{n-1} \cdot ln\left(\frac{a_1}{a_n}\right) \tag{5.1}$$

This logarithmic decrement is directly related to the damping ratio:

$$\xi = \frac{\Lambda}{2\pi} \tag{5.2}$$

In figure 5.7 the typical logarithmic response of the tower to a free vibration test can be seen. Results are shown in table 5.6. The value of 0.5% for the damping ratio is a typical material damping value for steel, which perfectly agrees with the studied structure.

Table 5.6 Damping ratio and logarithmic decrement.

Λ [-]	ξ [%]
0.0324	0.52

5.3 Modal analysis

A summary of the natural frequencies obtained from the modal analysis is shown in table 5.7. The values of the natural frequencies are calculated by the simulation software FLEX5.

Table 5.7 Summary of the natural frequencies obtained from the modal analysis, normalized w.r.t. the design natural frequencies.

	Blades		**Support structure**	
	Flapwise	**Edgewise**	**Fore-aft**	**Side-to-side**
f_0	1.06	1.71	1.22	1.23
f_1	2.67	5.23	7.51	7.36

5.4 Conclusions

In order to extract some conclusions from the analysis of the natural frequencies, table 5.8 shows a summary of the eigenfrequencies obtained from measurements, modal analysis and design.

Table 5.8 Comparison of the natural frequencies obtained from measurements, modal analysis and design, normalized w.r.t. the design natural frequencies.

		Blades		**Support structure**	
		Flapwise	**Edgewise**	**Fore-aft**	**Side-to-side**
Measurements	f_0	1.04	1.79	1.22	1.22
	f_1	2.72	5.43	7.32	7.32
Modal	f_0	1.06	1.71	1.22	1.23
analysis	f_1	2.72	5.43	7.32	7.32
Design	f_0	1.00	1.66	1.00	1.00
	f_1	2.82	5.24	5.71	5.71

The main outcome of the analysis of natural frequencies can be summarized in two statements:

1) In general, for the blades, the natural frequencies from design and modal analysis are matching quite well with the measured ones. However, some uncertainties are involved in the determination of the measured value of the $f_{0,BF}$, as the values from the case in operation are significantly lower than those obtained from the idling case. Finally, the closest value to the $f_{0,BF}$ calculated in design (i.e. the value obtained in idling conditions) has been assumed as true, though no explanation for the mismatching between the idling case and the case in operation has been found.

2) For the support structure, the main mismatching values are related to the first natural frequency in both fore-aft and side-to-side directions calculated in design. These natural frequencies calculated in design are underestimated to a 15% (with reference to the measured ones). Nevertheless, the modal analysis in the design phase has provided a safer approach. In this analysis, the behaviour of the support structure for different cases with different natural frequencies is checked. According to the modal analysis, both the first and second measured natural frequencies of the support structure lay within the range calculated during the design phase. Therefore, the design has been robust enough to ensure the good behaviour of the support structure under current conditions.

Chapter 6

Turbine model in FLEX5

Extensive simulations of the behaviour of the turbine under different environmental conditions were performed during the design phase of the Arklow Bank Offshore Wind Farm. For this purpose, the simulation package FLEX5 was used. The design model of the GE 3.6s offshore wind turbine used in the design process has been provided by GE Wind Energy. The information obtained during the measurement campaign, together with design basis and certification documents, has been used for refinement of the turbine model, regarding both structural properties and environmental conditions.

6.1 Simulation code and modelling

The simulation package FLEX5 was used during the design phase, as mentioned in the previous paragraph, and also for the verification of design assumptions. FLEX5 was developed at the Fluid Mechanics Department of the Technical University of Denmark. This software can be used to model onshore and offshore horizontal axis wind turbines with 1 to 3 rotor blades, fixed or variable speed, pitch or stalled controlled. FLEX5 simulates dynamic responses of wind turbines under different operation conditions, including operation in turbulent wind and transient load situations. The aeroelastic model uses a modal analysis with a relatively limited number of degrees of freedom to describe rigid body motions and elastic deformations in the time domain.

Within FLEX5 the whole wind turbine is modelled with 28 non-linearly coupled degrees of freedom. Calculations may be linear or non-linear. Table 6.1 shows the breakdown of the whole structure in coupled components and the corresponding degrees of freedom.

Results of the simulations consist of time histories for loads and deformations which can be used to design single components for extreme loads or calculating fatigue damage within their lifetime. Stochastic time series of wind and wave kinematics were calculated by Vindsim and Wavekin (respectively), two extensions for the pre-processing environment of FLEX5.

Table 6.1 Degrees of freedom in FLEX5 [10].

Component	Degrees of freedom (DOF)	Number of DOF
Foundation		
	Translation in 3 directions	3
	Rotation around 3 axes	3
Tower		
	1st eigenmode in 2 directions	2
	2nd eigenmode in 2 directions	2
	Torsion	1
Nacelle		
	Nacelle tilt	1
Blades		
	1st eigenmode, edgewise	3
	2nd eigenmode, edgewise	3
	1st eigenmode, flapwise	3
	2nd eigenmode, flapwise	3
Power train		
	Rotation	1
	Torsion	1
	Bending in 2 directions	2
Total		**28**

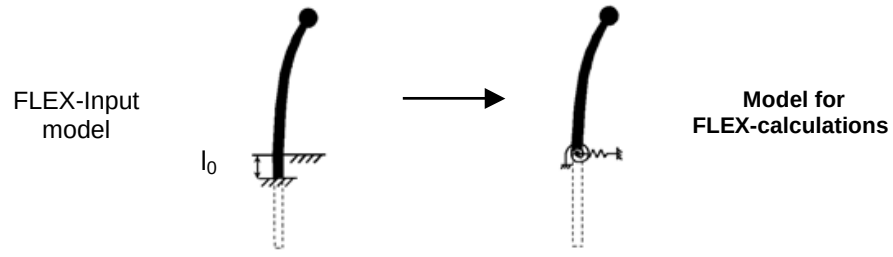

Figure 6.1 Derivation of the foundation stiffness matrix from the beam model with clamped edge [8].

Monopile foundation

In FLEX5 the monopile foundation is modelled by a stiffness matrix representing a pair of coupled translational and rotational springs. The user is requested to set the so-called *apparent fixity length* l_0, i.e. the distance below mudline at wich the foundation is assumed to be rigidly clamped (see figure 6.1).

The *apparent fixity length* can be set to make the 1st natural frequency of both the FLEX5 model and the real structure be coincident. The stiffness matrix, which is related to the mudline level, is derived from the *apparent fixity length* concept according to the theory of elasticity, and used in further FLEX5 calculations. One of the big disadvantages of this calculation method is its inability to calculate loads on the support structure below seabed.

The stiffness matrix model of the foundation can be expressed as:

$$\begin{pmatrix} k_{11} & k_{12} \\ k_{21} & k_{22} \end{pmatrix} \cdot \begin{pmatrix} \delta \\ \theta \end{pmatrix} = \begin{pmatrix} F \\ M \end{pmatrix} \tag{6.1}$$

where

k_{11}	stiffness against displacement due to the horizontal force at seabed
k_{12}	stiffness against displacement due to the moment at seabed
k_{21}	stiffness against torsion due to the horizontal force at seabed
k_{22}	stiffness against torsion due to the moment at seabed
δ	displacement at seabed
θ	torsion at seabed
F	horizontal force at seabed
M	moment at seabed

6.2 Tuning of the simulation model for load validation

FLEX5 simulations for the present thesis have been run at the SWE (Stiftungslehrstuhl Windenergie) of the Universität Stuttgart. The model of the turbine (provided by GE Wind Energy) has been therefore adapted from the FLEX5 version of GE Wind Energy to the version of the SWE. For the validation of the SWE model, the design load time series have been provided by GE Energy. Nevertheless, only the main parameters of the corresponding wind and wave fields were available, and not the files themselves. Hence, slight changes on the output time series, and even in the fatigue damage equivalent loads (with differences up to 25%, as shown in section 7.3.3.2), can be related to different wind and wave fields. Therefore, the validation of the SWE model relies on similar average and standard deviation values, rather than on similar fatigue damage equivalent loads.

The adapted model is further refined for load validation purposes. Small modifications on the turbine geometry carried out on the last stages of the design have not been reflected on the turbine simulation model. In addition, the actual support structure natural frequencies are not accurately estimated

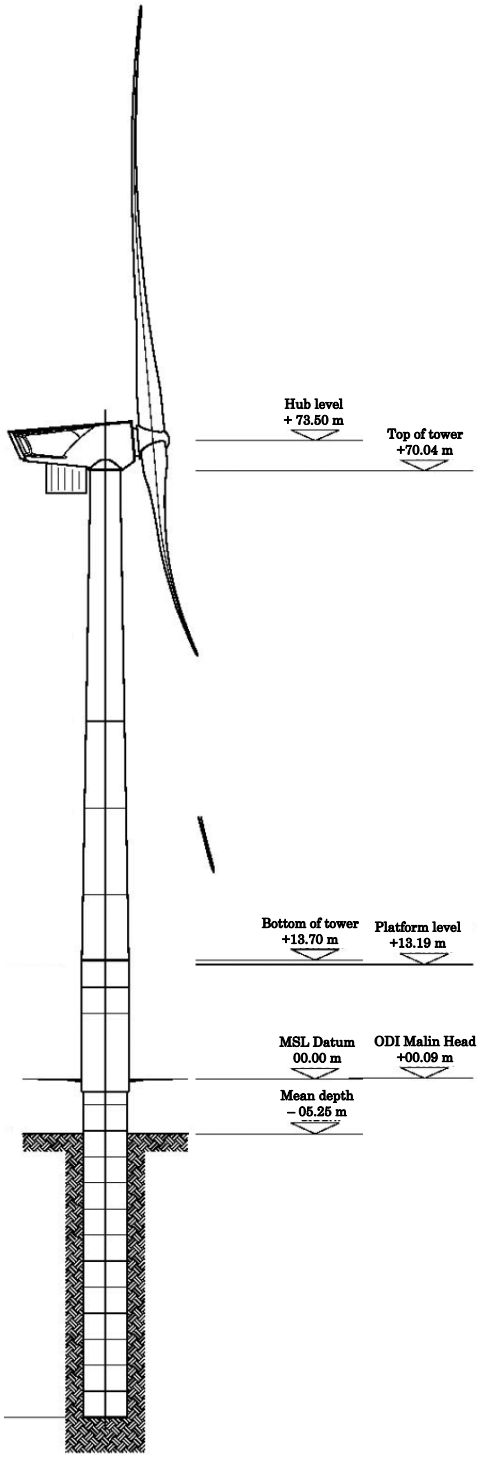

Figure 6.2 Tower and monopile arrangement of turbine 1.

by the design model. Finally, some of the assumptions made in the design phase regarding environmental conditions have not been verified in chapter 4. Hence, some model tuning is necessary to correct these slight deviations, in order to better reproduce the behaviour of the turbine.

The adapted model is first modified to meet the definite geometry of the real structure (see figure 6.2), according to the certification document of the foundation [6], which is assumed to be the definite one. However, small differences with reality could arise, as several slightly different geometries are identified in other documents provided by GE Energy, including the original FLEX5 model. On a second step, the model is tuned in order to achieve coinciding modal properties (1^{st} and 2^{nd} natural frequencies) between the real support structure and the FLEX5 model. This is done through a trial an error process, by adjusting the apparent fixity length, as well as the monopile diameter and thickness below seabed level, until the sought values of the natural frequencies are obtained.

The blade model is not modified, as the simulated natural frequencies of the blades are matching the measured ones quite accurately (see section 5.4). On the other hand, due to the poor modelling of the bending modes of the drive train in FLEX5, this is assumed to have an infinite bending stiffness. Therefore, no drive train natural modes and frequencies are obtained from simulations, and subsequently no further tuning of the drive train model is carried out.

Only the most relevant input files (monopile and tower) of both the FLEX5 original (design) model and the tuned model of the GE 3.6s turbine at Arklow Bank are shown in this section. The rest of the files have only been adapted from the FLEX5 version from GE Energy to the version of the SWE.

6.2.1 Monopile model

The first tuning of the monopile model is referred to the water depth, changed from 9.30 m in the original model (see section 4.2.1) to 5.25 m in the tuned model. The length of the monopile is changed subsequently, based on the information in the certification document of the support structure [6]. The top of the monopile is changed from 15.15 m above seabed to 11.30 m. The length of the transition piece has also been changed according to [6], from 13.95 m to 15.14 m.

The wall thickness of the structure has been also tuned. The 38 mm wall thickness used in the original model for the transition piece - monopile overlapping region is replaced by the sum of their individual wall thicknesses (the thickness of the grouted joint is not considered), that is, 95 mm. In the region above the top of the monopile, the thickness of the transition piece is constant (according to [6]), whilst in the original model it decreases with increasing height.

Based on the results from section 5.2.4, the logarithmic decrement of the structural damping is changed from 0.010 to 0.032.

There are also some changes regarding the lumped masses attached to the monopile and transition piece. Three lumped masses of 7,400 kg, directly attached to the monopile, are included in the original monopile file. However, these masses cannot be associated to any auxilliary structure, and therefore are

neglected in the tuned version. Furthermore, the mass of the grouted joint has been recalculated, and used in the tuned version of the model (four lumped masses of 10,000 kg each, instead of the original 50,405 kg of total mass of the grouted joint). The mass of the platform (43,005 kg) remains equal.

The last tuning of the monopile model refers to the *apparent fixity length* and the thickness and diameter of the monopile below mudline. These parameters are changed in order to match the modal properties of the model with those determined from measurements.

6.2.2 Tower model

6.2.2.1 Tuned model

Some small changes are made on the tower input file. The input-output flag is removed, together with the torsional stiffness of the tower and the nacelle tilt stiffness (which are not taken into account for the analysis).

The logarithmic decrement of the structural damping is modified for the 1st and 2nd modes, fore-aft and side-to-side directions. The structural damping of the tower is related to the structural damping of the coupled tower-monopile system by means of the following expresion [11]:

$$\Lambda_{tower} = \frac{\Lambda \cdot f_{rigid}}{f_{coupled}} \tag{6.2}$$

where

Λ	logarithmic decrement of the structural damping of the support structure (introduced in the monopile input file)
Λ_{tower}	logarithmic decrement of the structural damping of the tower (introduced in the tower input file)
$f_{coupled}$	natural frequency of the support structure
f_{rigid}	natural frequency of the support structure, assuming an infinitely stiff foundation

From section 5.2.4 the structural damping of the support structure is known, as well as its natural frequency. The f_{rigid} is derived from a simulation in FLEX5, by deactivating the degrees of freedom of the foundation, making it completely stiff. The logarithmic decrement of the tower structural damping resulting from equation 6.2 is 0.043. This is the value used for the 1st eigenmode, both fore-aft and side-to-side directions. Normally, a good estimate for the structural damping of the 2nd eigenmode is given by doubling the damping of the 1st mode, thus obtaining a value of 0.086.

6.3 Conclusions

The GE3.6s model has been tuned for matching the real geometry of turbine 1 at the Arklow Bank Offshore Wind Farm. Some changes on the geometry of

the transition piece during the latest steps of the design process could not be reflected in the model, probably because the simulations have been run before the last changes were made. Changes on the length of the monopile are derived from the overestimation of the site water depth. Actually, the real length of the monopile is not changed, but only its length in the model. This is due to the *apparent fixity length* concept, which implies a fictive length of the monopile below mudline level.

Finally, the model is tuned for matching the measured modal properties (natural frequencies of the different subsystems, and structural damping). Regarding the tuning of the *apparent fixity length*, the difference between this fictive length (26.50 m), and the real one (33.70 m), is to be highlighted. Anyway, this fixity length is very sensible to changes in the diameter and thickness of the monopile under mudline level (also tuned in this case to fictive values).

After this tuning process, the model is well prepared to accurately simulate the dynamic behaviour of the turbine.

Chapter 7

Fatigue analysis

7.1 Introduction

The fatigue analysis is based on short term (10 min) load calculations, which are compared with design results and measured values. The measurement campaign on turbine 1 has been too short for obtaining representative information of the environmental conditions at Arklow Bank along a whole year. A long term fatigue analysis based on those measurements would not be reliable, and therefore only a short term fatigue analysis is performed. Seventeen 10-min time series are chosen from the whole measurements period for an in-depth analysis. These time histories are selected in such way that they match as much as possible design conditions (especially regarding mean wind speed and significant wave height), in order to enable later comparisons between design results, measurements and simulations.

Due to mismatching results between simulations and measurements, further investigations on the influence of several parameters on the fatigue damage equivalent loads are carried out. Results of these investigations lead to some hypothesis on the reasons behind the differences between simulations and measurements.

Due to confidentiality issues, all figures involving equivalent loads in this chapter are normalized, referring all the values of the y-axis to the maximum in each graph. Load spectra are not normalized, however numerical data are removed from their axis.

7.2 Fatigue load cases selection

7.2.1 General approach

During the design process of a wind farm, several fatigue load cases under certain environmental conditions are studied, in order to ensure that the wind turbine will endure the fatigue load over lifetime. However, the overall real environmental conditions are often less severe than what is assumed in the design.

This complicates the task of finding long measurement periods with the same environmental conditions as used in design load cases. As these measurements periods are usually not long enough to ensure statistical reliability, the load verification process often aims at the validation of the aeroelastic model. This is done by applying the measured environmental conditions as an input for the simulations, and comparing the output with measurements.

In the offshore environment, there are two main load drivers:

- Wind, defined by two main parameters: mean wind speed and turbulence intensity.
- Waves, defined by another two main parameters: significant wave height and zero up-crossing period.

Turbulence intensity quantification might be distorted by trends in the wind speed [12]. A trend is a monotonic increase, decrease, or a long cyclic variation of the 1-min wind speed averages. The use of time series with a trend in the wind speed is not recommended, and should be avoided, where possible. Alternatively, there are de-trending algorithms that could be applied in order to avoid overestimation of the turbulence intensity.

In the case of the wave height, the possibility of trends should also be taken into account. However, the change in the parameters related to the variation of the water level is much slower than those accounting for the wind variations. The stationary period of the wind varies from 10 minutes to 1 hour (spectral gap in figure 7.1a), whilst a sea state is commonly regarded as stationary within a period from 1 to 3 hours (deep valley in the *long period waves* region in figure 7.1b). If the analysis focuses in 10-min periods, trends in the water level variations are assumed to be negligible.

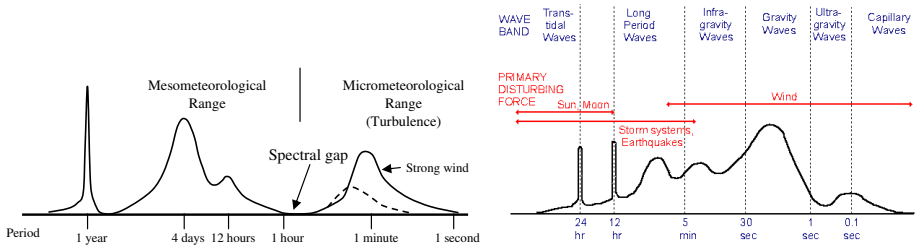

Figure 7.1 Qualitative energy spectra for (a) wind [13]; (b) ocean waves.

In conclusion, the four aforementioned parameters should guide the selection process for load validation. The objective is the identification of measurement time histories with similar values for those four parameters as used in design. Trends in both wind speed and wave height should be carefully assessed, and avoided where possible.

Table 7.1 Design load cases for fatigue analysis [2].

No.	H_s [m]	T_z [s]	$\bar{U}$ [m/s]	I [%]
1	0.14	4.51	4	19.24
2	0.23	4.67	5	18.40
3	0.34	4.85	6	17.98
4	0.48	5.06	7	17.79
5	0.63	5.28	8	17.74
6	0.81	5.51	9	17.67
7	1.02	5.74	10	17.48
8	1.24	5.96	11	16.99
9	1.49	6.17	12	16.46
10	1.76	6.36	13	15.63
11	2.06	6.52	14	14.76
12	2.38	6.66	15	14.02
13	2.72	6.78	16	13.42
14	3.08	6.87	17	12.93
15	3.47	6.96	18	12.53
16	3.87	7.05	19	12.22
17	4.31	7.17	20	11.95
18	4.76	7.34	21	11.73
19	5.24	7.60	22	11.53
20	5.74	7.99	23	11.38
21	6.26	8.57	24	11.24
22	6.81	9.00	25	11.12
23	6.81	9.00	>25	11.02

7.2.2 Selection process

On a first step, the selection process of the time series for fatigue analysis is based on two parameters: mean wind speed and significant wave height. These parameters should have similar values to those used on the design fatigue load cases (see table 7.1). On a second step, from all the time series identified in the measurements period that comply with the previous condition, those having mean loads and standard deviations in the same order of magnitude as design mean loads and standard deviations are chosen.

Both the turbulence intensity and the zero up-crossing period should also be taken into account on the first selection step, as stated in the previous section. However, when looking into the measurements period, no cases with similar values of the I or the T_z to those in table 7.1 are found. Therefore, these parameters are neglected for the selection process.

On the first selection step, 10-min measurement periods with similar $\bar{U}$ and H_s to design cases have been identified in the wind speed range 5 - 14 m/s. For wind speeds outside this range, no 10-min time series matching the design cases are found in the measurements. Therefore, the short term fatigue analysis is

Table 7.2 Load cases for the verification of the fatigue analysis.

No.	H_s [m]	T_z [s]	$\bar{U}$ [m/s]	I [%]
1	0.35	2.57	6.07	7.90
2	0.33	2.40	6.24	8.30
3	0.48	2.79	6.96	4.86
4	0.48	2.74	6.98	8.74
5	0.62	3.08	7.86	7.80
6	0.62	3.66	7.77	5.34
7	0.77	3.58	8.81	6.42
8	0.84	4.00	8.77	7.21
9	1.05	4.34	9.93	4.88
10	1.06	4.30	9.90	3.74
11	1.22	4.12	10.96	8.06
12	1.27	4.20	10.87	6.68
13	1.51	5.20	11.78	7.11
14	1.50	4.83	12.21	8.65
15	1.70	5.20	12.83	7.95
16	1.70	5.20	12.84	5.74
17	2.08	5.81	14.06	9.71

constrained to the partial load range, up to rated wind speed. Moreover, only two eligible periods are found in the measurements for the 5 m/s wind speed, both of them happening with the turbine in idling conditions. These time series are finally discarded, as no conclusions could be extracted from comparisons with design load case number 2 (which assumes turbine in operation). No period with trend in the wind speed is chosen. Trends in the wave height are negligible for 10-min time series, as stated in the previous section.

The second step of the selection process leads to a final group of 17 data sets (two data sets per each wind speed in the 5 - 14 m/s range, except for 14 m/s, with only one) shown in table 7.2.

7.3 Short term fatigue analysis of verification load cases

7.3.1 General approach

Next step in the process is the simulation of the behaviour of the turbines under the measured environmental conditions for the chosen time series. For comparison purposes, the simulations are run both with the original GE Wind Energy model and the tuned one.

Fatigue damage equivalent load calculations are performed by a post-processing tool from FLEX5. The values used for the inverse slope of the S-N curve m are

3 for the support structure and 12 for the blades. Six sensors are analyzed for each of the selected time histories:

- Support structure
  - Tower bottom bending moment in fore-aft direction (*towbetilt*)
  - Tower bottom bending moment in side-to-side direction (*towberoll*)
  - Monopile bending moment in fore-aft direction, at mudline level (*monbetilt*)
  - Monopile bending moment in side-to-side direction, at mudline level (*monberoll*)
- Blades
  - Blade root bending moment in flapwise direction (*blbef*)
  - Blade root bending moment in edgewise direction (*blbee*)

The analysis mainly focuses on both the tower and monopile bending moments in fore-aft direction. Two reasons justify this choice:

1. **Both parameters are focused on the response of the support structure**. The special conditions of the wind farm, located in an offshore environment, affect to a higher extent the behaviour of the support structure, compared to the blades. The influence of the hydrodynamic loads in the response of the blades is negligible, whilst the support structure is significantly influenced by the presence of waves.
2. **On the support structure, these two loads are the most indicative of both the environmental and operational conditions of the turbine**. Both the tower and monopile bending moments are mainly induced by the thrust caused by the wind on the rotor. For shallow water depths (as in this case) the thrust force is the main load on the turbine. Furthermore, they are also an indication of the operational conditions of the turbine, as the thrust force is directly related to the amount of energy extracted from the wind. Big differences between simulation results and measurements in these magnitudes would imply different environmental or operational conditions. In contrast to the fore-aft bending moments, the side-to-side bending moments do not have such a strong dependency on the thrust force, but on the variations of both wind and wave directions.
3. **These two loads represent the main contribution to fatigue damage**, which is actually the object of study.

7.3.2 Simulation of verification load cases in FLEX5

Simulations have been run with both the GE Wind Energy design and the (SWE) tuned models, as mentioned in the previous section. In order to strictly assess the difference in performance of both models, identical simulation conditions are used, including the same wind and wave fields. A Kaimal model (from IEC 61400 ed. 3 [14]) is used for generating the stochastic wind field, whilst the

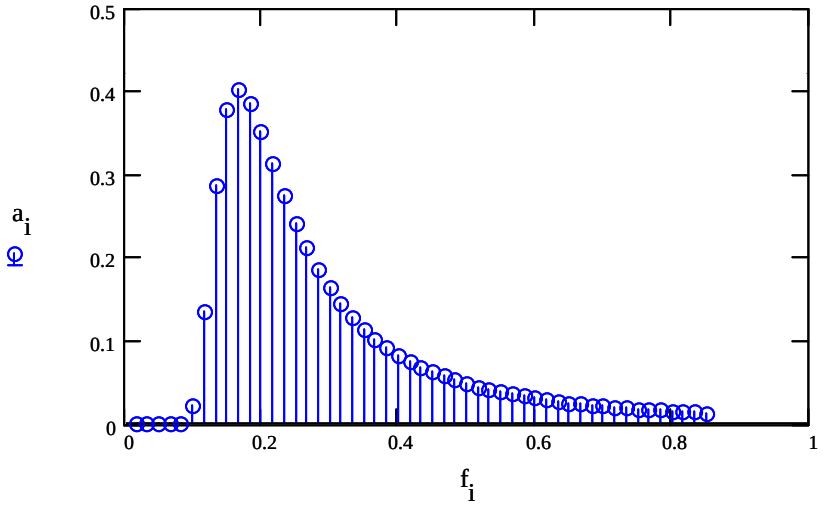

Figure 7.2 Discretization of the wave spectrum [15].

wave field generation is based on the discretization of the PSD of the measured wave heights (see figure 7.2).

The input to the program Wavekin (the wave field generation tool from FLEX5) consists of the amplitude and phase for 200 frequency components in the range 0 – 1 Hz. Each discrete component represents a harmonic wave on the form [15]:

$$\eta_i = a_i \cdot \sin\left(\omega_i \cdot t - k_i \cdot x + \theta_i\right) \tag{7.1}$$

where

$$a_i = \sqrt{2 \cdot S\left(f_i\right) \cdot \Delta f} \tag{7.2}$$

$$\omega_i = 2\pi \cdot f_i \tag{7.3}$$

$$k_i = \frac{2\pi}{L_i} \tag{7.4}$$

being

η_i	elevation of the *i-th* harmonic wave at the point x at a time t
a_i	amplitude of the *i-th* harmonic wave
ω_i	angular velocity of the *i-th* harmonic wave
k_i	wavenumber
θ_i	random phase of the *i-th* harmonic wave
$S(f_i)$	spectral density of the *i-th* discrete component of the wave field spectrum

Δf	frequency intervals width (constant)
f_i	discrete *i-th* frequency component
L_i	wave length of the *i-th* harmonic wave, calculated on the basis of the wave period T_i and the water depth

As measurements provide no information on some aspects, some assumptions are required for the simulations:

1. No yawed inflow is considered
2. No wind and waves misalignment is considered
3. No currents are considered
4. The density of the air is assumed to be constant and equal to 1.255 kg/m^3, and its dynamic viscosity to $1.82 \cdot 10^{-5}$ kg/(m·s)
5. Stall, dynamic wake, tower shadow and tower drag effects are taken into account

7.3.3 Validation of the tuned model results

Fatigue damage caused by different load histories are compared through the fatigue damage equivalent load. For the present thesis, all the fatigue damage equivalent loads are calculated for a reference number of cycles of 600. All figures in this chapter (and also in chapter 8) are normalized, relating all the values on the y-axis to the maximum of each graph.

Figures 7.3, 7.4, 7.5 and 7.6 show the comparison between fatigue damage equivalent loads calculated from measurements and simulation results, for the tower and monopile, in fore-aft and side-to-side directions. Figures 7.7 and 7.8 show the comparison between the equivalent loads calculated from measurements and simulations results for the blade root bending moments, in flapwise and edgewise directions. Simulation results shown in the figures correspond only to the tuned model. Differences between the design model and the tuned model are analyzed in section 7.3.4.

When looking into the fore-aft direction (figures 7.3 and 7.5) large variations in the differences between measurements and simulations are observed. In some cases the simulations are almost perfectly matching the measurements (cases 1, 3, 9, 13 and 16); however, in some others the differences are considerably large (cases 5, 10 and 17). For the side-to-side direction the mismatching between measurements and simulations is much more notorious than in fore-aft direction. In the case of the blades, large differences between measurements and simulations mainly arise in the flapwise direction. Gravity forces are dominant in the edgewise direction, and therefore the matching between simulations and measurements is almost perfect.

However, for the reasons explained in section 7.3.1, further investigations are mainly focused in obtaining better results for the support structure fore-aft bending moments. Several aspects are studied in order to find the reasons for the large differences observed:

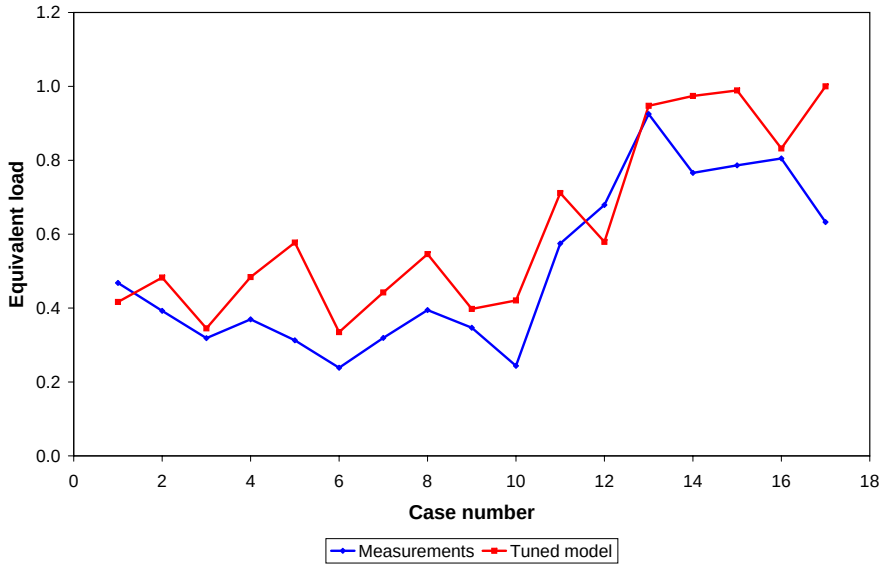

Figure 7.3 Fatigue damage equivalent loads of the *towbetilt*, for verification load cases.

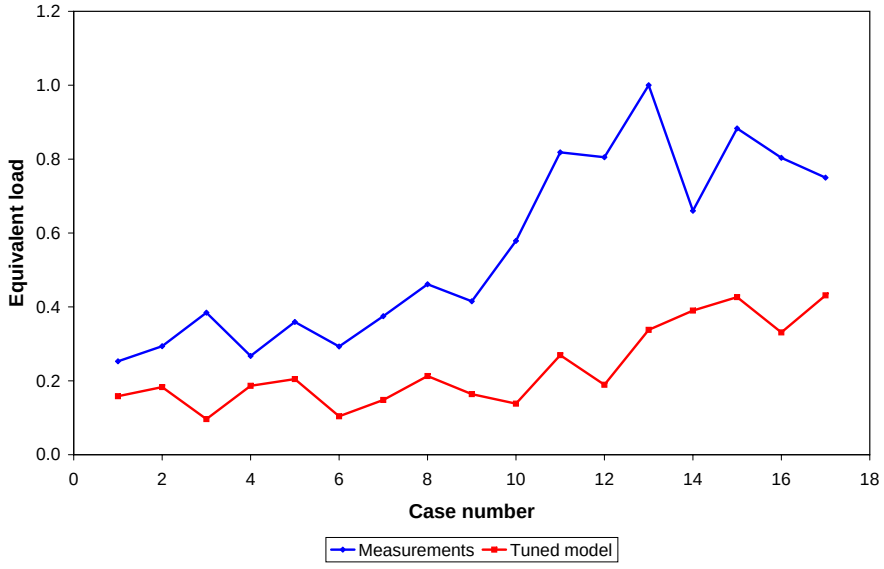

Figure 7.4 Fatigue damage equivalent loads of the *towberoll*, for verification load cases.

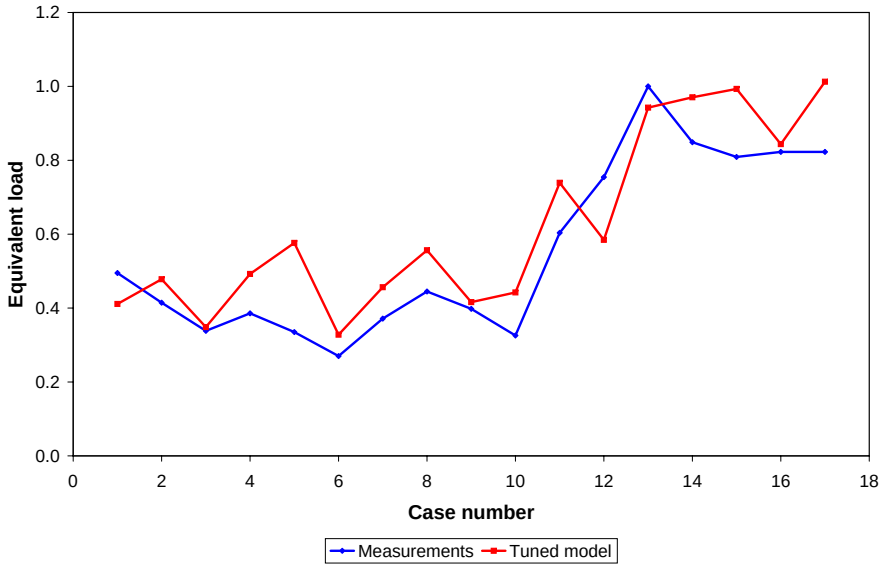

Figure 7.5 Fatigue damage equivalent loads of the *monbetilt* for verification load cases.

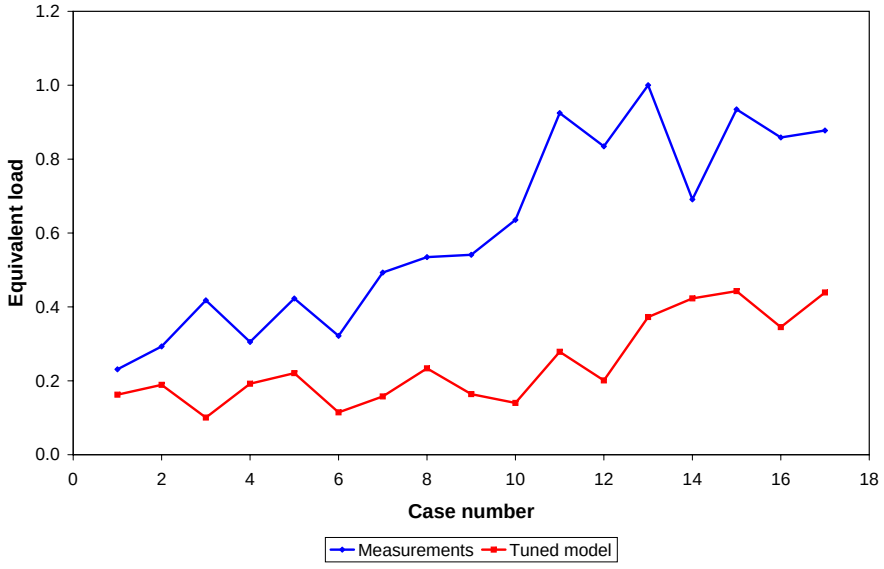

Figure 7.6 Fatigue damage equivalent loads of the *monberoll* for verification load cases.

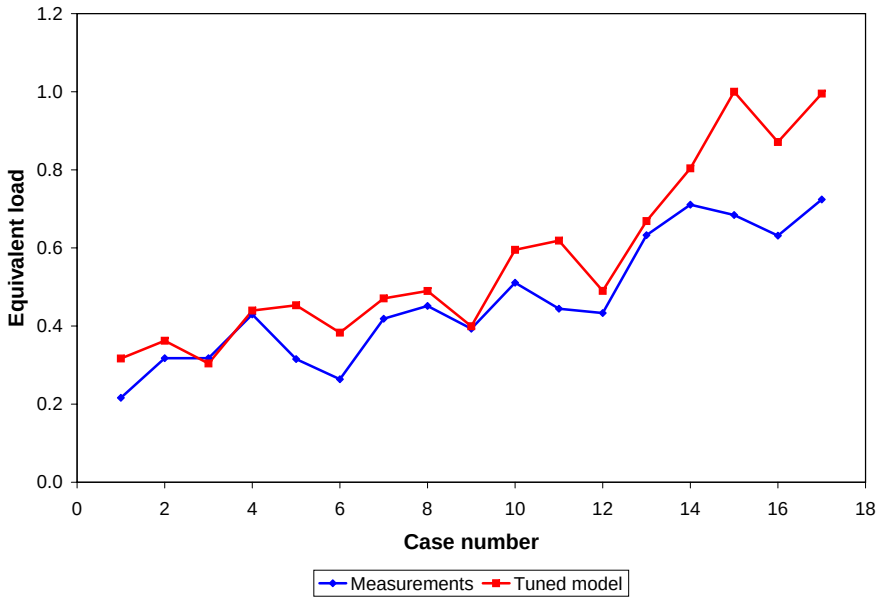

Figure 7.7 Fatigue damage equivalent loads of the *blbef* for verification load cases.

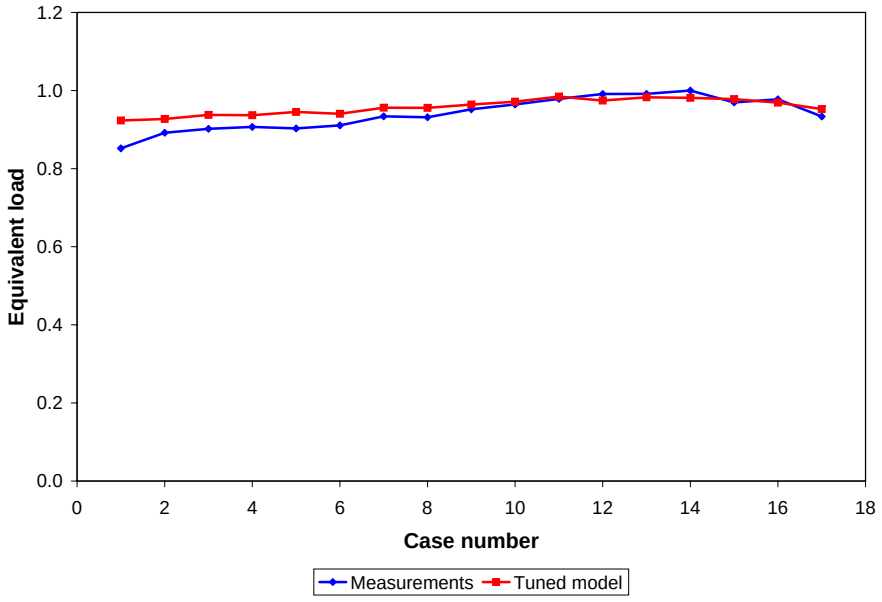

Figure 7.8 Fatigue damage equivalent loads of the *blbee* for verification load cases.

- Aspects related to load simulation
    1. Influence of a possible mismatching of the simulation model to the design thrust curve
    2. Influence of hydrodynamic loads
    3. Influence of structural dynamics
    4. Influence of an incorrect simulation of the dynamic behaviour of the support structure
- Aspects related to wind field generation
    5. Influence of the variation of random seeds for wind field generation
    6. Influence of coherence and length scale
- Aspects related to measurements and operational conditions
    7. Influence of yaw misalignment
    8. Influence of wind and waves misalignment
    9. Influence of the distance between the turbine and the anemometer

7.3.3.1 Aspects related to load simulation

Matching of simulation model to design thrust curve

The first investigation focuses on the verification of the tuned simulation model regarding thrust forces. Eight out of the seventeen verification load cases are chosen for this purpose. The verification is carried out by comparing the design thrust coefficient curve values (see figure C.1 in Appendix C) and the simulation results. As explained in the Appendix, the design thrust coefficient curve is calculated for certain specific conditions, which need to be used in the simulation model in order to obtain comparable results. Thus, the turbulence intensity is calculated according to IEC 61400 ed. 3 [14]:

$$I = \frac{I_{ref} \cdot \left(0.75 \cdot \bar{U}_{hub} + 5.6\right)}{\bar{U}_{hub}} \tag{7.5}$$

where

I	actual turbulence intensity
I_{ref}	reference turbulence intensity (12.50%, in this case)
$\bar{U}_{hub}$	mean wind speed at hub height

In addition, as the design thrust coefficient curve is determined in stiff conditions (i.e. only the rotational motion of the turbine is allowed), all the simulation results presented in this section correspond to stiff conditions.

Figure 7.9 shows the comparison between the results obtained from simulations, and the values taken from the thrust coefficient curve, for eight different wind speeds. The C_T calculated in the simulations represents the mean value for each 10-min period.

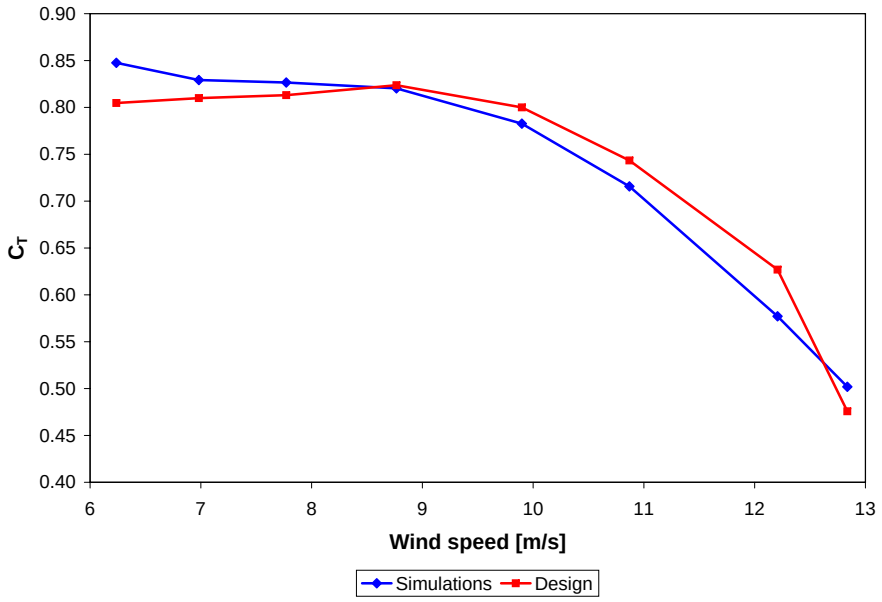

Figure 7.9 Thrust coefficient comparison between design and simulation results.

According to the results shown in figure 7.9, a mismatching of the thrust values provided by the tuned model is discarded. The simulation and design curves are very close to each other, with a maximum difference of 7.95% for a wind speed of 12.21 m/s (load case number 14). In conclusion, the tuned model is validated for thrust force calculations with respect to design values. Therefore, the mismatching between the equivalent loads obtained from measurements and from simulations does not have its origin on an erroneous calculation of thrust forces.

Influence of hydrodynamic loads on fatigue damage

In this section, the influence of hydrodynamic loads on fatigue damage equivalent loads is analyzed. In order to assess the relative importance of hydrodynamic effects, new simulations are run for the 17 studied load cases. Water density is set to 0 kg/m^3, in order to eliminate the effect of the waves, but also the hydrodynamic damping of the structure. The rest of the parameters of the simulation remain identical to those used in the first set of simulations.

In figures 7.10 and 7.11 the equivalent loads for simulations with and without hydrodynamic effects are plotted, for both the tower and monopile in fore-aft direction. From the figures it can be concluded that the hydrodynamics cannot assumed to be always negligible, as the differences between the results from both simulations reach 47.5% in the case of the *towbetilt*, and 44.8% in the case of the *monbetilt*. Nevertheless, the large variability of this influence, being negligible in some of the studied cases (cases number 1, 11, 12 and 13), should be pointed out.

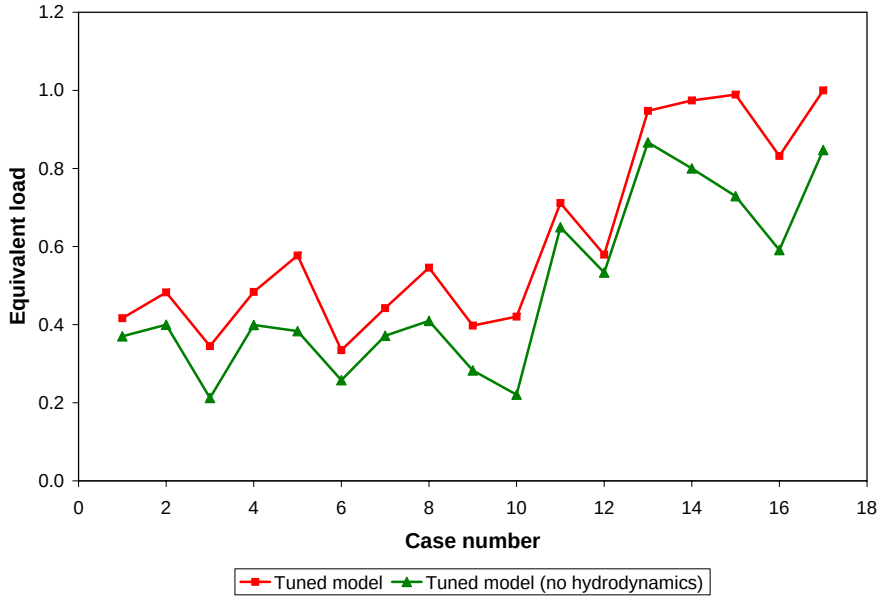

Figure 7.10 Comparison of the *towbetilt* fatigue damage equivalent loads for the normal case, and for a water density of 0 kg/m^3.

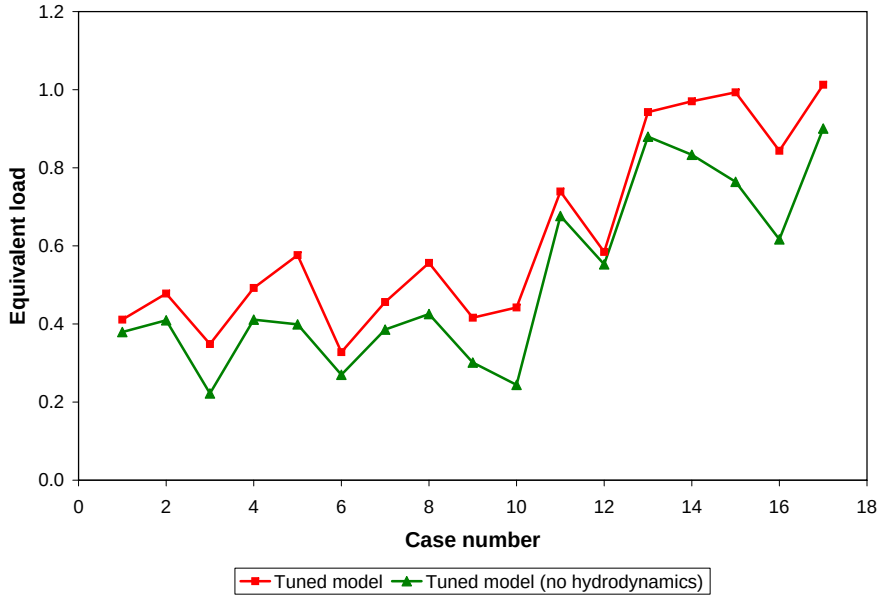

Figure 7.11 Comparison of the *monbetilt* fatigue damage equivalent loads for the normal case, and for a water density of 0 kg/m^3.

Influence of structural dynamics on fatigue damage

Before analyzing the effect of an accurate simulation of the dynamic behaviour of the turbine, the relative importance of structural dynamics should be assessed. In order to evaluate the influence of dynamics on the fatigue damage equivalent loads, static loads are calculated in FLEX5 and compared to the results obtained with initial simulations (shown in figures 7.3 to 7.8).

A set of simulations in stiff conditions (i.e. allowing only one degree of freedom in the system, corresponding to the rotational motion of the rotor) is run in order to evaluate the static loads. For this purpose, three different load cases are analyzed (load cases 5, 10 and 17 from table 7.2). The chosen cases are those which show the highest differences in fatigue damage equivalent loads between simulations and measurements. Equivalent loads from initial and stiff simulations are shown in figure 7.12. Furthermore, comparison of *towbetilt* spectra obtained from initial and stiff simulations are shown in figures 7.13, 7.14 and 7.15, for load cases 5, 10 and 17, respectively.

From figure 7.12 it can be concluded that there is a large variability on the influence of dynamics on fatigue damage equivalent loads. For load case number 10 the difference in the equivalent load reaches 41%, while for load case 17 the difference is reduced to 7%.

In figures 7.13 to 7.15, large differences are observed between the *towbetilt* spectra from initial and stiff simulations. Obviously, in stiff conditions no natural frequency peaks appear, only those corresponding to harmonics from the rotational speed of the turbine.

In addition, in load cases 10 and 17, an excitation of the 2^{nd} natural frequency of the support structure by 3P can be observed. However, the peak corresponding to this natural frequency is much lower than for the 1^{st} natural frequency, and its contribution to the fatigue damage is not expected to be relevant compared to the $f_{0,SS}$ peak. For the load case number 5, no excitation of the 2^{nd} natural frequency of the support structure by 3P occurs.

Finally, results shown in figure 7.12 can be explained from the spectra. The simulation of the load case 5 results in a higher fatigue damage equivalent load than in load case 10, as the $f_{0,SS}$ peak in load case 5 is remarkably higher than in load case number 10 (i.e. $f_{0,SS}$ is further excited in load case number 5 than in load case 10). The same reasoning holds for load cases 17: the peak corresponding to the $f_{0,SS}$ is higher than for the other two, and therefore its fatigue damage equivalent load is also higher.

Moreover, the variations on the fatigue damage equivalent loads between the dynamic and stiff simulations can also be explained based on the areas between the two curves (which represents a difference in energy accumulated in the structure). For both load cases 5 and 10, the area in between the dynamic and stiff curves for the $f_{0,SS}$ peak are in the same range, therefore showing a similar mismatching in equivalent loads between the dynamic and the static case (see figure 7.12). Nevertheless, the area in between the dynamic and stiff simulations for the $f_{0,SS}$ peak for load case 17 is much smaller, therefore showing a lower discrepancy between the dynamic and stiff fatigue damage equivalent loads.

In conclusion, the main source for the discrepancies in the fatigue damage equivalent loads are different excitations of the 1^{st} natural frequency of the

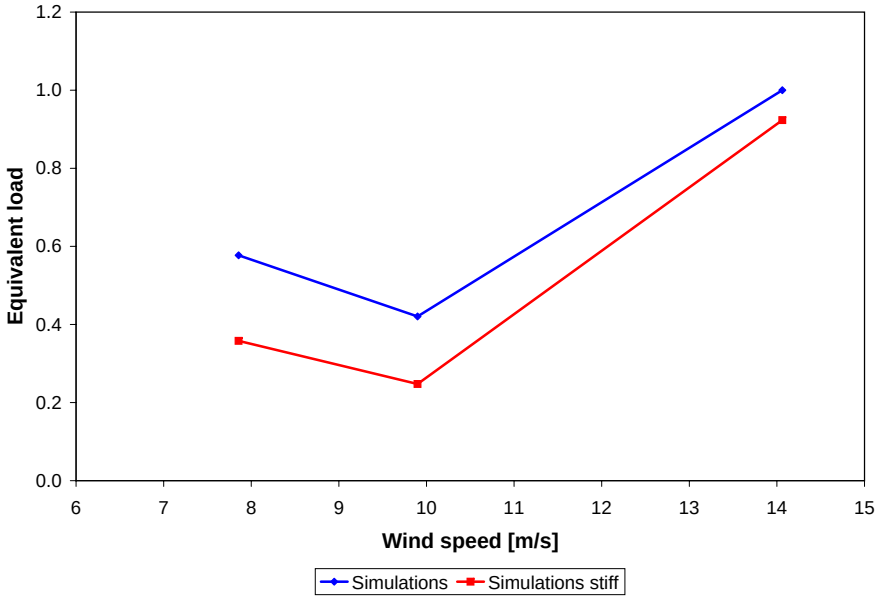

Figure 7.12 Comparison of *towbetilt* fatigue damage equivalent loads between initial simulations and stiff simulations, for load cases 5, 10 and 17.

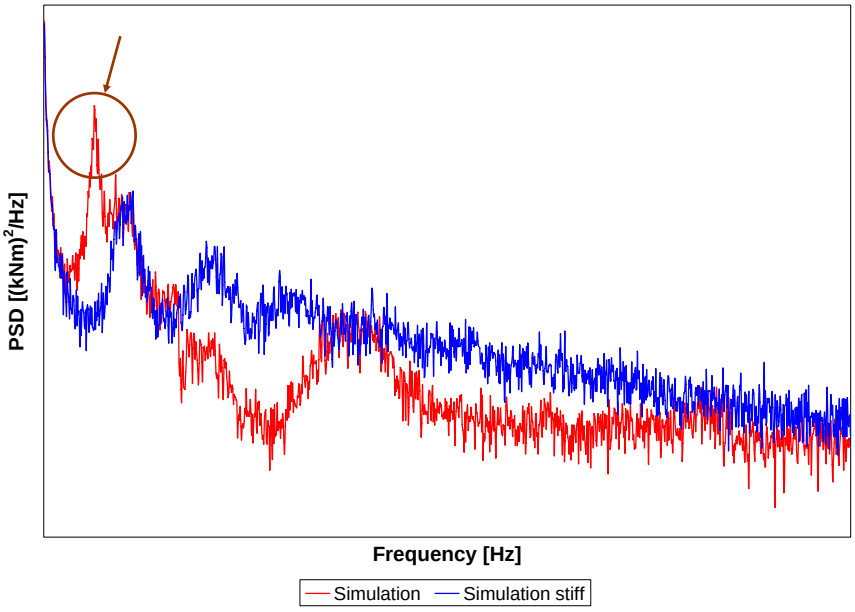

Figure 7.13 Comparison of *towbetilt* spectra from initial simulations and stiff simulations, for load case number 5 (logarithmic scale).

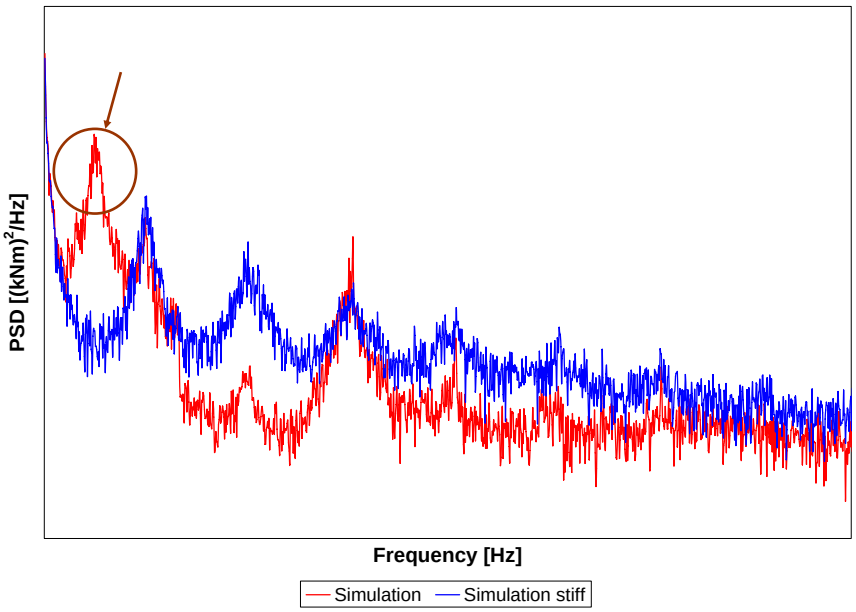

Figure 7.14 Comparison of *towbetilt* spectra from initial simulations and stiff simulations, for load case number 10 (logarithmic scale).

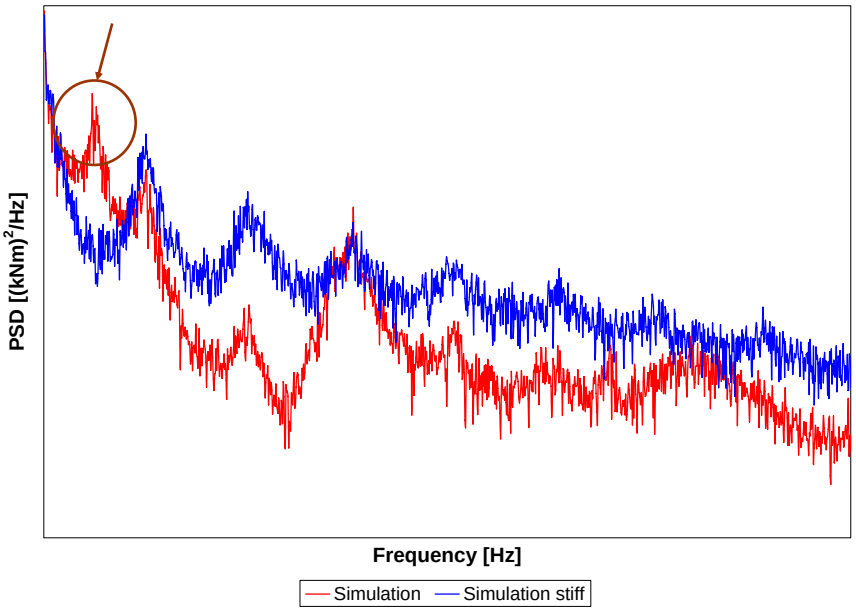

Figure 7.15 Comparison of *towbetilt* spectra from initial simulations and stiff simulations, for load case number 17 (logarithmic scale).

support structure. From figures 7.13 to 7.15, no excitation of the $f_{0,SS}$ by rotational frequencies is observed, and therefore wind and waves are expected to be the source of these different excitations.

Matching between simulated dynamic behaviour and measurements

The model tuning explained in section 6.2 aims at achieving coincident 1st and 2nd natural frequencies with the measurements, for the support structure and the blades. However, other subsystems could have an influence on the dynamic behaviour of the turbine. In order to investigate to what extent the simulation model reflects the real dynamic behaviour of the support structure, measurements and simulations *towbetilt* spectra are studied. A comparison of spectra built up from measurements and from simulations, for load cases 5, 10 and 17 is shown in figures 7.16, 7.17 and 7.18.

The matching between measurements and simulations spectra for these 3 cases is in general quite good. Nevertheless, the 2nd natural frequency of the support structure (highlighted with a brown circle) is highly undamped in the simulation results, with reference to measurements. Furthermore, simulation spectra for both load cases 5 and 10 show a peak in the between the 1P and 2P excitations, which does not correspond to any peak on the measurements spectra. In addition, the 2nd natural frequency of the blades in edgewise direction is notably more damped in the simulation model than in the real structure.

Finally, simulations for all three load cases show a higher damping of the 1st natural frequency of the support structure in the real turbine. A close look into the spectra of load cases 5 and 17 shows that the difference between the $f_{0,SS}$ peak from simulation and from measurements is in the same range bor both load cases. These similar differences result in similar discrepancies in the fatigue damage equivalent loads in figure 7.3. Moreover, a lower difference between the simulated and measured $f_{0,SS}$ peaks in load case 10, result in lower discrepancies in the fatigue damage equivalent loads.

In conclusion, in general the simulation model represents quite accurately the behaviour of the real structure, with slight deviations. However, spectral differences for the $f_{0,SS}$ are the main source for the discrepancies on the fatigue damage equivalent loads. This conclusion is in line with the results from the previous section.

7.3.3.2 Aspects related to wind field generation

Influence of the variation of random seeds for stochastic wind field generation

In the generation of the wind field for FLEX5, the Vindsim program (wind field generation tool) requires a random parameter, called seed. Different seeds lead to different time series, though having identical statistical parameters, namely mean wind speed, turbulence intensity and mean wind direction.

Again, the analysis focuses on load cases 5, 10 and 17. 20 simulations are run for each case, by only varying the random seeds used for wind field generation. Results for the *towbetilt* and *monbetilt* equivalent loads are shown in figures 7.19, 7.20, 7.21, 7.22, 7.23 and 7.24.

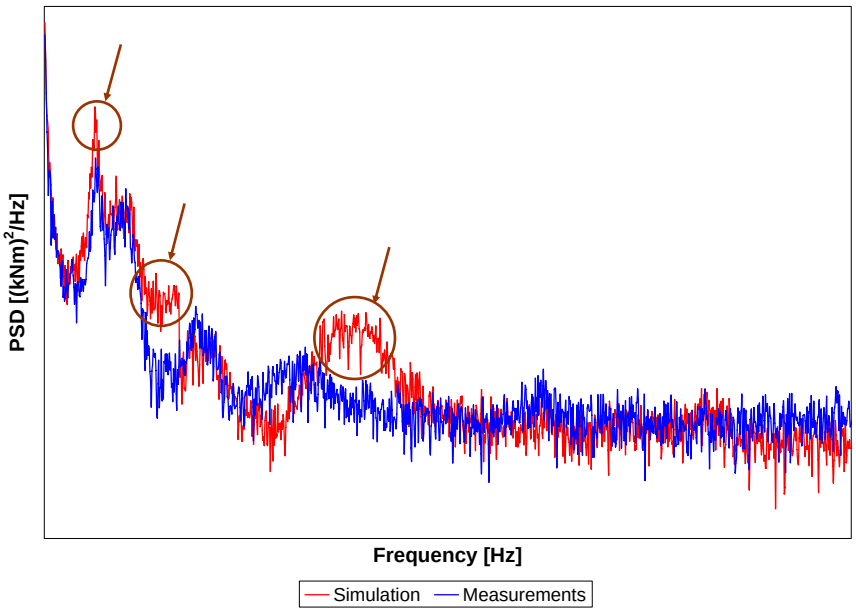

Figure 7.16 Comparison of *towbetilt* spectra between simulation and measurements, for load case 5 (logarithmic scale).

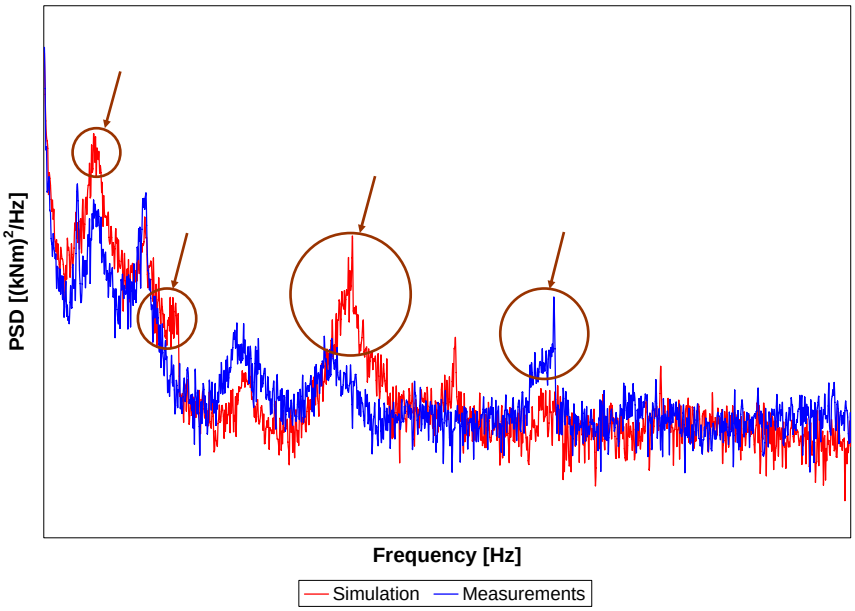

Figure 7.17 Comparison of *towbetilt* spectra between simulation and measurements, for load case 10 (logarithmic scale).

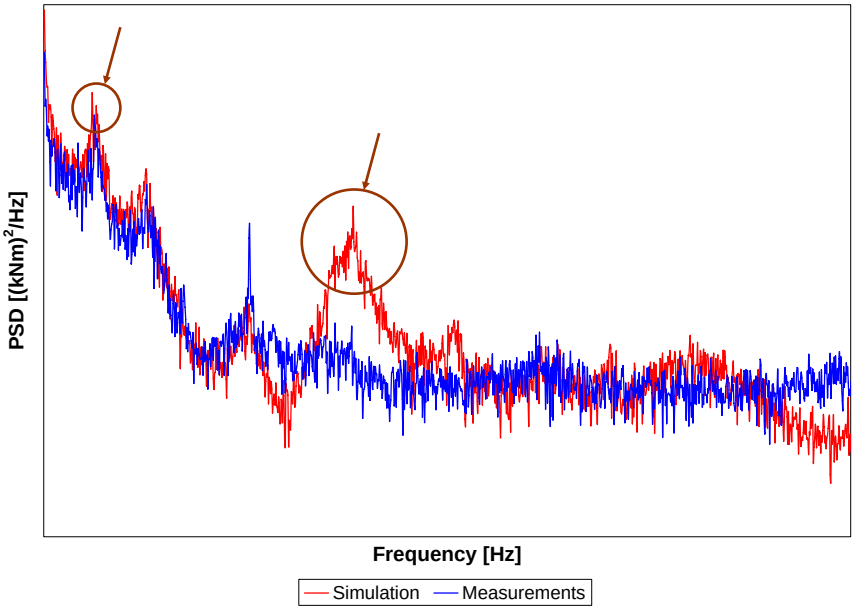

Figure 7.18 Comparison of *towbetilt* spectra between simulation and measurements, for load case 17 (logarithmic scale).

From table 7.3, one main conclusion can be extracted. Differences on the fatigue damage equivalent loads up till 14.4% are observed, hence the variation on the fatigue damage equivalent load can be significant depending on the used wind field.

Table 7.3 Maximum differences in fatigue damage equivalent loads due to the random seed used for wind field generation.

	Towbetilt	**Monbetilt**
Load case 5	**14.42%**	**14.45%**
Load case 10	6.35%	5.66%
Load case 17	11.47%	11.52%

For all three load cases, wind field A corresponds with the wind field used for the calculation of fatigue damage equivalent loads shown in figures 7.3 to 7.8. The maximum differences on fatigue damage equivalent loads resulting from the use of different wind field than wind field A are observed again in load case number 5 (see table 7.4).

Therefore, the use of a simulated wind field different than the actual wind field on-site does not have a significant influence on the discrepancies observed between measurements and simulations.

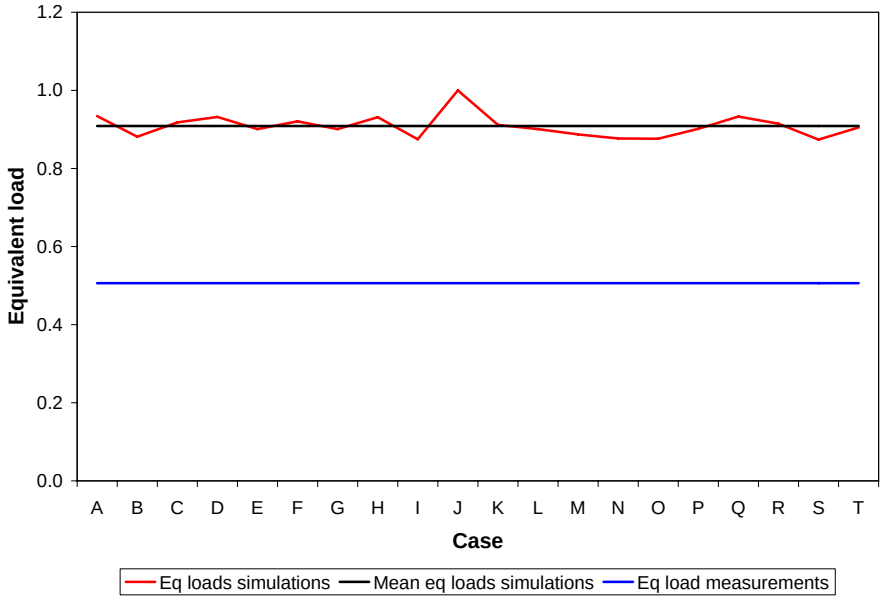

Figure 7.19 *Towbetilt* fatigue damage equivalent loads for different random seeds, for load case number 5 (7.86 m/s wind speed).

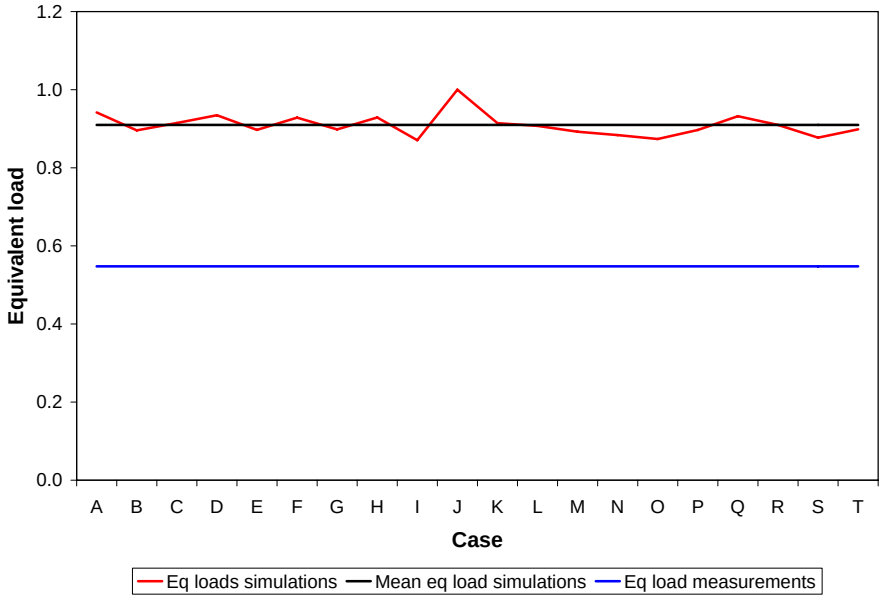

Figure 7.20 *Monbetilt* fatigue damage equivalent loads for different random seeds, for load case number 5 (7.86 m/s wind speed).

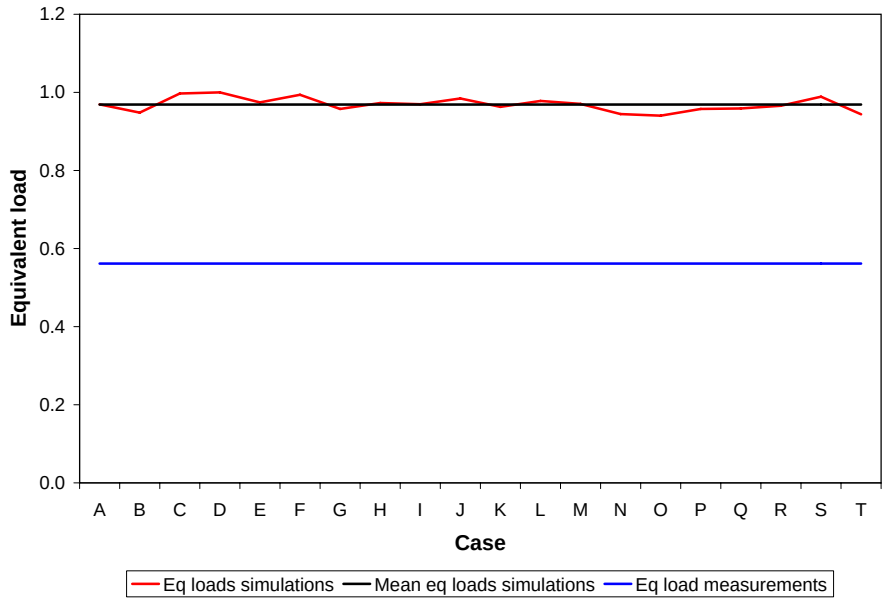

Figure 7.21 *Towbetilt* fatigue damage equivalent loads for different random seeds, for load case number 10 (9.90 m/s wind speed).

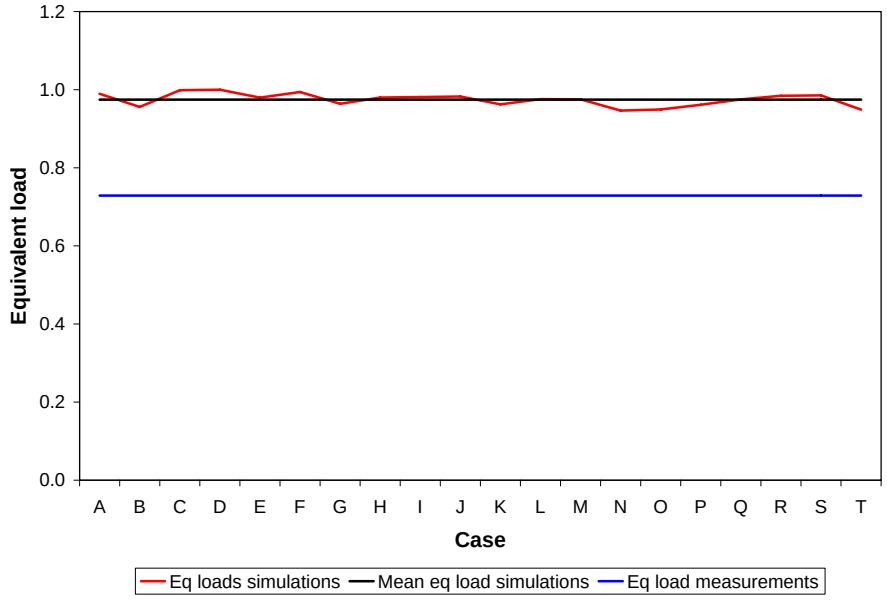

Figure 7.22 *Monbetilt* fatigue damage equivalent loads for different random seeds, for load case number 10 (9.90 m/s wind speed).

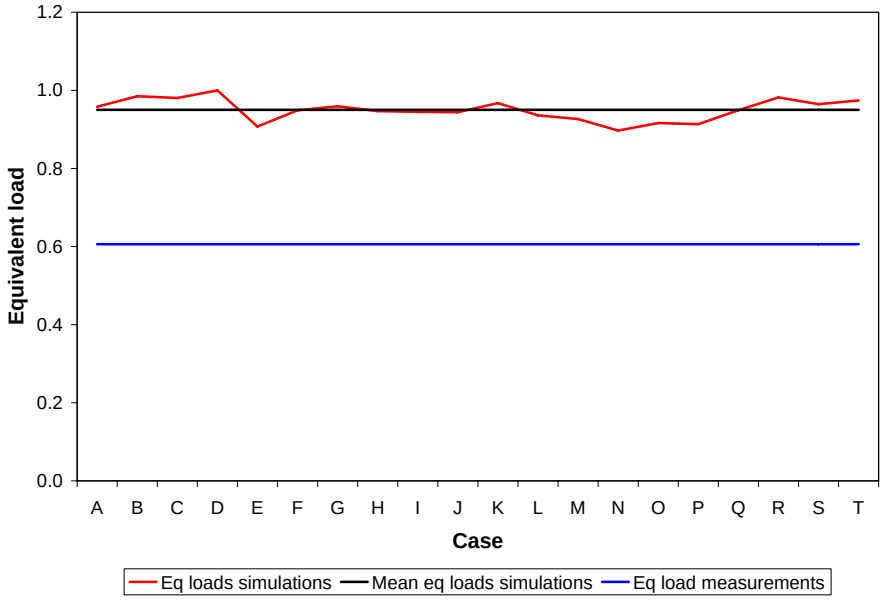

Figure 7.23 *Towbetilt* fatigue damage equivalent loads for different random seeds, for load case number 17 (14.06 m/s wind speed).

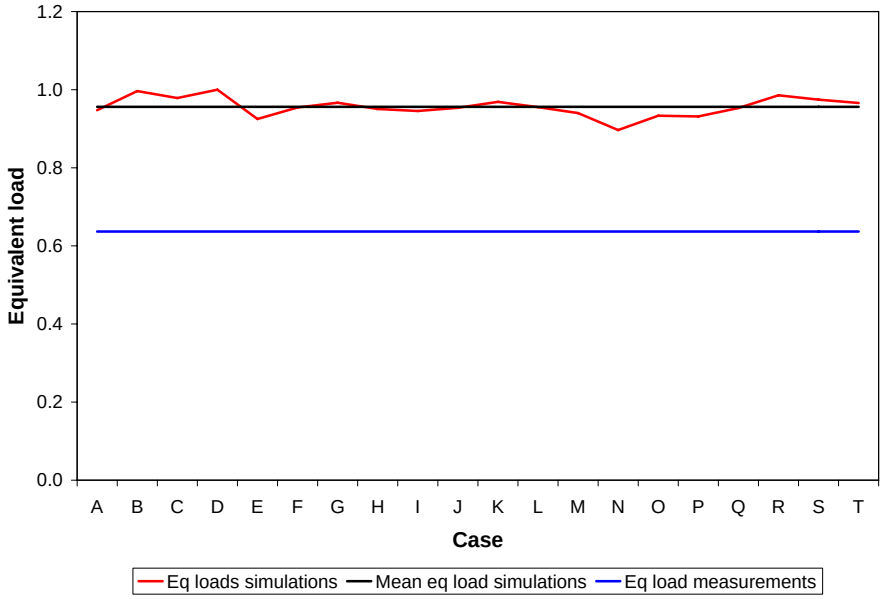

Figure 7.24 *Monbetilt* fatigue damage equivalent loads for different random seeds, for load case number 17 (14.06 m/s wind speed).

Table 7.4 Maximum differences in fatigue damage equivalent loads due to the random seed used for wind field generation, w.r.t. wind field A.

	Towbetilt	**Monbetilt**
Load case 5	**6.45%**	**7.22%**
Load case 10	2.98%	4.06%
Load case 17	6.34%	5.37%

Influence of coherence and length scale

In FLEX5, the definition of the coherence function is done according to IEC standards (IEC 61400 ed. 3 [14]). The decay parameter is therefore set to 12 (though for the previous edition of the standards IEC 61400 ed. 2 [16] had a value of 8.8), whilst the longitudinal turbulence scale parameter is has a value of 42 m. The decay parameter regulates the shape of the coherence function, determining how sharply the decrease of the coherence with increasing distances is. The influence of the turbulence scale parameter Λ_1 on the coherence function shape is almost negligible, though being relevant for the shape of the wind speed spectrum. Appendix D provides further information on this issue.

Table 7.5 Load cases for the analysis of the influence of the decay parameter and turbulence length scale on the fatigue damage equivalent loads.

Case	**Decay** [-]	Λ_1 [m]	$\mathbf{L_c}$ [m]
A	6.0	42.0	147
B	8.8	42.0	147
C (IEC ed.3)	12.0	42.0	147
D	14.0	42.0	147
E	16.0	42.0	147
F	12.0	60.0	210
G	12.0	80.0	280

In this section the influence of these two parameters is analyzed. Five different values of the decay parameter (6, 8.8, 12, 14 and 16) and three of the longitudinal turbulence scale parameter Λ_1 (42, 60 and 80) are used. Seven combinations of these parameters are studied (see table 7.5).

The influence of the decay parameter and Λ_1 on the *towbetilt* fatigue damage equivalent loads is shown in figures 7.25, 7.26 and 7.27. This is done for the three load cases analyzed in the previous section, i.e. load cases number 5, 10 and 17 from table 7.2. The variation of the turbulence length scale has a lower influence than the variation of the decay parameter on the equivalent loads, as

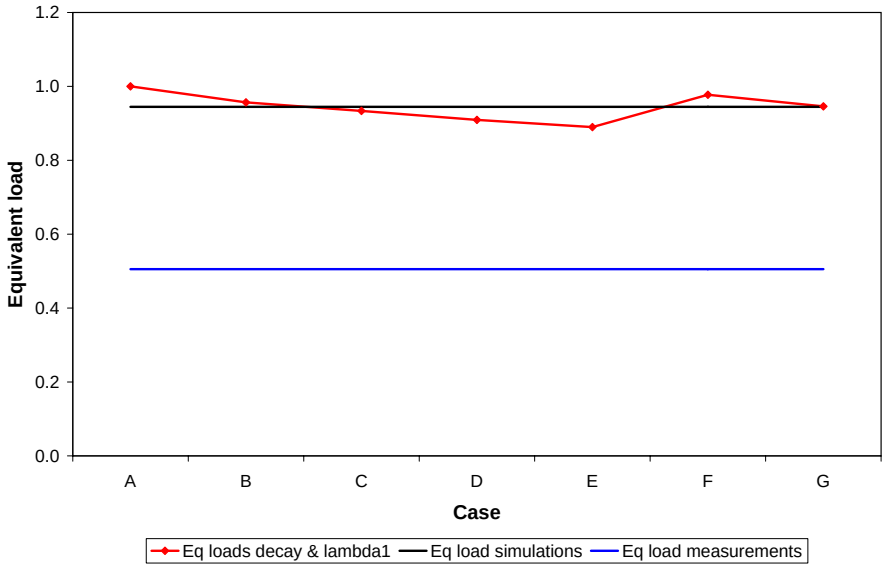

Figure 7.25 Variation on the *towbetilt* fatigue damage equivalent load with decay parameter and turbulence length scale (load case number 5).

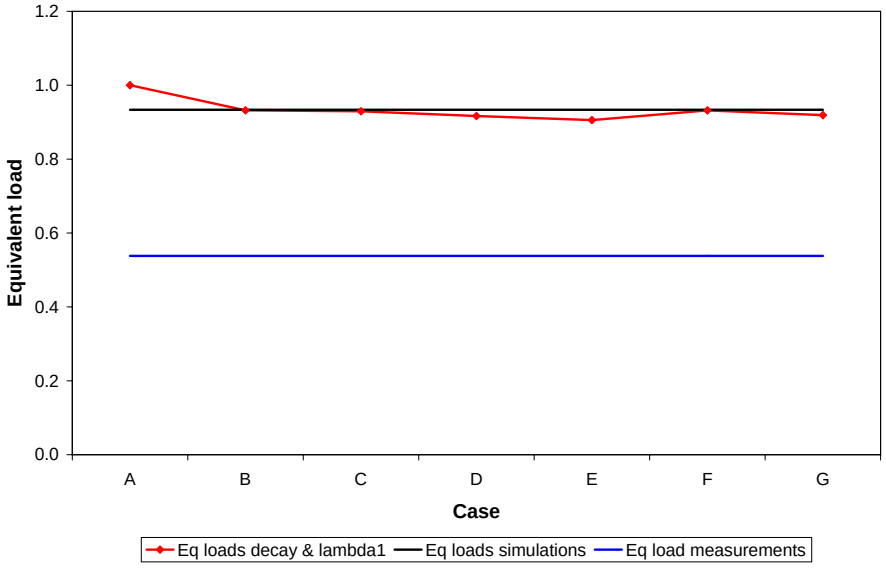

Figure 7.26 Variation on the *towbetilt* fatigue damage equivalent load with decay parameter and turbulence length scale (load case number 10).

can be seen from the figures, especially for higher wind speeds.

Thus, the maximum differences registered for all the three load cases are caused by a change in the decay parameter from 6 to 16. Maximum differences on the equivalent loads with reference to the IEC ed.3 case (decay parameter 12, Λ_1 42 m) are presented in table 7.6.

Table 7.6 Maximum differences in *towbetilt* fatigue damage equivalent loads due to variations on the decay parameter, w.r.t. IEC ed.3 case.

	Decay parameter	Λ_1
Load case 5	11.02%	**4.68%**
Load case 10	9.44%	1.11%
Load case 17	**26.06%**	4.12%

In conclusion, the decay parameter can strongly influence the the fatigue damage equivalent load, whilst the effect of the turbulence length scale is negligible. However, as can be seen in figures 7.25 to 7.27, the decay parameter does not appear to be the source for the big discrepancies between measurements and simulations for load cases 5, 10 and 17.

7.3.3.3 Aspects related to measurements and operational conditions

Influence of yaw misalignment

From figures 7.3 and 7.5 it can be concluded that the fore-aft fatigue damage equivalent loads are normally overestimated by the simulation model. However, equivalent loads in side-to-side direction are clearly underestimated, as can be seen in figures 7.4 and 7.6. Therefore, the possibility of a yaw misalignment as a source of error is considered. The yaw signal has been errored during the measurement campaign (see section 3.2), and therefore no information on this issue is provided by the measurements.

Again, load cases 5, 10 and 17 from table 7.2 are analyzed in this investigation, assuming 4 different yaw misalignments: 15°, 30°, 45° and 60°. Results for the *towbetilt* fatigue damage equivalent loads are plotted in figure 7.28.

In figure 7.28, yawed inflows result in a much higher fatigue damage equivalent load for the fore-aft direction. Small variations on the wind direction lead to large variations on the angle of attack, which could result in large changes on the instantaneous load on the turbine. Hence, larger amplitudes are found in the bending moment time histories. This effect results in higher fatigue damage. Therefore, yaw misalignment is discarded as the source of error.

Influence of wind and waves misalignment

Wind and waves misalignment is considered as a real possibility at the Arklow

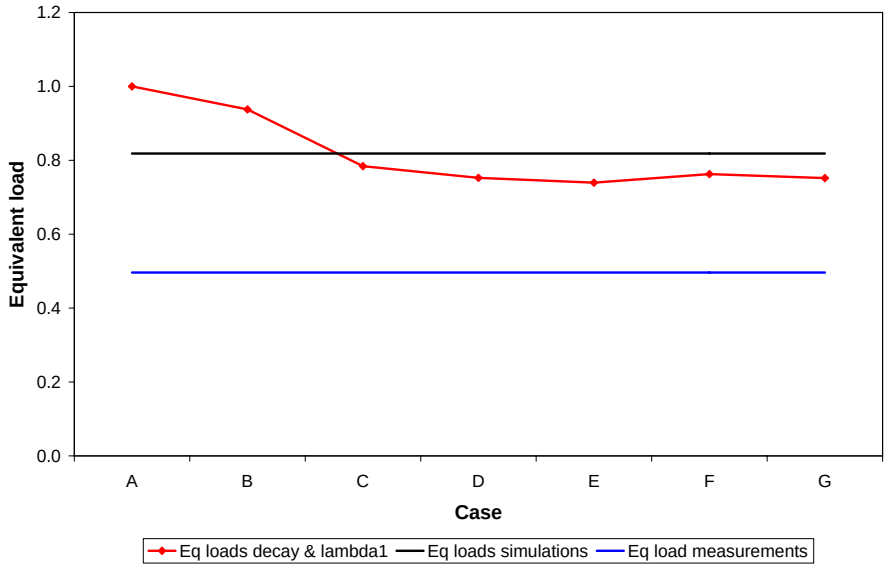

Figure 7.27 Variation on the *towbetilt* fatigue damage equivalent load with decay parameter and turbulence length scale (load case number 17).

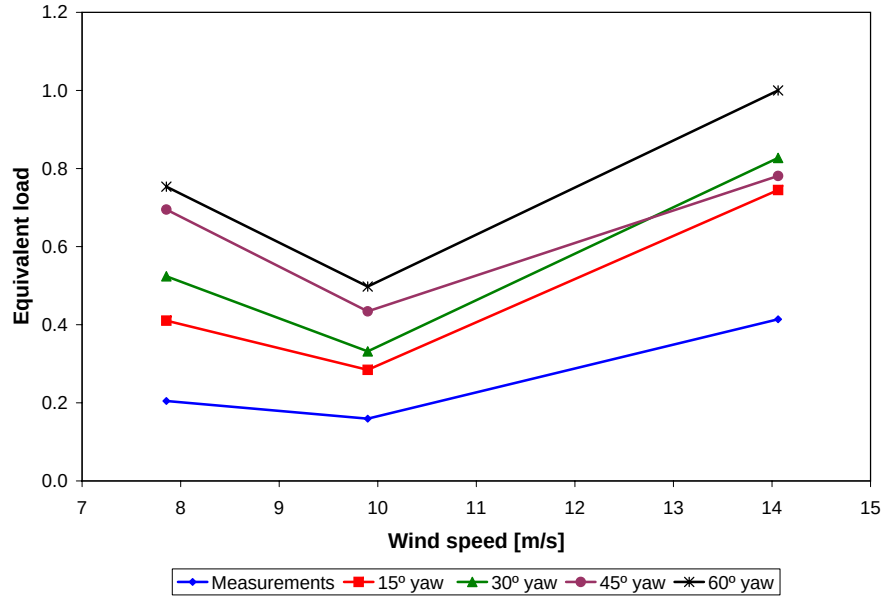

Figure 7.28 Fatigue damage equivalent loads for the *towbetilt*, for different yawed inflows.

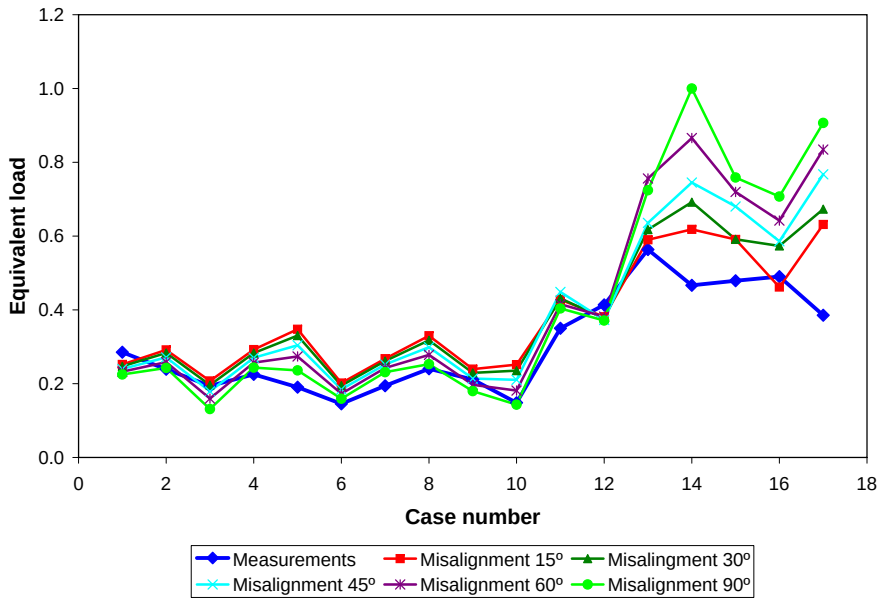

Figure 7.29 *Towbetilt* fatigue damage equivalent loads, for measurements and simulations with different wind and waves misalignments.

Bank. No waves or current direction have been measured during the measurement campaign. Nevertheless, the effect of the sudden variations in water depth at the bank could be the origin for wave diffraction. Furthermore, another possible source for wind and waves misalignment could be the delayed response of waves direction to changes in the direction of the wind.

All 17 load cases from table 7.2 are simulated for wind and waves misalignments of 15º, 30º, 45º, 60º and 90º. In figure 7.29 the results for the *towbetilt* fatigue damage equivalent loads are shown for all five wind and waves misalignments, for all 17 load cases. Only three cases (number 14, 15 and 17) are conflictive, as measurements do not have an accurate corresponding simulation result.

Therefore, a different wind and waves misalignment could be assumed for each of the 17 load cases. Furthermore, also *towberoll* and *monberoll* are used in this section for choosing the most appropriate misalignment, that is, the best match with measurements. Best matching cases are shown in table 7.7, and comparisons between measurements and best matches in figures 7.30, 7.31, 7.32 and 7.33. The equivalent loads for the blades remain almost unchanged with reference to the aligned-wind-and-waves case.

Again, load cases number 5, 10 and 17 are still conflictive, especially regarding the fore-aft bending moments (i.e. *towbetilt* and *monbetilt*). On the other hand, all the other cases show differences on the *towbetilt* equivalent loads lower than 35% with reference to the measurements. In the case of the *monbetilt*, *towberoll* and *monberoll*, these differences are even lower.

In conclusion, it seems clear that there is a wind and waves misalignment for all 17 load cases chosen for fatigue analysis verification. Not only the fore-aft

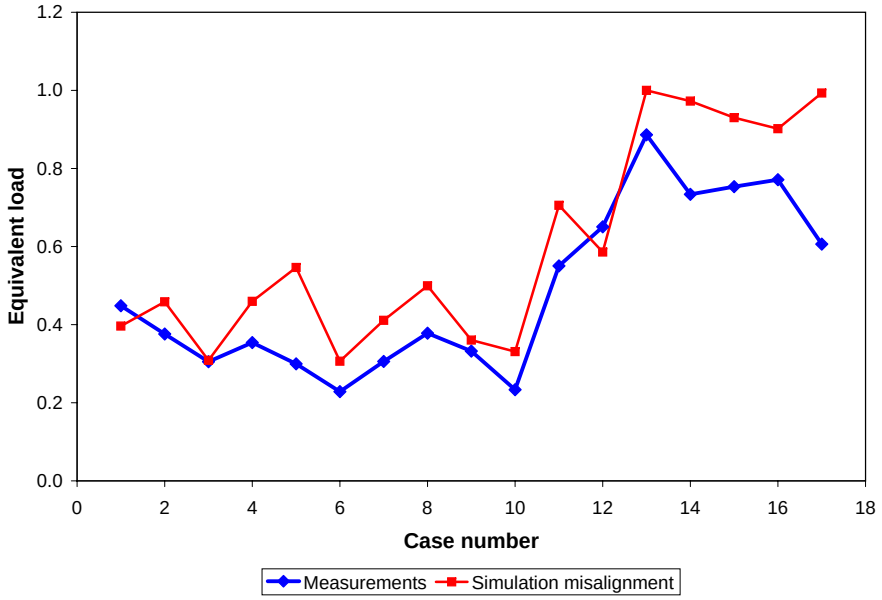

Figure 7.30 Fatigue damage equivalent loads for the *towbetilt*, for measurements and best matching simulations.

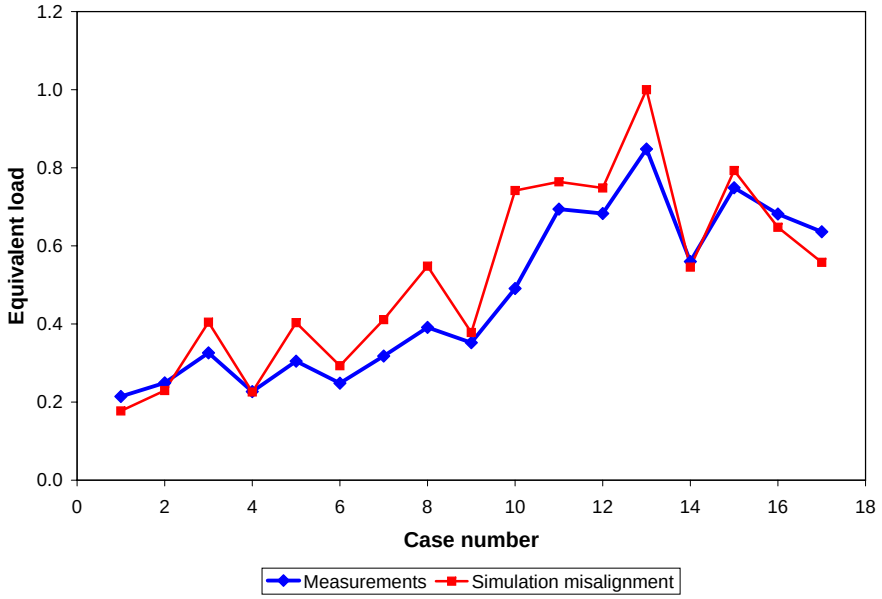

Figure 7.31 Fatigue damage equivalent loads for the *towberoll*, for measurements and best matching simulations.

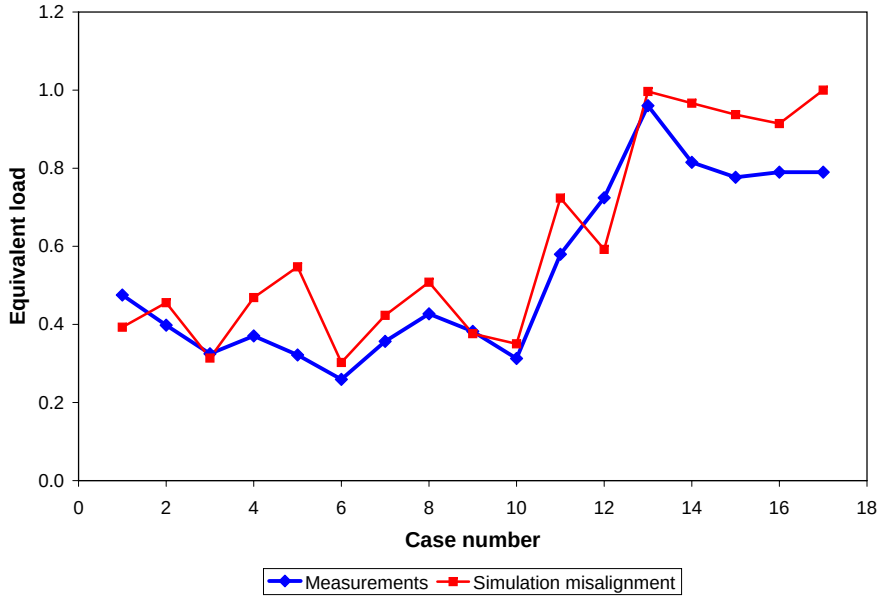

Figure 7.32 Fatigue damage equivalent loads for the *monbetilt*, for measurements and best matching simulations.

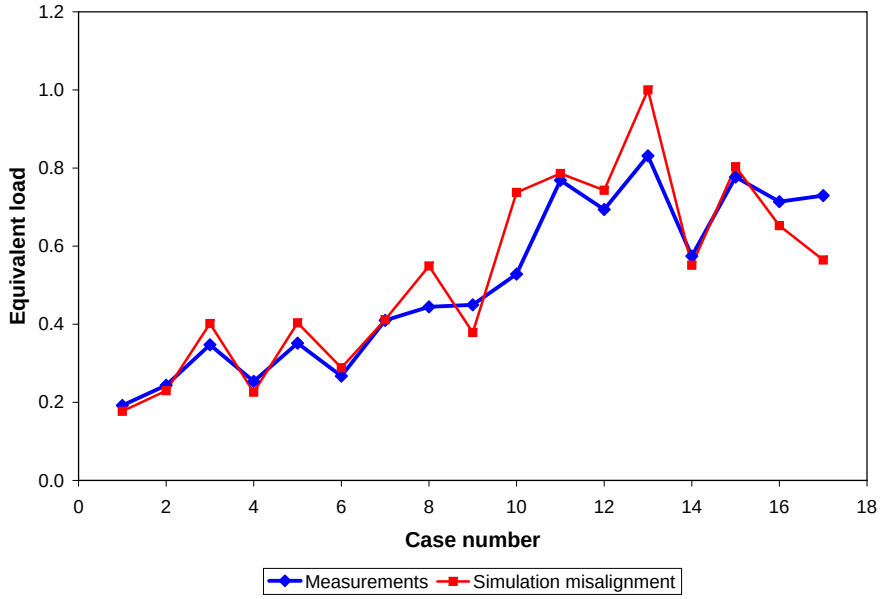

Figure 7.33 Fatigue damage equivalent loads for the *monberoll*, for measurements and best matching simulations.

Table 7.7 Best matching cases for the verification of the fatigue analysis.

No.	H_s [m]	T_z [s]	$\bar{U}$ [m/s]	I [%]	Wind and waves misalignment [º]
1	0.35	2.57	6.07	7.90	15
2	0.33	2.40	6.24	8.30	15
3	0.48	2.79	6.96	4.86	30
4	0.48	2.74	6.98	8.74	15
5	0.62	3.08	7.86	7.80	15
6	0.62	3.66	7.77	5.34	30
7	0.77	3.58	8.81	6.42	30
8	0.84	4.00	8.77	7.21	30
9	1.05	4.34	9.93	4.88	30
10	1.06	4.30	9.90	3.74	45
11	1.22	4.12	10.96	8.06	45
12	1.27	4.20	10.87	6.68	45
13	1.51	5.20	11.78	7.11	45
14	1.50	4.83	12.21	8.65	15
15	1.70	5.20	12.83	7.95	30
16	1.70	5.20	12.84	5.74	30
17	2.08	5.81	14.06	9.71	15

bending moments are more or less accurately simulated with these conditions, but also the side-to-side bending moments. However, 3 out of the 17 load cases are still far away from measurements equivalent loads. Attention should be drawn to the fact that only 5 possible wind and waves misalignments are used: it is quite probable that intermediate values of this misalignment give better results.

Influence of the distance between the turbine and the anemometer

As stated in section 3.1, the distance between the metmast and turbine 1 is 255 m (i.e. $2.45 \cdot D$ aprox.). This value complies with IEC 61400-12 ed. 3, which sets a distance between the metmast and the wind turbine of $2.5 \cdot D \pm 5\%$. Normally, when not measuring in the wake of any turbine, wind conditions at the meteorological mast should be almost identical to those at turbine 1. However, the distance between the metmast and the turbine makes it possible to measure different wind speeds and directions than those at the rotor plane.

This phenomenon is observed in the measurements. In some cases, the wind speed trend in the time series does not match the power output time series, as can be seen in figure 7.34 for load case number 5. The brown circle indicates a peak on the Risø anemometer at the meteorological mast which does not have a corresponding peak neither on the power output nor on the nacelle anemometer time series. The nacelle anemometer measurements, though not being representative of the absolute values of the wind speed at the rotor plane (due to high turbulence induced by the rotor), reflects wind speed trends at the

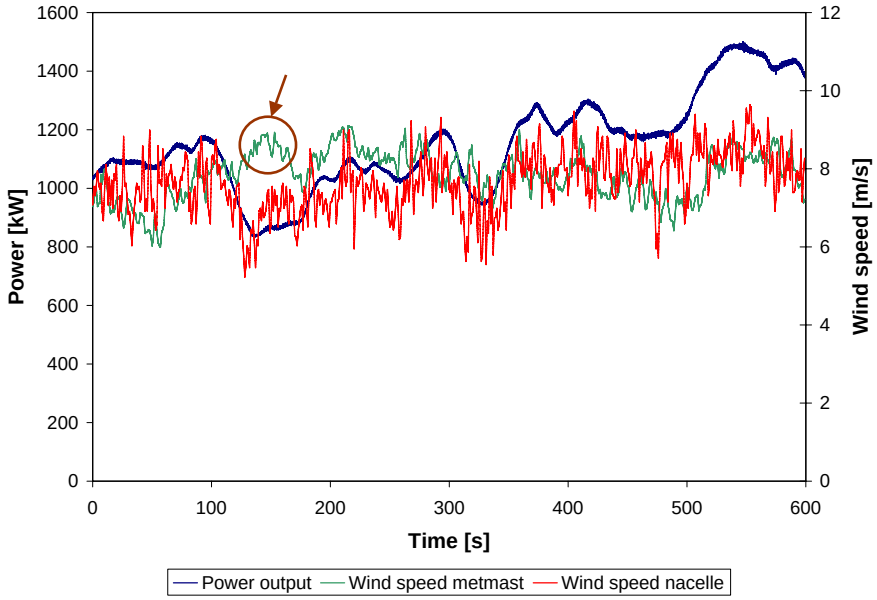

Figure 7.34 Power output, wind speed (Risø anemometer) and wind speed (nacelle anemometer) time series for load case number 5.

rotor plane quite accurately. Hence, the use of wind data measured at a certain distance from the rotor plane induces an error, though impossible to quantify as no reliable anemometers are installed at the rotor plane for comparison.

7.3.3.4 Conclusions of the validation of the tuned model

The analysis focuses on seventeen 10-min load cases which are selected from the scatter diagram. Results from initial simulations do not reasonably match the measurements, and therefore further invetigations have been performed. All these investigations are mainly focused on the support structure fore-aft bending moments. The main outcome of these investigations are summarized below:

1. The main source of error in the simulations is originated in a wind and wave misalignment on all 17 verification cases ranging from 15° to 45°.

2. Errors up to 7.5% could be induced due to the random seed used for wind field generation in FLEX5. In addition, the use of different coherence decay parameters does not have a large influence on the discrepancies between mesurements and simulations.

3. In general, dynamic behaviour of the turbine is quite accurately simulated. However, deviations on the excitations of the $f_{0,SS}$ are identified in the spectra, which are the main source for fatigue damage equivalent loads discrepancies. These excitations do not come from rotational frequencies, but from wind and waves.

4. Hydrodynamic loading on the structure is important. In some cases it is not very relevant for fore-aft bending moments, but it is for the bending moments in side-to-side direction.

5. The differences between the equivalent loads from simulations and measurements are not due to yaw misalignment.

6. In some cases, the conditions measured at the metmast do not match the conditions at the rotor plane. However this error is not quantifiable, as no reliable measurements can be obtained at the rotor plane itself.

7.3.4 Comparison between design model and tuned model

In order to make a comparison between the performance of the design model and the tuned model, new simulations of the verification load cases are performed with the model provided by GE Wind Energy. The wind and waves misalignment shown in table 7.7 is considered in the simulations, as this misalignment has been identified as the main source of error in the previous section.

Figures 7.35, 7.36, 7.37 and 7.38 show the comparison of the results from measurements and simulations (both with the tuned and the design GE models) for the tower and monopile, in both fore-aft and side-to-side directions. In figures 7.39 and 7.40 the comparison for the blade root bending moments, in flapwise and edgewise directions, is shown.

From figures 7.35 and 7.37 it can be concluded that, in general, results from the original GE Wind Energy model in the fore-aft direction are quite close to those from the tuned model, except for wind speeds higher than 13 m/s cases (i.e. load cases number 15 and 16). Slight variations between the *towbetilt* results from design and tuned models are identified in 9 out of the 17 cases. In the case of the monopile, the mismatching is more notorious, as the length of the monopile in the design model is different than the real one. Maximum differences between fatigue damage equivalent loads obtained from measurements and simulations for the *towbetilt* are 82.3%, in the case of the tuned model (for load case number 5), and 71.4% for the design model (load case 17). For the monopile, maximum deviations happen again in load case 5 for the tuned model (70.0%) and in case number 17 for the design model (79.1%). In spite of these high maximum differences, average deviation from the tuned model to measurements results is 28.56% for the *towbetilt*, and 19.3% for the *monbetilt*. In the case of the design model, these differences increase up to 40.0% for the tower bottom and 35.4% for the monopile.

Nevertheless, the design model approximates the side-to-side bending moments on the support structure much less accurately than the tuned model, as can be seen in figures 7.36 and 7.38. Maximum differences between measurements and simulations for the *towberoll* occur on load case 10 for both the tuned (51.1%) and the design (159.2%) models. In the case of the monopile, these deviations reach 39.6% for the tuned model, and 156.7% for the design model, again both of them for load case number 10. However, mean deviations of the results obtained with the tuned model from the measurements are 17.1% for the *towbetilt* and 12.4% for the *monbetilt*. For the design model case, average

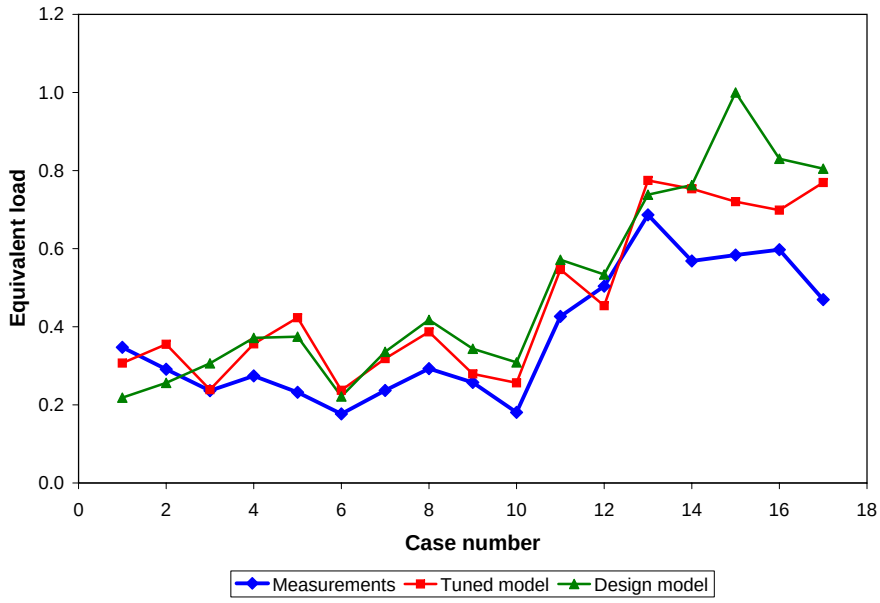

Figure 7.35 Comparison of the *towbetilt* fatigue damage equivalent loads for the verification load cases, from measurements and simulations (with both design and tuned model).

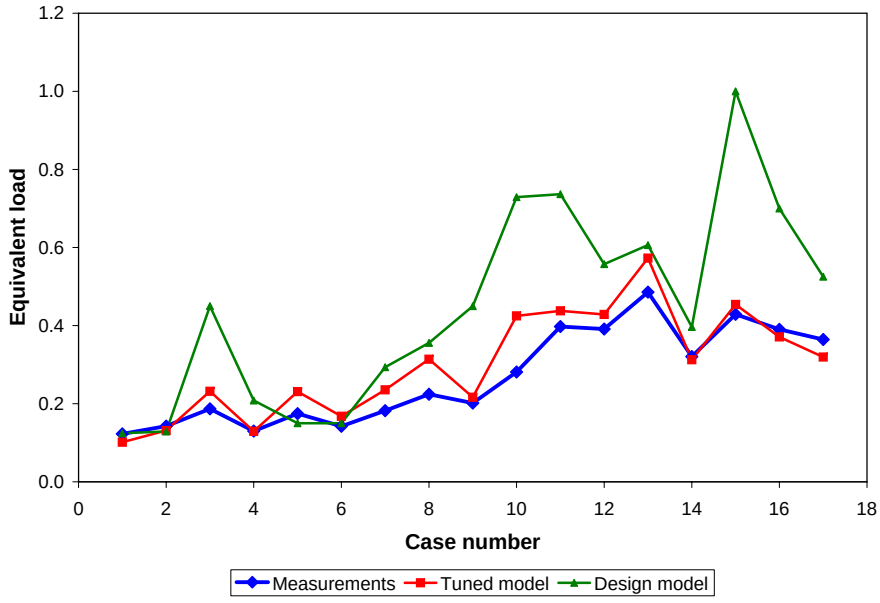

Figure 7.36 Comparison of the *towberoll* fatigue damage equivalent loads for the verification load cases, from measurements and simulations (with both design and tuned model).

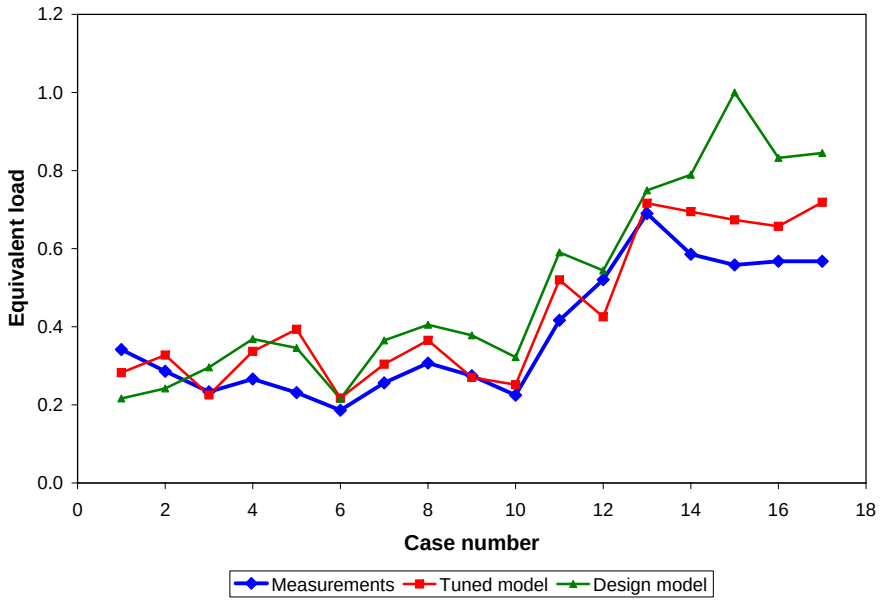

Figure 7.37 Comparison of the *monbetilt* fatigue damage equivalent loads for the verification load cases, from measurements and simulations (with both design and tuned model).

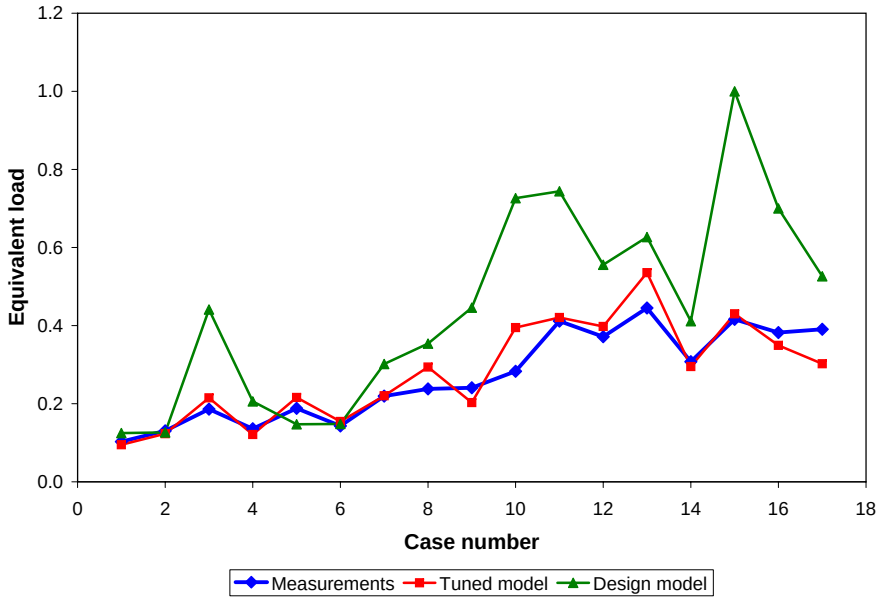

Figure 7.38 Comparison of the *monberoll* fatigue damage equivalent loads for the verification load cases, from measurements and simulations (with both design and tuned model).

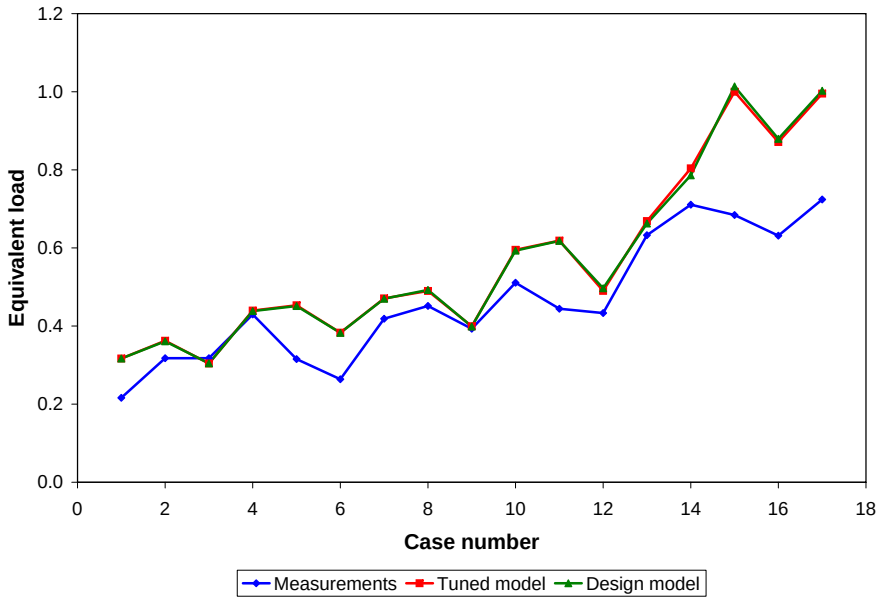

Figure 7.39 Comparison of the *blbef* fatigue damage equivalent loads for the verification load cases, from measurements and simulations (with both design and tuned model).

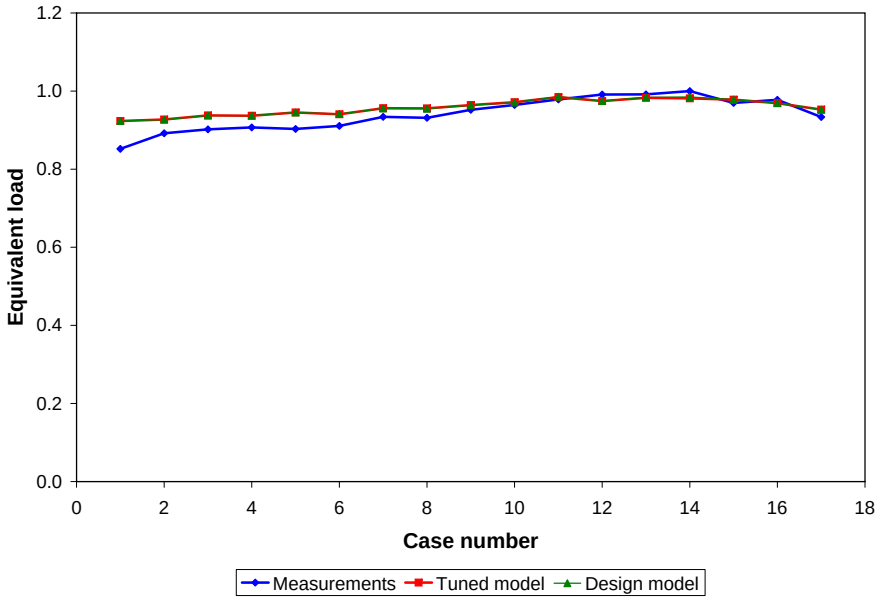

Figure 7.40 Comparison of the *blbee* fatigue damage equivalent loads for the verification load cases, from measurements and simulations (with both design and tuned model).

differences from the equivalent loads obtained from measurements are 62.7% at the tower bottom and 60.6% on the monopile at mudline level.

For the blades, results from both design and tuned model are approximately equal. The fact that no tuning of the blade model has been carried out results in similar equivalent loads for both the tuned and the design model. Maximum differences between the fatigue damage equivalent loads obtained from measurements and simulations reach 46.5% in flapwise direction, and 8.4% in edgewise direction, both occurring in load case 1. Nevertheless, mean deviations of the simulation models from the measurements are 22.4% for the flapwise direction and 2.0% in edgewise direction.

Finally, it should be pointed out that equivalent loads obtained with the design model, both for the tower and monopile in fore-aft and side-to-side directions, are in general higher than real loads. Moreover, this behaviour is observed also in results obtained from the tuned model, though to a lower extent (e.g. for bending moments on the monopile in side-to-side direction there is no clear trend). The same happens, with both models, on the blade root bending moments in flapwise direction.

7.4 Conclusions

The main conclusions from the fatigue analysis are summarized below:

1) The tuned model approximates the behaviour of turbine 1 more accurately than the design model. The main differences are observed in the side-to-side bending moments on the support structure. The tuned model calculates the bending moments on the support structure in fore-aft direction slightly better, as well. However, bending moments on the blades are equally simulated, with better results in edgewise direction than in flapwise direction.

2) A certain wind and waves misalignment has been discovered for all verification load cases. This effect has the largest contribution to the discrepancies between the fatigue damage equivalent loads obtained from simulations and from measurements.

3) In spite of the shallow water depth and mild sea conditions at the Arklow Bank, hydrodynamic loads on the support structure are not negligible, and could have a critical contribution for the fatigue damage equivalent loads, especially on the side-to-side direction.

4) No important influence from the wind field generation is expected for the studied load cases.

5) Dynamic behaviour of the support structure is accurately simulated. Nevertheless, spectral differences for the peak corresponding to the $f_{0,SS}$ are identified. The source of these excitations are not rotational frequencies, but wind and waves.

6) The differences between the equivalent loads from simulations and measurements are not due to yaw misalignment.

7) Design load cases are not comparable to the verification load cases. Turbulence intensity and zero up-crossing period design values have not been found in the measurements, and therefore these two parameters have been skipped from the selection criteria. Furthermore, turbulence intensity and zero up-crossing period values from verification load cases are much lower than those used for design. As turbulence intensity is a critical parameter for fatigue calculations, any further comparison between design and verification load cases would result in unreliable results.

Chapter 8

Analysis of severe sea states

During the measurements period, no extreme loads have been measured. However, some severe sea states have been measured during the measurement campaign. A short term (10 min) load analysis of these severe measured weather conditions is carried out, in order to assess the behaviour of the turbine under severe sea states. Two possible situations are analyzed: most severe sea states with the turbine in operation and when the turbine is stopped. The analysis is carried out in terms of short term (10 min) fatigue damage equivalent load, as no real extreme event is studied here.

As in the previous chapter, due to confidentiality issues all figures involving equivalent loads in this chapter are normalized, referring all the values of the y-axis to the maximum in each graph.

8.1 Severe sea state cases selection

The objective of this analysis is the assessment of the behaviour of the turbine under severe sea state conditions, both with wind speeds around cut-out wind speed (still in operation) and above it (already stopped). All the chosen cases above cut-out wind speed have been measured within a 4 h period, starting on the 7^{th} of January of 2007, at 23:00 h. For the chosen cases below cut-out wind speed, two of them occur during the aforementioned 4 h period, whilst the other 3 cases happen within a 1.5 h period, starting on 27^{th} of October, at 18:35 h. All selected load cases (for both in operation and not in operation) are shown in table 8.1.

8.2 Comparison of results

The same approach explained in section 7.2.1 is applied here. Fatigue damage equivalent loads are determined through *rainflow counting*, by using an inverse slope m of the S-N curve of 3 for the support structure, and 12 for the blades. All fatigue damage equivalent loads are calculated for a number of cycles of 600. Finally, stochastic wind fields are generated by means of a Kaimal model,

Table 8.1 Load cases for the severe sea state analysis.

State	Case	H_s [m]	T_z [s]	$\bar{U}$ [m/s]	I [%]
In operation	A	1.99	5.17	25.00	6.75
	B	2.03	5.76	25.21	7.39
	C	2.13	5.85	25.78	6.26
	D	2.25	5.30	25.49	6.68
	E	2.37	5.67	25.05	6.86
	F	2.21	6.12	25.44	7.65
Not in operation	G	2.21	6.12	26.53	8.11
	H	2.21	6.12	26.90	7.27
	I	2.17	5.68	26.12	7.39
	J	2.17	5.68	26.84	7.93
	K	2.17	5.68	26.35	6.93

whilst wave fields are generated based on the discretization of the PSD of the measured wave heights.

Assumptions described in section 7.3.2 are also considered for the simulations with severe sea states.

8.2.1 Severe sea states with the turbine in operation

Figures 8.1, 8.2, 8.3 and 8.4 show the equivalent loads for the tower and monopile, in fore-aft and side-to-side directions, for six cases in which the turbine is operating.

The tuned model approximates the behaviour of the support structure in fore-aft direction more accurately than the design model. However, differences in accuracy are small, especially regarding the bending moments at tower bottom. Maximum differences on the *towbetilt* fatigue damage equivalent loads between simulations and measurements are 24.5% for the tuned model, and 32.8% for the design model, both happening in load case B. Variations for the monopile are larger on simulations performed with the design model, as expected, due to overestimation of the length of the monopile on the design model. In this case, maximum differences between measurements and simulations are 16.25% for the tuned model, and 36.2% for design model, both happening again in load case B. Average differences between tuned model and measurements equivalent loads are 12.5% (for the tower bottom) and 5.8% (for the monopile at mudline level). In the case of the design model, these mean deviations are in the order of 15.5% and 56.5%, respectively.

The design model provides slightly worse results than the tuned model in side-to-side direction. Maximum differences between measurements and simulations for the *towberoll* equivalent loads are 24.3% in the case of the tuned model (happening in load case D)), and 44.4% for design model (for load case A). For the monopile, maximum differences are 31.4% with the tuned model (load

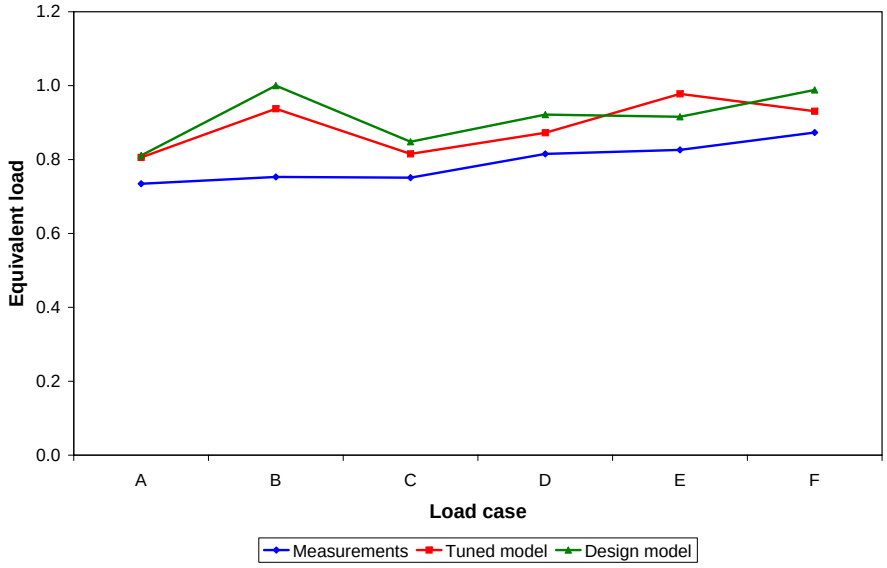

Figure 8.1 Fatigue damage equivalent loads of the *towbetilt*, for severe sea state load cases with the turbine in operation.

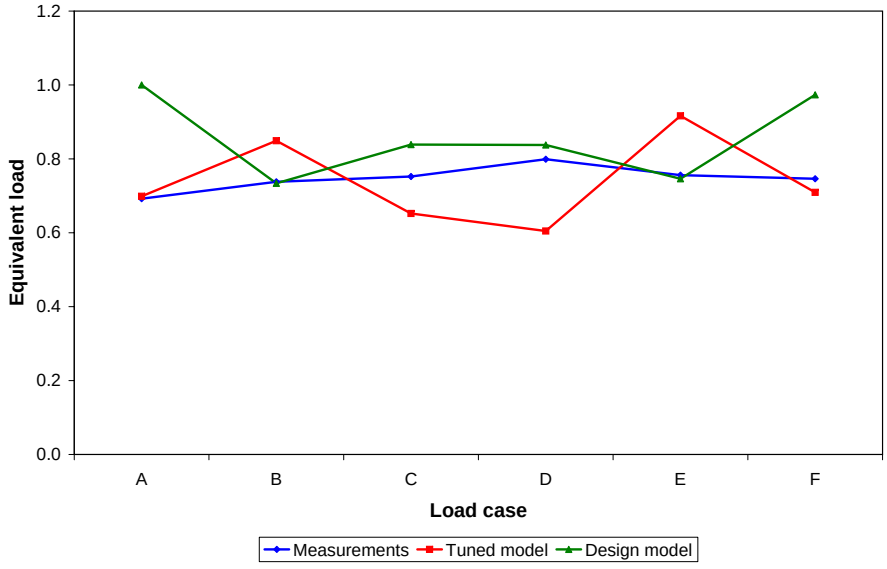

Figure 8.2 Fatigue damage equivalent loads of the *towberoll*, for verification load cases with the turbine in operation.

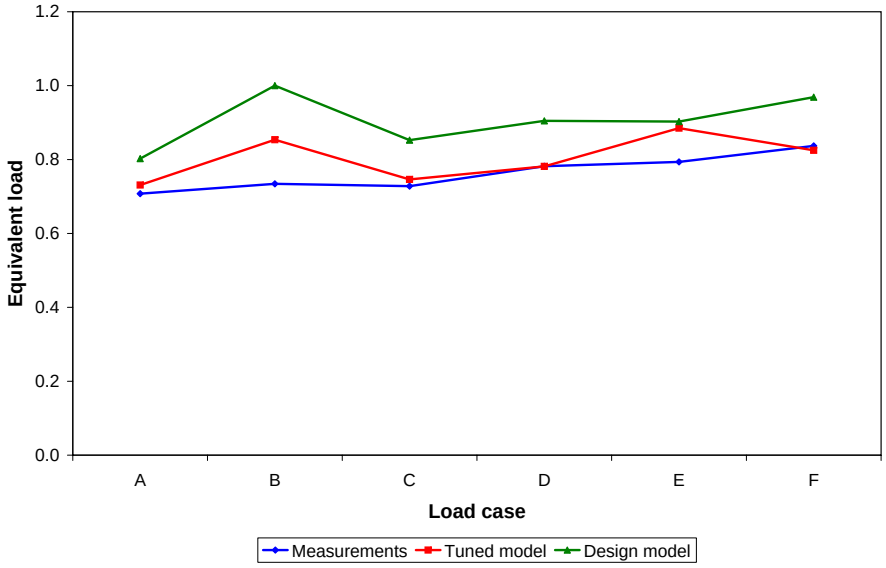

Figure 8.3 Fatigue damage equivalent loads of the *monbetilt* for verification load cases with the turbine in operation.

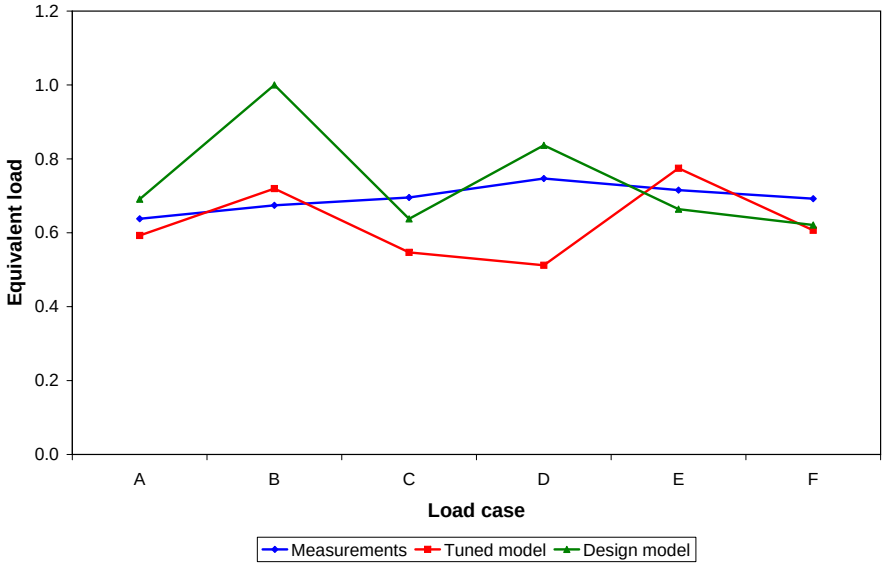

Figure 8.4 Fatigue damage equivalent loads of the *monberoll* for verification load cases with the turbine in operation.

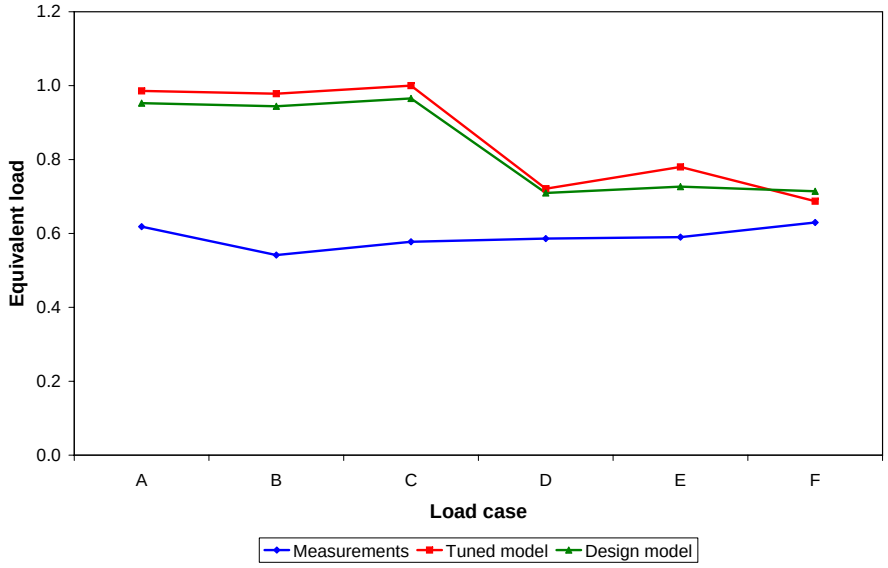

Figure 8.5 Fatigue damage equivalent loads of the *blbef* for verification load cases with the turbine in operation.

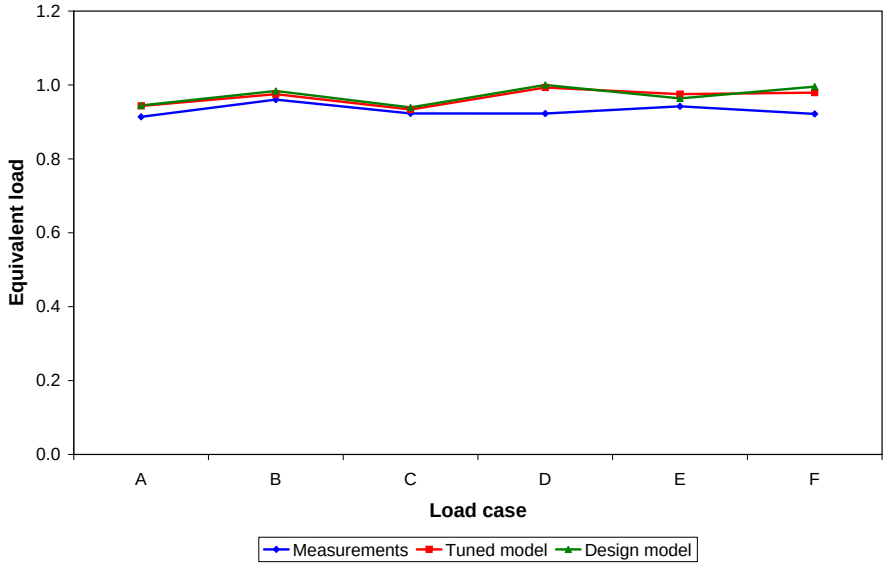

Figure 8.6 Fatigue damage equivalent loads of the *blbee* for verification load cases with the turbine in operation.

case D), and 48.3% with design model (load case B). The average deviation of the tuned model from the equivalent loads of the measured bending moments at tower bottom is 13.3%, and 14.5% for the monopile at mudline level. For the design model, average differences are 15.5% and 34.5%, respectively. However, despite the fact that design model shows higher average and maximum differences with measurements, this model provides more accurate results than the tuned model for 4 out of the 6 cases studied (load cases B to E) for the tower bottom bending moments.

None of the models are precisely reproducing the bending moments on the blade root in flapwise direction. Nevertheless, following the trend from results shown in chapter 7, bending moments on edgewise direction are almost equal to those measured, as can be seen in figure 8.6. Mean deviations of the equivalent loads obtained with the models from those obtained from measurements reach 46.3% for flapwise direction, and 4.4% for edgewise, with maximum differences of 80.6% and 8.4%, respectively.

Finally, it should be highlighted that all the simulated fore-aft bending moments, both at tower bottom and on the monopile at mudline, with both models, are overestimated. This overestimation is even more patent in the case of balde root bending moments, both in flapwise and edgewise directions. However, in side-to-side direction no trend in simulation results is observed.

8.2.2 Severe sea states with the turbine not in operation

Figures 8.7, 8.8, 8.9 and 8.10 show the equivalent loads for the tower and monopile, in fore-aft and side-to-side directions, for six severe sea state cases in which the turbine is not in operation.

From figure 8.7, small differences between the *towbetilt* equivalent loads obtained from simulations with the tuned model and with design model are observed. However, these differences are more notorious in the case of the the monopile at mudline level. In this case, bending moments are highly overestimated with the design model, mainly due to the aforementioned larger water depth assumed in design. Maximum differences on equivalent loads between measurements and simulations for the fore-aft bending moments at tower bottom reach 20.68% for the tuned model, and 15.2% for the design model, both of them happening in load case G. For the *monbetilt*, the maximum difference between measurements and simulation results again is found in load case G: for the tuned model is 12.1%, whilst for the design model this difference is increased up till 50.7%. The average deviation of the tuned model from the measurements is 9.3%, for both tower and monopile. For the design model, these mean differences are 7.9% and 39.2%, respectively.

In side-to-side direction, again small variations are observed on the accuracy of both models. Moreover, results from the design model are closer to measurements than those from the tuned model, for the bending moments on the monopile at mudine level. However, due to the different length of the monopile in the design model, these results are not representative of a more accurate simulation, but of a coincidence. Maximum *towberoll* equivalent load differences between measurements and simulations are 17.1% for the tuned model (in load case H), and 31.9% for the design model (happening on load case G). In the case

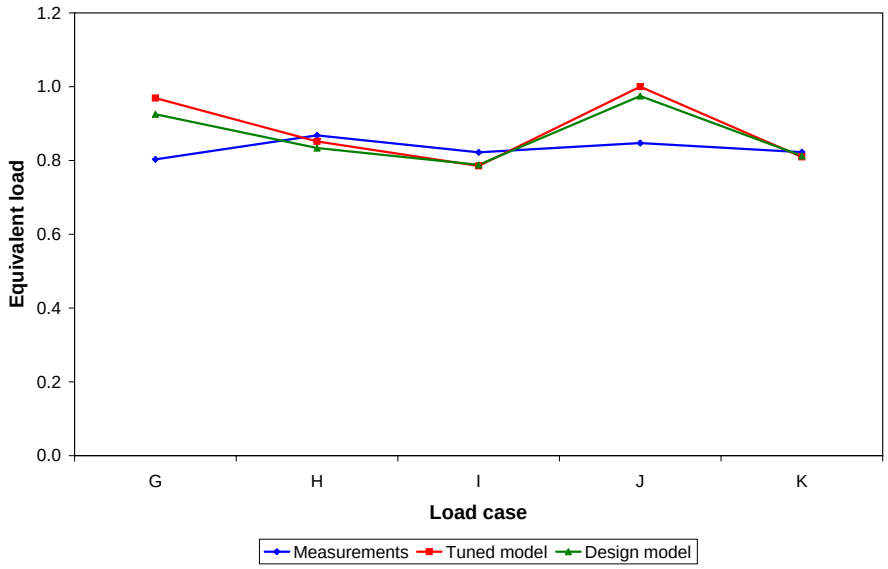

Figure 8.7 Fatigue damage equivalent loads of the *towbetilt*, for severe sea state load cases with the turbine not in operation.

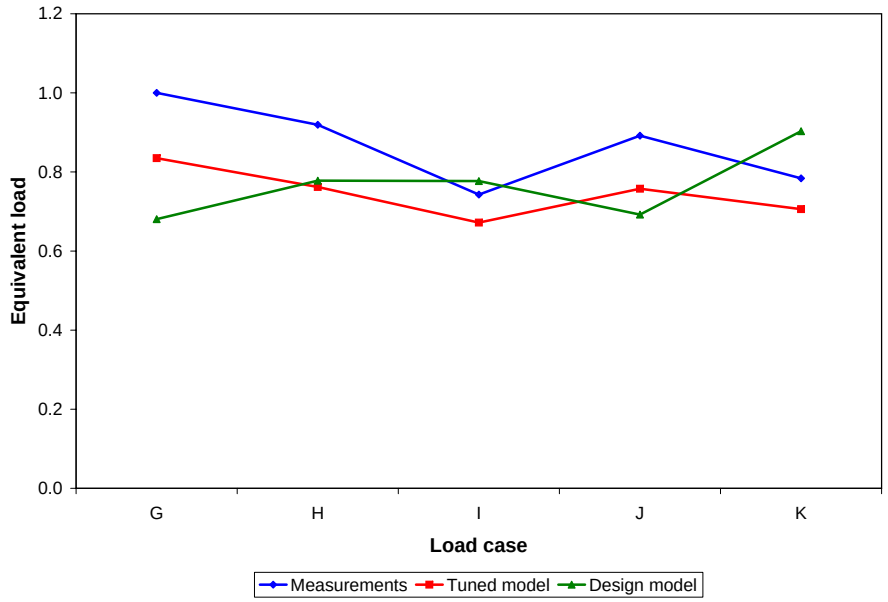

Figure 8.8 Fatigue damage equivalent loads of the *towberoll*, for verification load cases with the turbine not in operation.

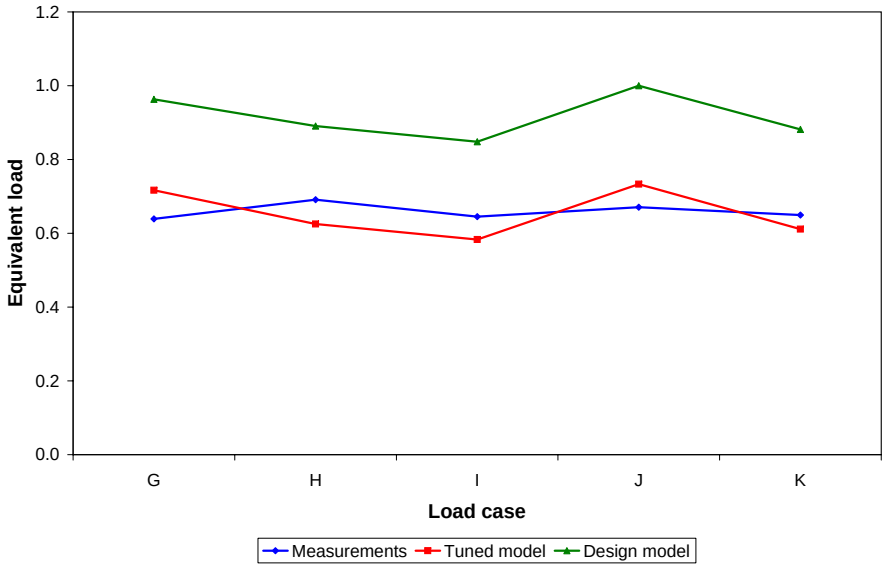

Figure 8.9 Fatigue damage equivalent loads of the *monbetilt* for verification load cases with the turbine not in operation.

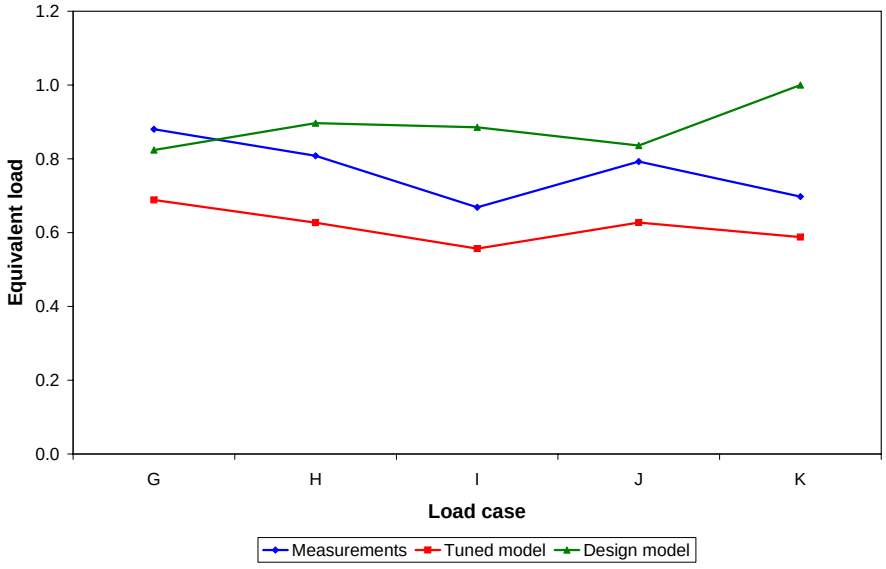

Figure 8.10 Fatigue damage equivalent loads of the *monberoll* for verification load cases with the turbine not in operation.

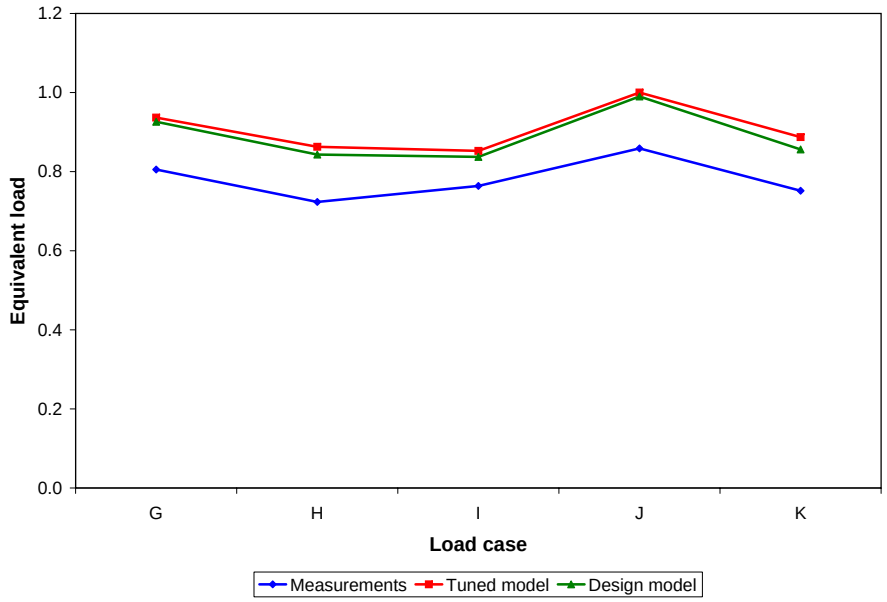

Figure 8.11 Fatigue damage equivalent loads of the *blbef* for verification load cases with the turbine not in operation.

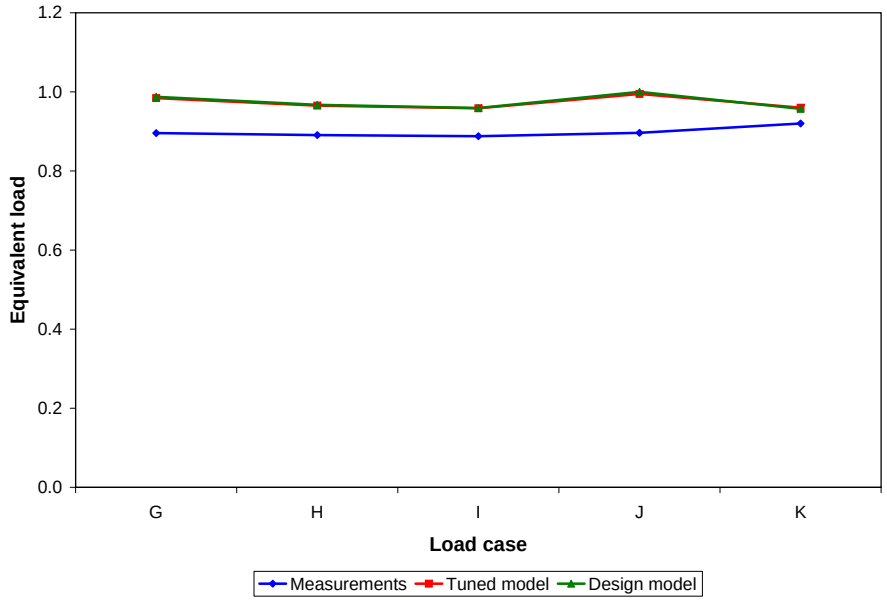

Figure 8.12 Fatigue damage equivalent loads of the *blbee* for verification load cases with the turbine not in operation.

of the monopile, these deviations reach 22.4% for the tuned model (again load case H), and 43.4% for the design model (load case K). The mean differences between the results from the tuned simulation model and measurements are 13.6% (for the tower bottom) and 19.5% (for the monopile at mudline level). For the original design model, these differences reach 17.9% and 19.7%, respectively.

Blade root bending moments are accurately reproduced by both models (see figures 8.11 and 8.12). Again, results from both models are quite close, with maximum differences from the measurements of 19% in the case of flapwise direction, and 11.5% for edgewise direction. Average deviations are in the order of 15% for the flapwise bending moments, and 8.5% for the edgewise bending moments.

Finally, it should be highlighted that all the side-to-side equivalent loads calculated with the tuned model, both for the tower and monopile, are underestimated. In addition, blade root bending moments, in both flapwise and edgewise directions, are overestimated with both models.

8.3 Conclusions

Two possible cases are assessed in the analysis of severe sea states: a situation where the turbine is operating, and a situation where the turbine is stopped.

The main outcome of the analysis of severe sea state cases is described below:

1) Fore-aft bending moments, both on the tower and on the monopile, are in general more accurately reproduced by the tuned model than by the design model. However, for the not-in-operation case, the design model provides almost the same results as the tuned model for the tower bottom. In addition, it should be kept in mind that the design model does not provide reliable results for the bending moments on the monopile at mudline level, due to the higher water depth assumed in the design phase.

2) Side-to-side bending moments are more accurately reproduced by the tuned model for the in-operation situation. In the idling case, side-to-side bending moments are significantly underestimated for all the studied load cases. The design model provides also reasonable results for the tower bottom bending moments, in the same order of magnitude as those results from the tuned model.

3) Blade root bending moments in flapwise direction are overestimated for both cases in which the turbine is operating or idling. Moreover, edgewise bending moments are also overestimated for all cases, though to a lower extent.

Chapter 9

Conclusions and recommendations

9.1 Conclusions of the project

The main outcome of the project can be divided into a verification of the design environmental conditions at turbine 1, and a load verification in the partial load range.

9.1.1 Verification of design environmental conditions

The main conclusions regarding the verification of the design are related to the environmental conditions at the Arklow Bank site:

1) Large differences between the design turbulence intensity and the turbulence intensity measured at the site arise. The design phase considered a the extension of the wind farm up to 33 turbies, which finally has not been carried out. The design turbulence intensity is not referred only to the ambient turbulence, but also to the background turbulence from the whole wind farm, and to a continuous wake operation. Therefore, design turbulence intensity values are much higher than those actually measured.

2) The water depth measured at the Arklow Bank site (5.25 m) shows large discrepancy with the design water depth (9.30 m). However, due to the reduced amount of data (only two measurements), no firm conclusion can be extracted.

3) Large differences between the maximum design wave heights and the maximum measured wave heights are observed. Design values for the significant wave heights overestimate the real waves conditions.

9.1.2 Load verification

When the present thesis was first defined, its main objective was the verification of the design of the Arklow Bank Offshore Wind Farm regarding natural frequencies, long term fatigue damage and extreme loads. However, this objective has turned out to be unattainable. Long term fatigue analysis cannot be verified due to the short measuring campaign, which does not provide representative data of the weather conditions at the Arklow Bank along the year. Furthermore, no extreme events have been measured during the measurements period, hence no comparison of design extreme loads with real data can be performed.

Therefore, a more realistic objective has been defined. As mentioned in section 7.2.1, the load verification process aims at the validation of the aeroelastic model of the wind turbine. The long term fatigue analysis performed in design is based on a proper selection of the fatigue load cases from the scatter diagram, and on the calculation of the loads for each of those load cases. As the first step cannot be analyzed due to the short period in which measurements were taken, the analysis focuses on the second step, i.e. the turbine model in FLEX5.

As FLEX5 describes the responses of the different subsystems of the turbine based on their modal properties, the natural frequencies analysis is performed before the fatigue analysis. Design model is tuned according to measured environmental conditions (water depth) and modal properties (natural frequencies and damping ratios) in order to get a more accurate model.

Regarding the analysis of natural frequencies, some important differences arise between measurements and the design model: 15% in the first natural frequency of the support structure in both fore-aft and side-to-side directions. Nevertheless, measured natural frequencies are inside the safety range provided by the design modal analysis, ensuring a safe performance of the turbine. No scour has been detected during the measurement campaign, and therefore support structure natural frequencies are not expected to vary in time due to this effect.

The performance of the turbine model regarding fatigue has only be assessed for the partial load range. In order to make reasonable comparisons between design and verification load cases, some criteria have been used for the selection of time histories used in the verification process. The wind speed and significant wave height have been used as the main parameters of the selection. Nevertheless, for wind speeds above 14 m/s, no 10-min measurement period complying with the selection criteria was found. Several conclusions are extracted from the fatigue analysis:

1. In all the 17 analyzed cases there is a wind and waves misalignment. This leads to higher loads in side-to-side direction, while keeping the fore-aft loads approximately equal.

2. Hydrodynamic loads on the turbines at the Arklow Bank Offshore Wind Farm are not negligible, despite the shallow water depth and mild weather conditions.

Finally, as no extreme events were measured during the measuring campaign, an analysis of the most severe measured conditions has been performed.

Therefore, the response of the turbine under severe weather conditions is studied. However, this analysis is done in terms of fatigue damage equivalent load, rather than as an extreme load assessment. Results from this analysis are not so accurate as those for the partial load range.

9.2 Recommendations and further work

Some recommendations are given for future offshore wind farms:

- Longer measurement campaign. The scope of the project has been conditioned by the duration of the measuring campaign. In order to be able to make long term predictions, the duration of the measuring campaign should be at least one year.
- Waves and current sensors. One of the main outcomes of the project is that there is a frequent wind and waves misalignment at the Arklow Bank. However, no waves direction sensor has been used in order to verify this. The influence of currents on the loads on the turbine could not be assessed, as no measurements have been done.
- More accurate determination of the upper bound for the water depths in design phase. The design water depth at turbine 1 from the Arklow Bank Offshore Wind Farm has been assumed to be 9.30 m. However, an almost constant water depth for the measurements period of 5.25 m has been measured, though only through two bathymetry surveys. Due to the lack of measurement data, no firm conclusion can be drawn. Nevertheless, water depth appears to be highly overestimated.

In addition, three open aspects should be further analyzed for a better understanding of the behaviour of the turbine:

- Deeper natural frequencies analysis of the measurements, in order to determine the origin of the discrepancies between the 1^{st} natural frequency of the blades in flapwise direction, when determined from a free vibration event or from operation. Furthermore, the natural frequencies of the main shaft should be determined, and the source some spectral peaks could not be clearly
- Assessment of fatigue damage of the turbine on the full load range. As mentioned before, the fatigue analysis has only been performed in the partial load range.
- In-depth analysis of the responses of the blades. Results for the blades have not been highly satisfactory, and further research should be carried out in this field.

Bibliography

[1] Álvarez Gómez, M. *Outline of the Master Thesis: Load Verification of the Arklow Bank Offshore Wind Farm.* Technical report, TU Delft.

[2] Seidel, M.; Böker, C. *Arklow Bank Phase 1: Design Basis Vol. 1 - Wind Turbine and Support Structure.* Internal report, GE Wind Energy, **2003**.

[3] Britton, J.; Baxter, R. *VSE Anode Automatic Impressed Current Cathodic Protection System, 25 Ampere (500 A-Yr).* External report GEW-4195 SYS SPEC, Deep Water Corrosion Services Inc., **2004**.

[4] Link, H.-P. *Load measurements on the "GE Wind Energy 3.6s offshore" wind turbine at Arklow Bank Windfarm, Ireland.* External report WT 3953/5, WINDTEST Kaiser-Wilhelm-Koog GmbH, **2004**.

[5] Lloyd, W. *Assessment of the Arklow Bank Offshore Wind Farm site conditions.* External report, Garrad Hassan and Partners Ltd., **2002**.

[6] Seidel, M.; Böker, C. *Design report for the foundation of the GE3.6 offshore at Arklow Bank.* Internal report, GE Wind Energy, **2003**.

[7] Murphy, J.; Dollard, B. *On the Effect of Wind Farm Structures on the Arklow Bank Seabed.* External report, Sure Engineering Europe, **2001**.

[8] Passon, P.; Kühn, M. *Research Program of the Utgrunden Demonstration Offshore Wind Farm. Final Report: Part I. Load and Eigenfrequency Measurement.* Technical Report STEM P11518-2, Wintus GmbH, **2005**.

[9] Reese, L. C.; Van Imple, W. F. *Single piles and pile groups under lateral loading;* A.A.Balkema, 1 ed., 2001.

[10] *PP7 and Flex5 - User Manual.* Internal document, GE Wind Energy, **2006**.

[11] Øye, S. *FLEX5 manual.* Technical report, Technical University of Denmark (Department of Fluid Mechanics), **1999**.

[12] Söker, H.; Illig, C.; Cosack, N.; Kröning, J.; Damaschke, M. *DEWEK* **2006**.

[13] van der Tempel, J. Design of Support Structures for Offshore Wind Turbines. PhD thesis, TU Delft, ISBN 90-76468-11-7, **2006**.

[14] *IEC 61400-3. Wind Turbines. Part 3: Design requirements for offshore wind turbines.* IEC, ed. 3 ed., **2005**.

[15] Pedersen, J.

[16] *IEC 61400-1. Wind Turbine Generator Systems. Part 1: Safety requirements.* Ed. 2 ed., **1998**.

[17] Emmerich, M. *Thrust Coefficient GE Wind Energy 3.6s Offshore* Internal report, GE Wind Energy, **2002**.

Appendix A

Coordinate systems and loads denotation

A.1 Coordinate systems

A.1.1 Rotor blade coordinate system

The origin of the blade fixed coordinate system is at the level of the blade flange plane. The subscript *bl* refers to the blade.

- X_{bl} axis: In the flange plane; according to the right hand rule with reference to Y_{bl} and Z_{bl}.
- Y_{bl} axis: In the flange plane, parallel to the rotor plane at a pitch angle of 3^{o}.
- Z_{bl} axis: Coaxial with the blade pitch axis.

A.1.2 Hub coordinate system

The origin of the hub coordinate system is in the intersection point of the Z_{bl} axis with the main shaft axis. The coordinate system rotates with the main shaft. The subscript *msh* refers to the main shaft.

- X_{msh} axis: In direction of the main shaft axis, positive in direction of the wind.
- Y_{msh} axis: In the rotor plane according to the right hand rule with reference to X_{msh} and Z_{msh}.
- Z_{msh} axis: Z_{bl} axis projection of the reference blade into the rotor plane.

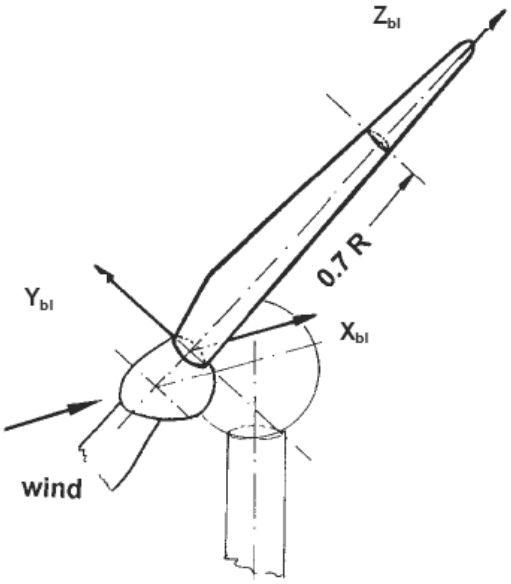

Figure A.1 Rotor blade coordinate system.

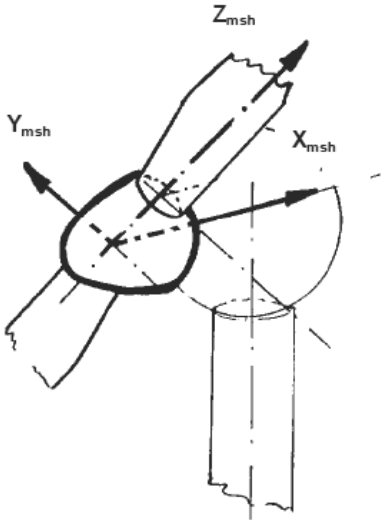

Figure A.2 Hub coordinate system.

A.1.3 Nacelle coordinate system

The origin of the nacelle coordinate system is in the intersection point of the main shaft axis with the tower axis. The subscript n refers to the nacelle.

- X_n axis: Parallel to the main shaft axis, positive in direction of the wind.
- Y_n axis: Horizontal and orthogonal to the X_n axis.
- Z_n axis: According to the right hand rule with reference to X_n and Y_n.

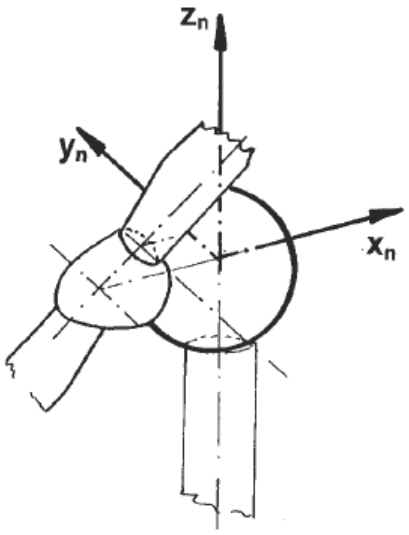

Figure A.3 Nacelle coordinate system.

A.1.4 Tower and monopile coordinate system

The origin of the coordinate system for the tower and monopile is located at the tower bottom. The subscript t refers to both tower and monopile.

- X_t axis: Projection of the X_{msh} on the tower bottom flange plane, positive in direction of the wind.
- Y_t axis: According to the right hand rule with reference to X_t and Z_t.
- Z_t axis: In direction of the tower axis, positive towards the tower top.

A.2 Denotation of loads

The names of the measurement channels used by WINDTEST Kaiser-Wilhelm-Koog GmbH for the bending moments on the rotorblades, main shaft and support structure are specified in table A.1, together with the axis to which they are referred.

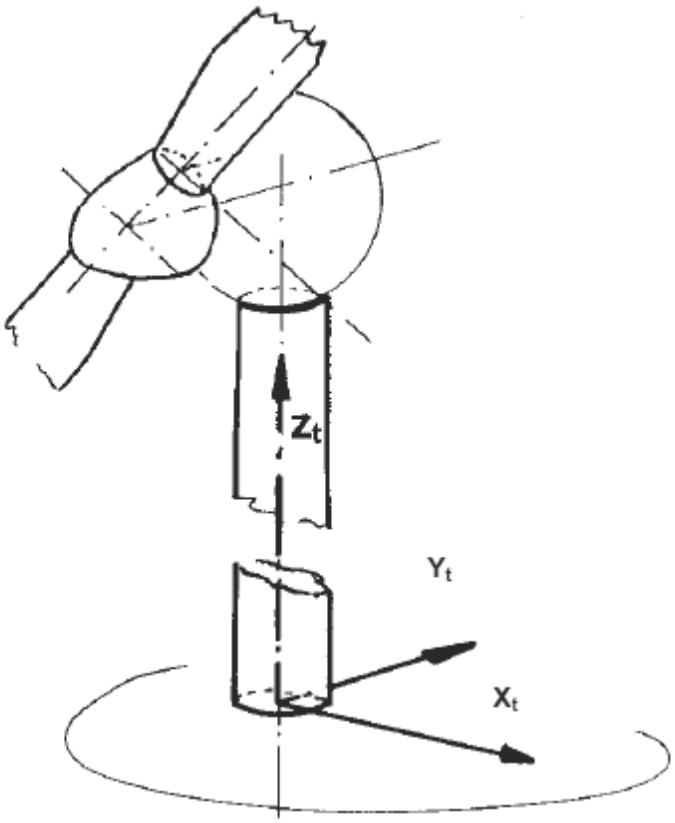

Figure A.4 Tower and monopile coordinate system.

Table A.1 Bending moments measurements channels used by WINDTEST for the blades, main shaft, tower and monopile [4].

Signal	**Channel**	**Axis**
Blade bending		
edgewise	*blbee*	Y_{bl}
flapwise	*blbef*	X_{bl}
Main shaft bending		
tilt	*mshbetlt*	Z_n
yaw	*mshbeyaw*	Y_n
Monopile bending		
fore-aft	*monbetilt*	Y_t
side-to-side	*monberoll*	X_t
Tower bending		
fore-aft	*towbetilt*	Y_t
side-to-side	*towberoll*	X_t

Appendix B

Methods for the calculation of the wind speed Weibull distribution

Three different distributions are calculated when approximating the measured wind speed frequency distribution:

1. Rayleigh distribution.
2. Weibull distribution, calculated with the *standard deviation method*.
3. Weibull distribution, calculated with the *energy density method*.

The calculation method for the Rayleigh distribution is explained in section 4.1.1, and therefore only the cases of the two Weibull distributions are dealt with here.

There are three relations between the Weibull distribution statistic parameters and the Gamma probability distribution Γ that make the wind speed data processing much easier:

1. Annual mean wind speed:

$$U_{mean} = A \cdot \Gamma\left(1 + \frac{1}{k}\right) \tag{B.1}$$

2. Standard deviation of the 10 minutes averaged values with respect to the mean wind speed:

$$\sigma_v^2 = A^2 \cdot \left[\Gamma\left(1 + \frac{2}{k}\right) - \Gamma^2\left(1 + \frac{1}{k}\right)\right] \tag{B.2}$$

3. Energy content of the wind distribution:

$$E' = A^3 \cdot \Gamma\left(1 + \frac{3}{k}\right) \tag{B.3}$$

B.1 Standard deviation method

The standard deviation method uses the first two properties of the Weibull distribution to calculate the A and k parameters:

$$\frac{\sigma_v^2}{U_{mean}^2} = \frac{\Gamma\left(1+\frac{2}{k}\right)}{\Gamma^2\left(1+\frac{1}{k}\right)} - 1 \tag{B.4}$$

The standard deviation of the wind speed data can be calculated by:

$$\sigma_v = \sqrt{\frac{1}{N}\sum_{i=1}^{N}\left(\bar{U} - U_{mean}^2\right)} \tag{B.5}$$

where $\bar{U}$ represents the average wind speed for a 10 min period, and N is the amount of 10 min periods studied.

The mean wind speed can be calculated out of the measurements as:

$$U_{mean} = \frac{1}{N}\sum_{i=1}^{N}\bar{U} \tag{B.6}$$

Therefore, the left term of equation B.4 can be calculated with the statistic parameters from the wind speed data. The only unknown variable is then the shape factor k, which can be calculated by means of an iterative process. The scale parameter A can be then calculated with equation B.1.

B.2 Energy density method

The energy density method applies the same logic as the standard deviation method, but using the energy density relation (equation B.3) instead of the standard deviation one:

$$\frac{E'}{U_{mean}^3} = \frac{\Gamma\left(1+\frac{3}{k}\right)}{\Gamma^3\left(1+\frac{1}{k}\right)} \tag{B.7}$$

The energy density of the wind can be calculated from the measured data as:

$$E' = \frac{1}{N}\sum_{i=1}^{N}\bar{U}^3 \tag{B.8}$$

Again, the left term of expression B.7 can be calculated with the statistic parameters from the wind speed data. By means of an iterative process the

shape factor k is calculated, whilst the scale parameter A is calculated with equation B.1.

Appendix C

Design thrust coefficient curve

The design thrust coefficient curve, for an air density of 1.225 kg/m^3 is shown in figure C.1. The curve is built for a reference turbulence intensity I_{ref} of 12.50% (from IEC 61400-1, Ed. 3 [14]), for stiff conditions, i.e. allowing only the rotational motion of the turbine (only one degree of freedom in the system). This is done so that dynamic effects (which for the support structure are on-site specific) are avoided.

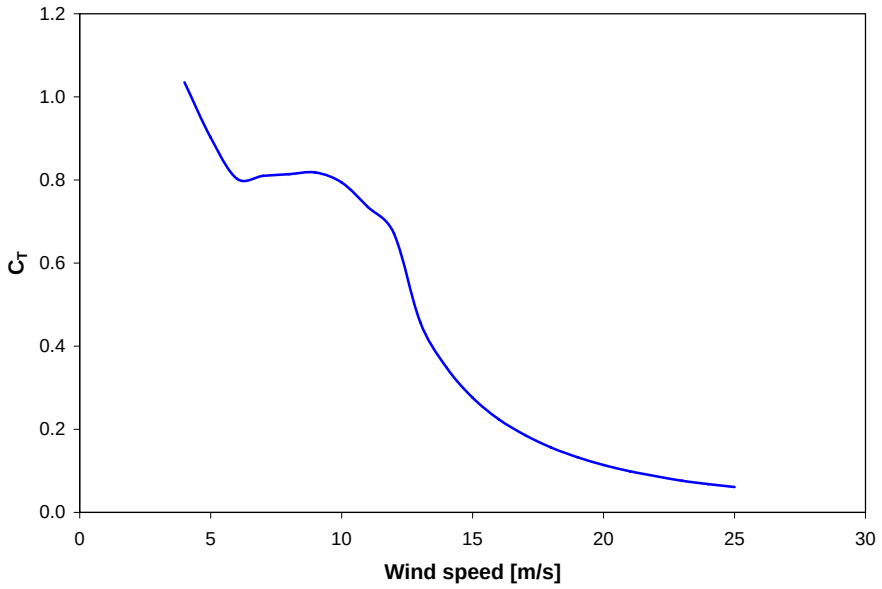

Figure C.1 Design thrust coefficient curve for the GE 3.6s offshore [17].

Appendix D

Influence of the decay parameter and Λ_1 on the coherence function

The coherence function is defined in the IEC standards (IEC 61400 ed. 3 [14]) by the complex magnitude of the cross-spectral density of the longitudinal wind velocity components at two different points divided by the autospectrum function:

$$Coh\,(r,f) = exp\left[-12\cdot\left(\left(\frac{f\cdot r}{V_{hub}}\right)^2+\left(\frac{0.12\cdot r}{L_c}\right)^2\right)^{0.5}\right] \tag{D.1}$$

where

$Coh\,(r,f)$	coherence function
r	magnitude of the projection of the separation vector between the two points on a plane normal to the average wind direction
f	frequency
L_c	coherence scale parameter

The coherence scale parameter L_c is calculated as:

$$L_c = 3.5\cdot\Lambda_1 \tag{D.2}$$

being Λ_1 the longitudinal turbulence scale parameter at hub height, given as

$$\Lambda_1 = \begin{cases} 0.7\cdot z & z \leq 60\ m \\ 42\ \text{m} & z \geq 60\ m \end{cases}$$

The first constant within the exponential function in equation D.1 is called the decay parameter, and is set to 12 in IEC 61400 ed. 3 [14]. However, in the previous edition of the standards (IEC 61400 ed. 2 [16]) its value is 8.8.

This parameter regulates the shape of the coherence function, determining how sharply the decrease of the coherence with increasing distances is.

In equation D.2 there is a second parameter which influences the shape of the coherence curve, besides the wind speed and the frequency and distance variables. This is the longitudinal turbulence scale parameter Λ_1, or the coherence scale parameter L_c, both related by equation D.2. Nevertheless, the influence of this parameter on the coherence function shape is almost negligible, though being relevant for the shape of the wind speed spectrum.

Figure D.1 shows the effect of the different values of the decay parameters on the coherence function, whilst figure D.2 shows the variation of the spectrum with the turbulence scale.

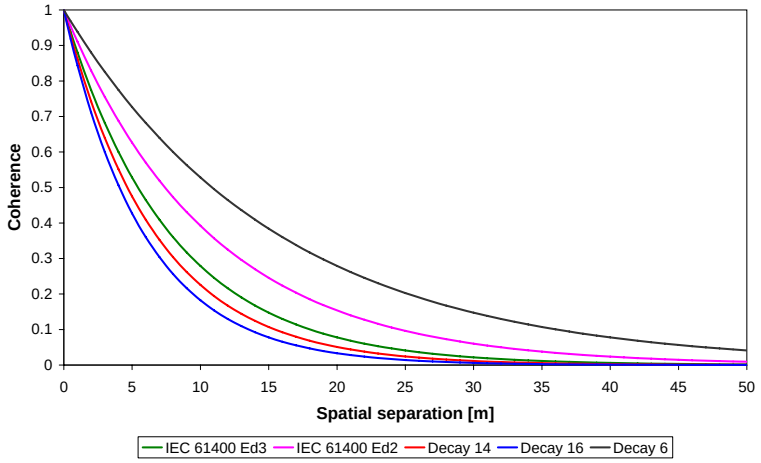

Figure D.1 Variation of the coherence function with the decay parameter (9.43 m/s wind speed, 0.1 Hz, and 42 m of turbulence scale).

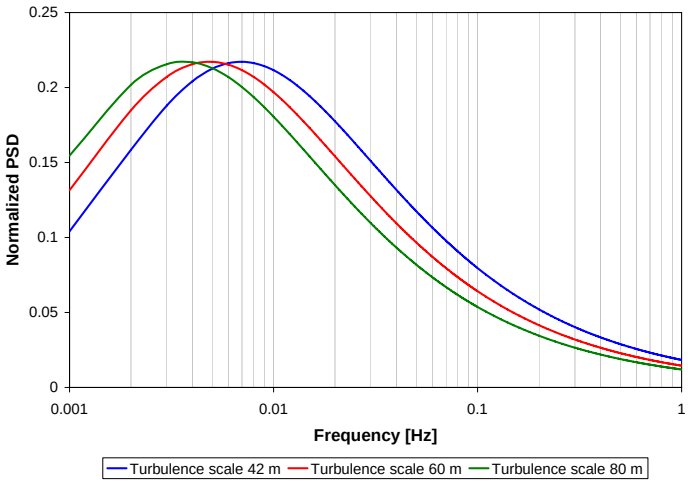

Figure D.2 Variation of the normalized power spectral density of the wind speed with the turbulence scale (9.43 m/s wind speed).